STUDY OF ULTRA-THIN ZINC OXIDE EPILAYER GROWTH AND UV DETECTION PROPERTIES

by

Mingjiao Liu

BS in EE, Jilin University, 1989

MS in EE, University of Pittsburgh, 1999

Submitted to the Graduate Faculty of

School of Engineering in partial fulfillment

of the requirements for the degree of

Doctor of Philosophy

University of Pittsburgh

2003

UNIVERSITY OF PITTSBURGH

SCHOOL OF ENGINEERING

This dissertation was presented

by

Mingjiao Liu

It was defended on

February 24th, 2003

and approved by

Joel Falk, Professor, Department of Electrical Engineering

Dietrich Langer, Professor, Department of Electrical Engineering

Mahmoud El Nokali, Associate Professor, Department of Electrical Engineering

Jean R. Blachere, Associate Professor, Department of Material Science and Engineering

Dissertation Director: Hong Koo Kim, Professor, Department of Electrical Engineering

ABSTRACT

STUDY OF ULTRA-THIN ZINC OXIDE EPILAYER GROWTH AND UV DETECTION PROPERTIES

Mingjiao Liu, PhD

University of Pittsburgh, 2003

ZnO is a wide bandgap (3.4 eV) II-VI semiconductor with large exciton binding energy (60 meV), and holds a strong potential for light emitting/detecting or nonlinear optical devices in the UV range. Essential to development of such devices is establishment of proper methods to grow/synthesize high quality materials and structures whose properties (electrical, optical, etc.) can be tailored to specific device application. Ultra-thin (nanometer-scale) ZnO films, for example, are of particular interest, due to the device potential involving the quantum confinement effects.

In this study, we have investigated the early-stage growth mode of ZnO on sapphire. The evolution of structural, morphological, and electrical properties was characterized with 2 to 20-nm-thick ZnO films grown at 700 ^{o}C with radio-frequency magnetron sputtering. X-ray diffraction results show that ZnO initially grows highly strained and epitaxial to substrate with negligible degree of mosaicity for up to ~5 nm thickness, despite the occurrence of partial strain-relaxation which indicates an incommensurate growth involving misfit dislocations. Then the mosaicity (out-of-plane tilt) develops as film thickness increases to around 10 nm. Both the atomic force microscopy (AFM) and resistivity measurement results suggest that ZnO grows as mostly discontinuous (electrically and physically) three-dimensional (3D) nano-islands at 2 to 5 nm thickness, and then the islands coalesce/merge and become connected, fully covering the substrate surface at 5 to 10 nm.

The optoelectronic properties of nanometer-thickness films are often dominated by the surface-mediated phenomena due to the large surface/volume ratio. It is well known that ZnO exhibits a strong chemisorption behavior through surface. While this phenomenon could be beneficial to some applications (such as chemical/gas sensing), it would also be desirable to control/alleviate this phenomenon in order to observe the effects originating from the dimensional and size confinement of intrinsic materials. We have investigated an oxygen-plasma treatment as a possible means of modifying/controlling the surface properties of ultra-thin (~20-nm-thick) ZnO epitaxial films. Oxygen plasma treatment is found to dramatically enhance the UV detection properties of ZnO, reducing the decay time constant and increasing the on/off ratio. Thus, for the first time, we have developed and demonstrated high speed, high reponsivity UV photodetectors with extremely low dark current using a single layer of nanometer-thick ZnO.

A model, based on modulation mechanism of the conductive volume and carriers, has been developed to explain the power dependence of the UV responsivity of ZnO photodetectors. In this model, the photocurrent decay process is analyzed with oxygen chemisorption and thermionic theory. The results suggest that the plasma treatment reduces the oxygen vacancy concentration at the surface and in the near-surface bulk of ZnO, which in turn reduces the surface band bending and therefore the chemisorption effects. Oxygen plasma treatment is considered an effective way of making nanometer-scale ZnO viable for high performance UV optoelectronic devices. The effects observed in this study are also expected to be observable in other low-dimensional structures of ZnO, such as quantum dots, nano wires and ribbons.

DESCRIPTORS

Epitaxy	Oxygen Plasma Treatment
RF Sputtering	UV Photodetector
Wideband Gap Semiconductor	ZnO

ACKNOWLEDGEMENT

I would like to gratefully acknowledge my advisor Professor Hong Koo Kim for his patience and great guidance during this study. His encouragement and generosity allowed me to accomplish this work. My gratitude to him can't be expressed in words.

My sincere thanks are to Professor Blachère of the Department of Material Science and Enginerrring for his kind and generous help.

I also thank my colleagues Zhijun Sun, Yun-Suk Jung and Zuo Zhang. We have a good time to work together.

I dedicate this thesis to my parents and to my dear wife Jinru Wen. I am grateful to them for always encouraging me to pursue my ideas and for their unfailing support and love.

TABLE OF CONTENTS

LIST OF TABLES

LIST OF FIGURES

1.0 INTRODUCTION

Zinc oxide has been under intensive investigation since the 1950s. It is an important material for a variety of practical applications. It has found applications in industries such as rubber and adhesive, paint and coating, advanced ceramics, and chemical. Zinc oxide has found many applications in electronics as well, as a transparent conductive material, thin film gas sensor, varistor, luminescent material, ultra-high-frequency electroacoustic transducer, etc. The majority of the applications based on zinc oxide use polycrystalline materials.[1] Recently, however, large-area bulk crystal growth has been achieved,[2] and, furthermore, several epitaxial methods have produced excellent materials.[3-7] Also, quantum wells have been successfully grown, by alloying with Mg or Cd.[8] ZnO is now considered as a promising candidate for short-wavelength photonic devices, and high-power, high-frequency electronic devices, etc.

Over the past few years, due to a strong commercial desire for blue and ultraviolet (UV) light emitters, the growth techniques and optical properties of most of the wide band gap semiconductors have been studied. The extensively researched materials include III-V nitrides and ZnSe based II-VI compounds. Both of these materials have been successfully used for fabrication of continuous wave laser diodes (LDs) working at room temperature. These achievements encourage people to explore other wide band gap semiconductors that have distinctive properties. One of the newer systems attracting increasing attention is ZnO, a compound semiconductor of the II-VI family, which has a direct band gap in the UV range (3.37 eV at room temperature). An appreciation of the potential of ZnO for optoelectronic applications can be obtained by examining Table 1, which compares the relevant material properties of ZnO with those of other wide gap semiconductors. The notable properties are the large bond strength (indicated by the cohesive energy and the melting point) and the extreme stability of excitons (indicated by the large exciton binding energy). ZnO is one of the “hardest” materials in the II-VI compound family. It is expected that a degradation of the material due to the generation of dislocation (dark line defects) during device operation will not be an issue. The stability of the exciton makes ZnO a promising material for the realization of excitonic laser gain at room temperature. The excitonic laser gain and its prospective advantages have been demonstrated for ZnSe based quantum well laser diodes (LDs). However, because of the relatively small exciton

binding energy of ZnSe, they still have difficulties in extending such a lasing mechanism up to room temperature even when using quantum wells. ZnO has an exciton binding energy of 60 meV, which corresponds to 2.4 times the effective thermal energy at room temperature. Furthermore, by reducing the dimensions of the active region in the LD, the binding energy of the excitons and the oscillator strength can be greatly enhanced. Even excitonic process such as radiative recombination of biexcitons could be expected to play a role in laser gain. [9]

Table 1 Comparison of properties of ZnO with those of other wide gap semiconductors (6H-SiC is an indirect band gap semiconductor)

Material	Crystal structure	Lattice constant		Band gap energy at RT E_g (eV)	Cohesive energy E_{coh} (eV)	Melting point T_m (K)	Exciton binding energy E_b (meV)	Dielectric constant	
		a (Å)	c (Å)					$\varepsilon(0)$	$\varepsilon(\infty)$
ZnO	Wurtzite	3.429	5.207	3.37	1.89	2248	60	8.75	3.75
ZnS	Wurtzite	3.823	6.261	3.8	1.59	2103	39	9.6	5.7
ZnSe	Zinc blende	5.668	…	2.70	1.29	1793	20	9.1	6.3
GaN	Wurtzite	3.189	5.185	3.39	2.24	1973	21	8.9	5.35
6H-SiC	Wurtzite	3.081	15.117	2.86	3.17	>2100	…	9.66	6.52

Since ZnO is a direct band gap material with high radiation hardness, it is also a good candidate for visible-blind detectors, and can be used in harsh environments. The importance of UV semiconductor detectors and the continuing emphasis on the development of low light level imaging systems for military and civilian surveillance applications have resulted in the recent meteoric expansion of the semiconductor industry. Many of the applications for UV detection involve hostile environments such as in situ combustion monitoring and satellite-based missile plume detection, where the ruggedness of active UV detector material is an important advantage. Other applications capitalize on the sensitivity of wide band-gap semiconductor detectors, such

as air quality monitoring, and gas sensing. The aerospace, automotive, petroleum industries, and others have continuously provided the impetus pushing the development of fringe technologies, which are tolerant of increasingly high temperature and hostile environments.[10]

For ultraviolet radiation corresponding to photon energies higher than 3.1 eV, even silicon with energy gap of 1.12 eV can be used for the detection. However, silicon is not the material of choice, since it also response to light other than UV range. Under typical conditions, ambient illumination will subject a semiconductor detector to many photos in the visible or infrared (IR) range, and, therefore, it is very desirable to have the UV detector insensitive to the visible and IR radiation (called solar-blind or visible-blind). This carves a unique niche for wide band gap semiconductors, such as ZnO, which is mostly transparent to visible and IR radiation. Figure 1-1 shows the band gaps and lattice constants of semiconductor materials with energy gaps of 3 eV or more.[11]

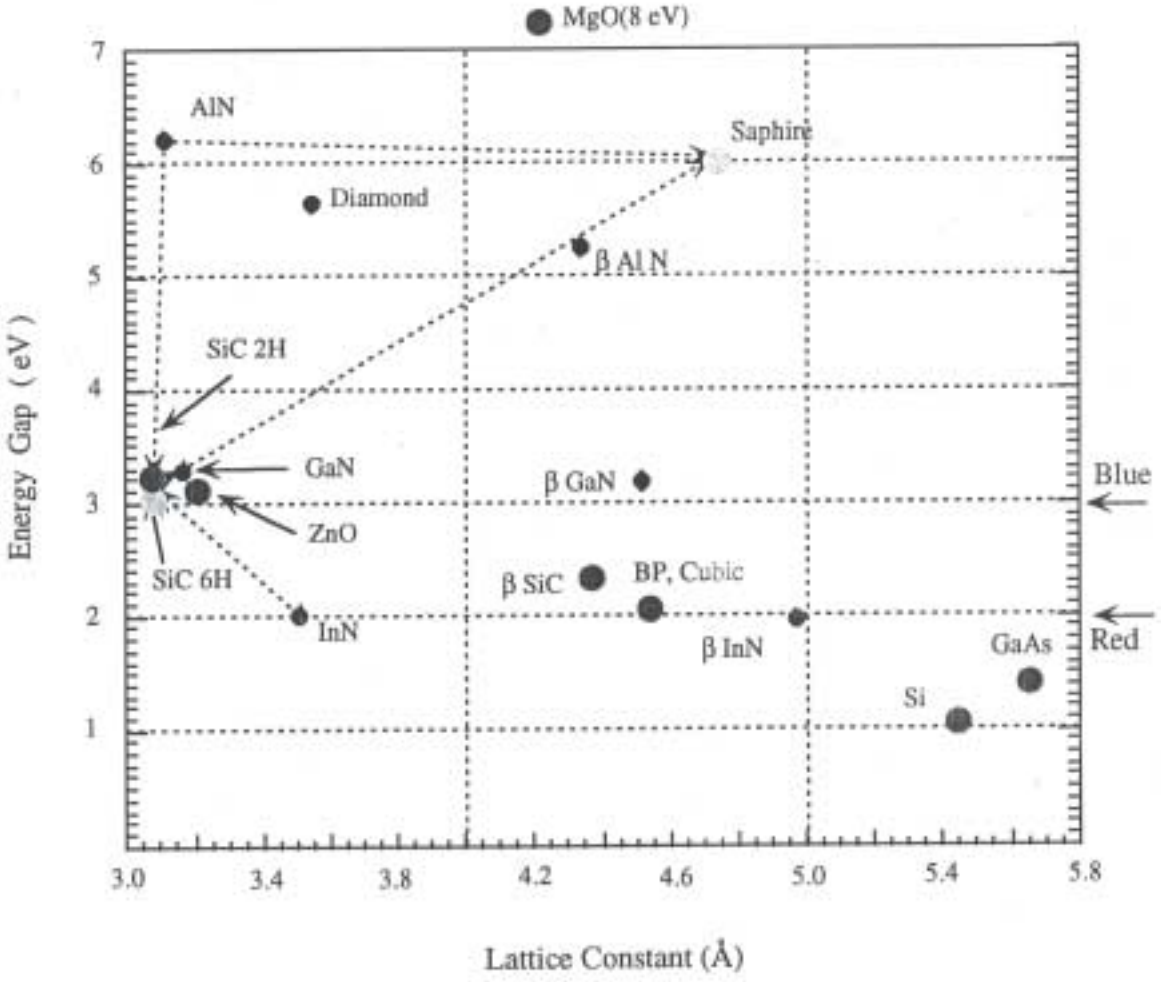

Figure 1.1 The bandgaps of common widegap semiconductors and their lattice constants.[11]

1.1 Structure of ZnO

Zinc oxide crystallizes in the hexagonal wurtzite lattice, in which the oxygen ions are arranged in closest hexagonal packing, and the zinc ions occupy half of the tetrahedral interstitial positions and have the same relative arrangement as the oxygen ions (Figure 1-2 (a)). Actually, the environment of each ion does not have exact tetrahedral symmetry. Instead, the spacing between nearest neighbors in the direction of the hexagonal, or c axis, is somewhat smaller than other three neighbors. The bonding is essentially polar; however, there is a homopolar component of binding between next nearest zinc and oxygen ions in the direction of the c axis.[12]

ZnO is on the border between a semiconductor and an ionic material. Under most growth conditions, it displays an n-type semiconductor behavior. Even though it is tetrahedrally bonded, similar to other semiconductors, the bonds have a partial ionic character. It has been proposed that a formal charge distribution of $Zn^{1,2+}O^{1,2-}$ be assigned to ZnO.[13] It belongs to the $P_6 3mc$ space group with lattice parameters, a=3.24982 Å and c=5.20661 Å (Table 1-2).[12] The c/a ratio is 1.602, which is slightly less than the ideal value of 1.633 for the ideal close packed structure. The Zn-O distance is 1.992 Å parallel to the c-axis and 1.973 Å in the other three directions of the tetrahedral arrangement of nearest neighbors. The lattice consists of two interpenetrating hexagonal-close-packed lattices, separating along the c-axis by 0.3825 (fractional coordinates). While oxygen (by convention) occupies the (0 0 0) and (0.6667 0.3333 0.5) positions, zinc occupies the (0 0 0.3825) and (0.6667 0.3333 0.8825) positions.[14] The crystal structure and its projection along the [$\underline{2}$110] direction are shown in Figure 1-2 (b).[12]

The close-packed (0001) planes are made up of two subplanes (A & a), each consisting of either the cationic (Zn) or the anionic (O) species. The crystal can be considered to have the stacking sequence …AaBbAaBb… as compared to …AaBbCcAaBbCc…in diamond cubic (such as Si) and zincblende (such as GaAs) crystal structures. This results in dramatic difference in the properties between the (0001) and (000$\underline{1}$) planes, the former being Zn terminated and the later being O terminated. This structure does not possess a center of symmetry. These two characteristics are responsible for some of the most important properties of ZnO. The lack of the

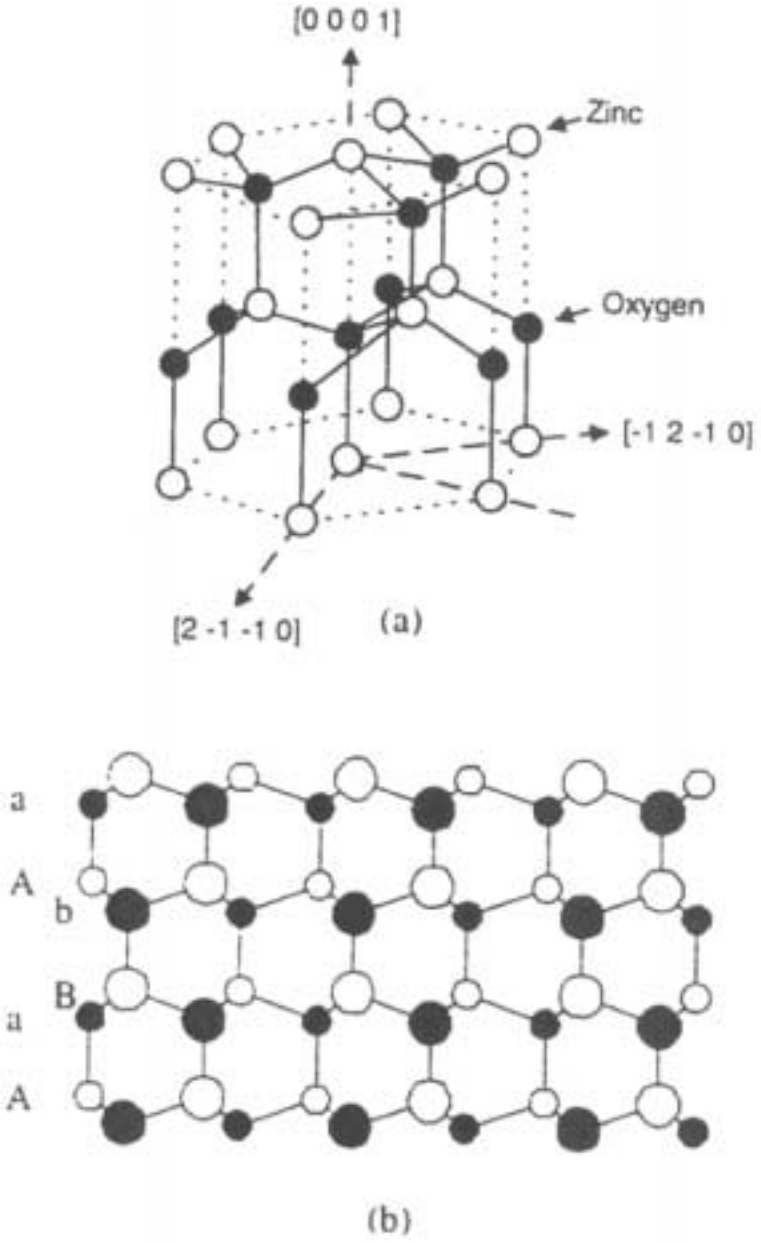

Figure 1.2 Schematic diagram of (a) crystal structure of ZnO (Wurtzite) and (b) the project of the wurtzite structure along the [$\underline{2}$110] direction.

inversion symmetry leads to ZnO being a piezoelectric material and the polarity of the c-axis causes Zn-terminated and O-terminated plane to display vastly different properties. They have profound effect on the structure of the material grown on ZnO, which has been used as substrate or buffer layer of the growth of III-V nitride.

InGaN grown by MOVPE on the Zn-treminated (0001) surface of ZnO substrates has better structure quality than the films grown on sapphire.[15] X-ray diffraction line width of InGaN grown on ZnO were 20% smaller than that of film grown on sapphire. The effect of ZnO substrate on the properties of III-V nitride grown by reactive molecular beam epitaxy has also been studied. It has been found that the best quality GaN films obtained were the ones grown on the O-terminated (0001) ZnO surfaces.[16] The characteristic yellow photoluminescence peak normally observed in GaN on Al_2O_3, which is produced due to defects in the film, was absent or was very weak in GaN films grown on ZnO.

The role of a ZnO buffer layer (grown on c-Al_2O_3) on III-nitride growth has also been investigated. By using rf sputtered ZnO buffered c-sapphire substrate, hydride vapor phase epitaxial growth of a high quality GaN film was realized. The electrical, crystalline, and optical properties of the GaN film are found to be superior to those grown directly on sapphire. The highest electron mobility has been obtained. Moreover, the c-oriented sputtered ZnO layer improves the reproducibility of the growth of GaN by HVPE.[17]

Table 2 Crystal structure, lattice constants and thermal expansion coefficients of ZnO, GaN and Al_2O_3.

	ZnO	GaN	α-Al_2O_3
Crystal structure	Wurtzite	Wurtzite	Corundum
Space group	$P_6$3mc	$P_6$3mc	R$\underline{3}$c
Lattice constants (Å)	a = 3.249	3.186	4.758
	c = 5.207	5.178	12.99
Thermal Expansions coefficients (10^{-6}/ºK)	6.51 ($\perp$c)	5.59 ($\perp$c)	7.5 ($\perp$c)
	3.02 (//c)	7.75 (//c)	8.5 (//c)

1.1.1 Native Defects and Extrinsic Doping of ZnO

1.1.1.1 Native Point Defects in ZnO. Native defects (also referred to as intrinsic defects) commonly occur in semiconductors. The three basic types of defects are vacancies (an atom missing from a lattice site), self-interstitials (an additional atom in the lattice), and antisites (in compound semiconductors, when, e.g., a cation is sitting on an anion site). For each of these types, the defect can occur either on the cation site or on the anion site.

Single-crystal ZnO has always been observed to contain metal excess (or oxygen deficiency) under experimentally attainable zinc and oxygen partial pressure.[18,19] The metal excess can be accommodated in part by the presence of zinc interstitials or oxygen vacancies.

In the following discussion, the defects are formulated in Kröger's nomenclature. The defect notation S_M^X is employed, where '*S*' represents the species occupying the lattice site *M*. The superscript represents the charge of the species relative to normal site occupancy with prime indicating a negative charge, and a dot representing a positive charge.

Zn excess, $Zn_{1+\delta}O$, can be understood as the dissolution of zinc forming the donor *D*

$$Zn_g \Leftrightarrow D. \qquad (1\text{-}1)$$

As in a large temperature range, the donors are known to be singly ionized; the defect equilibria are formulated in the corresponding manner. Thus, equation 1-1 takes the form

$$Zn_g \Leftrightarrow Zn^{\cdot}_i + e', \qquad (1\text{-}1a)$$

if zinc interstitials Zn_i are created or

$$Zn_g \Leftrightarrow Zn_{Zn} + V^{\cdot}_O + e', \qquad (1\text{-}1b)$$

if oxygen vacancies, V_O, are the dominating defects. Zinc excess can also be understood as a partial vaporization of oxygen

$$Zn_{Zn} + O_O \Leftrightarrow D + \frac{1}{2}O_2 \qquad (1\text{-}2)$$

or with ionized donor

$$Zn_{Zn} + O_O \Leftrightarrow Zn^{\cdot}_i + \frac{1}{2}O_2 + e \,, \qquad (1\text{-}2a)$$

and

$$Zn_{Zn} + O_O \Leftrightarrow V^{\cdot}_O + \frac{1}{2}O_2 + e \,. \qquad (1\text{-}2b)$$

Analogously, the dissolution of oxygen in zinc oxide can be formulated as

$$\frac{1}{2}O_{2g} \Leftrightarrow A(+O_O) \,, \qquad (1\text{-}3)$$

or assuming singly ionized acceptors in the form of zinc vacancies, and oxygen interstitials, respectively

$$\frac{1}{2}O_{2g} \Leftrightarrow V_{Zn}^{'} + O_O + h, \;\; \frac{1}{2}O_{2g} \Leftrightarrow O^{'}_i + h \,. \qquad (1\text{-}3a, b)$$

Again this can be formulated as a partial vaporization, in this case as the vaporization of zinc

$$Zn_{Zn} \Leftrightarrow Zn_g + A \,, \qquad (1\text{-}4)$$

$$Zn_{Zn} \Leftrightarrow Zn_g + V_{Zn}^{'} + h \qquad (1\text{-}4a)$$

or

$$Zn_{Zn} \Leftrightarrow Zn_g + O_i^{'} + h \,. \qquad (1\text{-}4b)$$

Obviously, equation (1-1) and (1-2) and respectively, (1-3) and (1-4) are coupled via the vapor pressure equilibrium of ZnO

$$Zn_{Zn} + O_O \Leftrightarrow Zn_g + \frac{1}{2}O_{2g} \,. \qquad (1\text{-}5)$$

From equations (1-1) to (1-4) it can be concluded that n-type conducting as well as p-type conducting oxide should exist depending on the oxygen or zinc pressure in the adjacent gas phase provided that equilibrium is attained. The type of dominating defect depends distinctly on the value of the intrinsic defect equilibrium constants.[20] Kröger's diagram is constructed to described the defect concentrations dependence of oxygen or zinc vapor pressure under equilibrium (Figure 1-3).

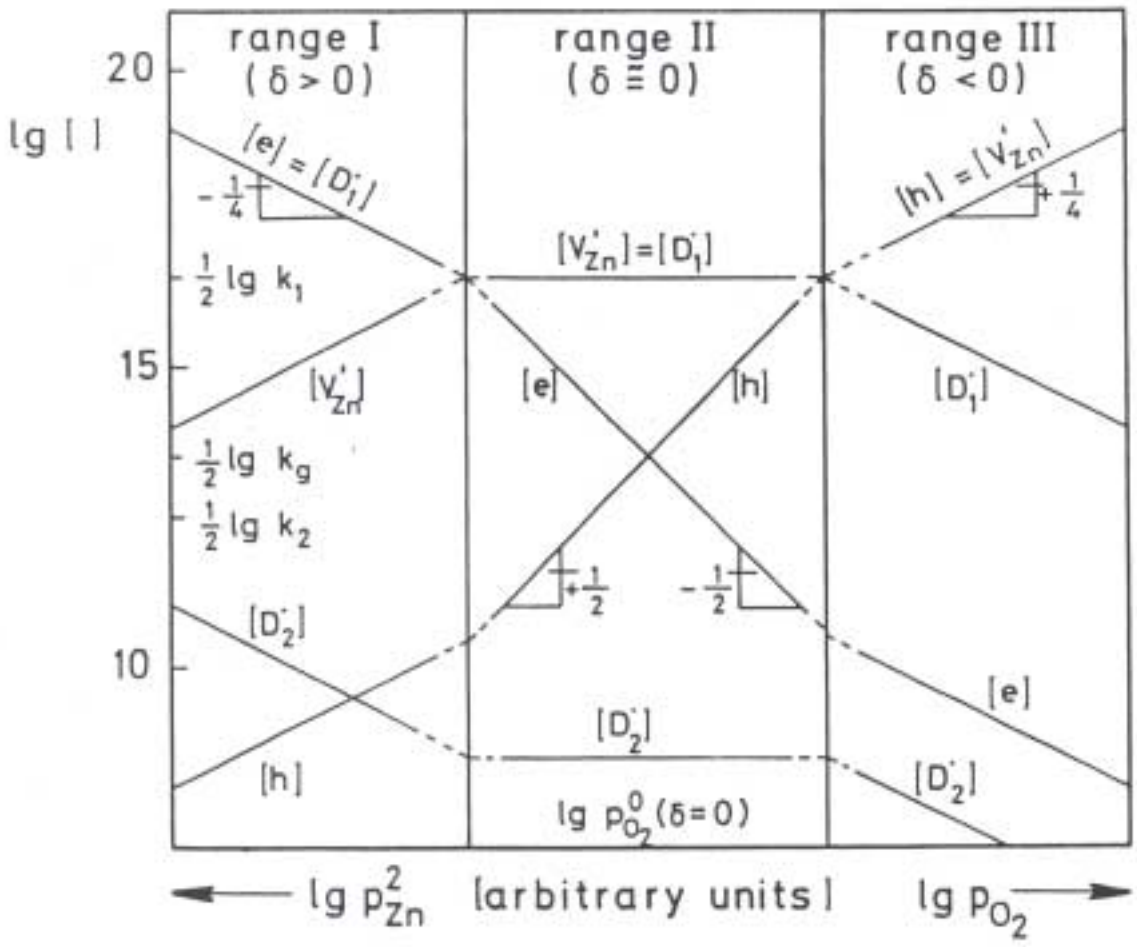

Figure 1.3 Schematic Kröger-Vink-diagram of ZnO.[20]

1.1.1.2 Self-compensation in ZnO. ZnO exhibits an asymmetry in its ability to be doped n-type or p-type like other wide band gap materials. For example, it is difficult, if not impossible, to make diamond and ZnTe n-type, and make ZnSe, ZnS, ZnO, CdS etc. p-type. The simplest explanation suggested for this phenomenon is that native defects compensate the acceptors in the materials.[21]

Because formation of the native defect often involves breaking or rearranging of bonds, deep levels in the semiconductor band gap are typically introduced. The occupation of the levels determines the charge state of the defect. Depending on the location of the levels in the gap, and the charge states they can assume, native defects can have donor-character or acceptor-character, or even be amphoteric.

For the sake of argument, let us assume that a donor-like native defect can be formed, which in the neutral charge state would have an electron residing in a level near the conduct band.[22] If we try to dope the material p-type, we are driving the Fermi level down to a position near the top of valence band. The donor, of course, will become positively charged, by transferring its electron from the gap level to the Fermi level – in the process compensating the electrical activity of an acceptor. The amount of energy gained by this charge transfer can be of the order of the band gap, i.e., a large value in a wide-band-gap semiconductor. The net formation energy of the native defect is equal to create the neutral defect, minus the energy gained by transferring the electron. The above argument indicates that in a wide-band-gap semiconductor the net formation energy of compensating native defects could become very low. This would lead to the formation of a large number of native defects. These donor-type defects of course compensate the acceptors that were introduced to make the material p-type. If this mechanism were indeed active, it would make it impossible to obtain p-type conductor.

The compensation by native defects is an issue in the wide-band-gap semiconductors. However, this compensation mechanism by no means forbids the formation of p-type. A comprehensive investigation of native defects in ZnSe was reported.[23] The main conclusion from this investigation was that native defects in ZnSe do not have significantly lower formation energies than defects in other semiconductors. Their concentrations, therefore, are usually quite

limited, and they do not necessarily pose a threat to the doping of the semiconductors. The prevalence of native defects depends sensitively on the stoichiometry of the material, and on the doping. A p-type doping in ZnSe was achieved.[24]

ZnO is in the same situation, it can be doped n-type via intrinsic or extrinsic doping to the point of becoming a metallic conductor, whereas it is very difficult to made p type via intrinsic doping. Under both Zn-rich and O-rich conditions, the defects (V_O, Zn_i, Zn_O) that compensate p-type doping have low formation enthalpies, and form easily. p-type ZnO, however, was obtained with nitrogen doping by suppressing the formation of oxygen vacancy and zinc intersitial.[25]

1.1.1.3 ZnO Extrinsic Doping. High conductive n-type ZnO can be achieved by Al doping. Al-doped ZnO has been used to be transparent conducting oxide as a front electrode and an optical enhancement window layer for Si solar cells.[26] Other column III metal (Ga, In, Ti) oxide into ZnO also leads to n-type conducting.

$$In_2O_3 \rightarrow 2In_{Zn}^{\cdot} + 2O_O + \frac{1}{2}O_2(g) + 2e \qquad (1\text{-}6)$$

and

$$In_2O_3 \rightarrow 2In_{Zn}^{\cdot} + 3O_O + V_{Zn}^{'} + e, \qquad (1\text{-}7)$$

respectively, in the case of stoichiometric ZnO, and to

$$In_2O_3 + Zn_i^{\cdot} \rightarrow 2In_{Zn}^{\cdot} + 3O_O + Zn_{Zn} + e \qquad (1\text{-}8)$$

and

$$In_2O_3 + V_O^{\cdot} \rightarrow 2In_{Zn}^{\cdot} + 3O_O + e \qquad (1\text{-}9)$$

in the case of n-type conducting samples. All the reactions lead to an increase of the conductivity.

Doping zinc oxide with halides also results in increasing the conductivity because of the following reactions:

$$ZnCl_2 \rightarrow Zn_{Zn} + 2Cl^{\cdot}_O + V_{Zn}^{'} + e, \qquad (1\text{-}10)$$

$$ZnCl_2 + Zn^{\cdot}_i \rightarrow 2Zn_{Zn} + 2Cl^{\cdot}_O + e, \qquad (1\text{-}11)$$

and

$$ZnCl_2 + V_O^{\cdot} \rightarrow Zn_{Zn} + 2Cl^{\cdot}_O + e, \qquad (1\text{-}12)$$

respectively.

Hydrogen can incorporate in high concentration in ZnO and behaves as a shallow donor. Hydrogen is ubiquitous and very difficult to remove from the crystal grown environment. It also forms a strong bond with oxygen, providing a powerful force for its incorporation in the ZnO crystal. Hydrogen even has been considered the cause of the prevailing n-type conductivity of ZnO not the native defects.[27]

Doping with monovalent metal ions in oxide can lead to the increase in the resistivity of ZnO. For example, Li acts as an acceptor when it occupies the position of Zn in ZnO lattice. Li_2O can result in the reaction

$$Li_2O + e \rightarrow 2Li_{Zn}^{'} + O_O + V_O^{\cdot} \qquad (1\text{-}13)$$

and

$$Li_2O + Zn_{Zn} + e \rightarrow 2Li_{Zn}^{'} + O_O + Zn_i^{\cdot} \qquad (1\text{-}14)$$

This would lead the consumption of electron and the reduction of conductivity.

Considering stoichiometric zinc oxide, the reaction of adding Li_2O will be as following

$$Li_2O \rightarrow 2Li_{Zn}^{'} + O_O + V_O^{\cdot} + h \qquad (1\text{-}15)$$

and

$$Li_2O + Zn_{Zn} \rightarrow 2Li_{Zn}^{'} + O_O + Zn_i^{\cdot} + h \qquad (1\text{-}16)$$

This would lead to p-type conductivity. Hitherto, however, this has not been observed experimentally. If Li is in the interstitial sites on ZnO, it is a donor, which will supply the electrons to the crystal and increase the n-type conductivity of ZnO.

p-type ZnO has been achieved by nitrogen doping. Nitrogen is a very effective donor for wide band-gap semiconductor. The successfully fabricated p-type samples were realized by codoping N with H or Ga,[28-29] and p-n homojunction of ZnO has been fabricated.[30,31] The challenge for p-type doping ZnO is how to obtain samples with high hole concentration and high mobility.

2.0 GROWTH CHARACTERISTICS AND MORPHOLOGY EVOLUTION OF RF SPUTTERING DEPOSITED ZNO ON SAPPHIRE SUBSTRATE

2.1 Background

Many kinds of materials have been used as substrates for zinc oxide growth, such as glass, quartz, etc. These substrates are only suitable for growing polycrystalline materials. Sapphire is a ubiquitous substrate on which to grow various semiconductors. Sapphire is also the frequently used substrate for zinc oxide epitaxial growth owing to its low cost, the availability of large size crystals of good quality, its transparent nature, and stability at high temperature. High quality epitaxial zinc oxide films have been grown on sapphire substrates in this study.

2.1.1 Epitaxial Relationship of ZnO on Sapphire Substrate

Sapphire has a corundum structure. It belongs to R3c space group, and has rhombohedral lattice. The structure of sapphire consists of the closed-packed planes of oxygen atoms stacked in the A-B-A -B sequence, thus forming a closed-packed hexagonal sublattice of anions. The cations are placed in the octahedral sites of this basic array and form second set of closed-packed planes, which are inserted between the oxygen layers. To maintain charge neutrality, however, only two thirds of the octahedral sites are filled with cations. Figure 2-1 illustrates the (0001) oxygen closed-packed planes of sapphire (large circles), and projections of aluminum atoms (small circles). Figure 2-2 shows the (0001) plane of ZnO: zinc and oxygen atoms belong to the same planes as small and large circles, respectively.

The calculated mismatch between the basal ZnO plane and the basal sapphire plane is around 32%. In the case of growth of ZnO on (0001) α-Al_2O_3, there is a 30° rotation of the crystal orientation of the ZnO epilayer against the Al_2O_3 substrate. The actual mismatch is about 18% because of the 30° rotation alignment. The atomic arrangement is schematically represented in Figure 2-3. The [2 $\bar{1}$ $\bar{1}$ 0] orientation of ZnO aligns with the [1 $\bar{1}$ 0 0] direction of Al_2O_3, and the [1 $\bar{1}$ 0 0] direction of ZnO aligns with the [1 $\bar{2}$ 1 0] direction of Al_2O_3. It is seen that the

hexagonal Zn plane of ZnO is matched to the closed-packed oxygen plane of sapphire, which is rotated 30° with respected to the α-Al_2O_3 unit cell. This configuration establishes that Zn-O bonding at the interface controls the epitaxial orientation of the ZnO film. The actual mismatch is calculated as follows

$$\frac{\sqrt{3}a_{ZnO} - a_{sapphire}}{a_{sapphire}} = 0.18 . \qquad (2\text{-}1)$$

The relationship between the ZnO epilayers and the Al_2O_3 substrates has been investigated by X-ray diffraction φ scanning in this study.

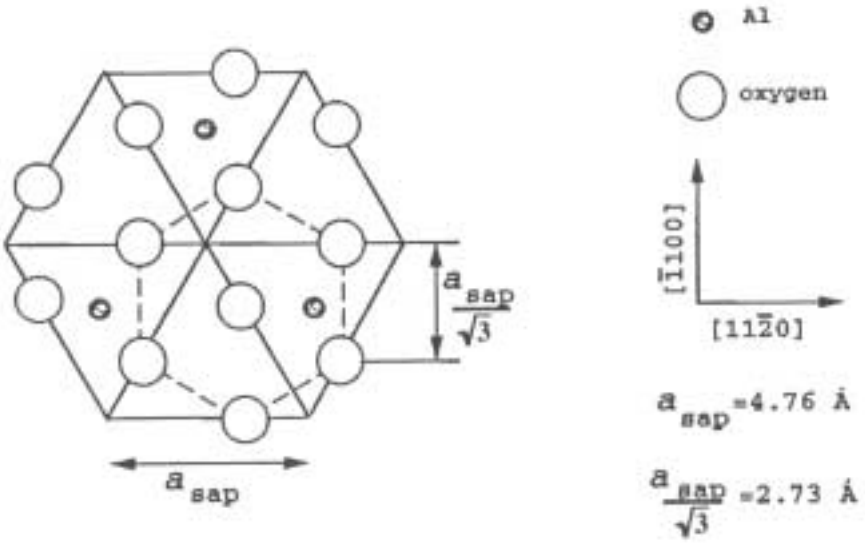

Figure 2.1 Top view of sapphire unit cell.

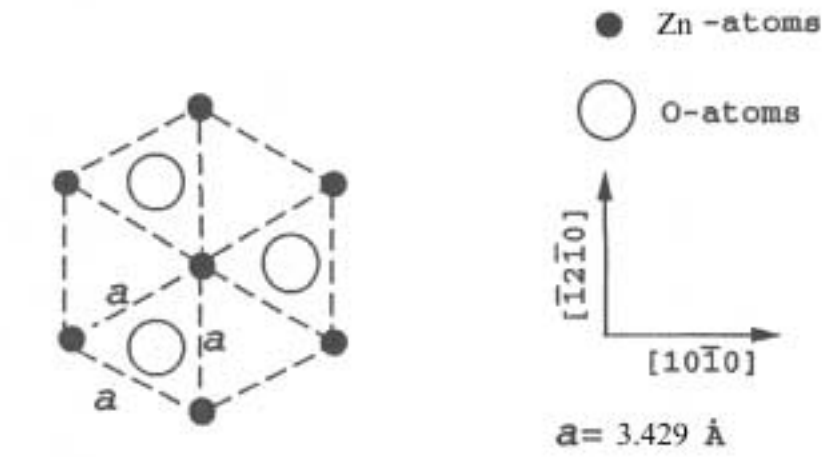

Figure 2.2 Top view of ZnO unit cell.

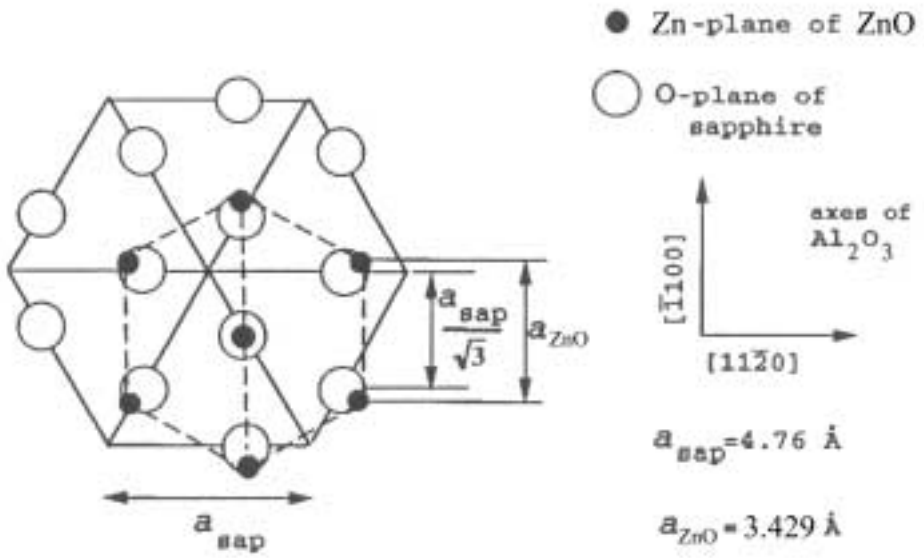

Figure 2.3 Schematic representation of in plane atomic arrangement in the case of ZnO (0001) on sapphire (0001).

2.1.2 General Morphology of Lattice-mismatched Systems

In the equilibrium theory of heteroepitaxial growth three growth modes are traditionally distinguished. They are Frank-van der Merwe (FM), Volmer-Weber (VW), and Stranski-Krastanow (SK) growth modes. They may be described as layer-by-layer growth (2D), island growth (3D), and layer-by-layer plus islands (Figure 2-4), respectively. The particular growth mode for a given system depends on the interface energies and on the lattice mismatch.

In lattice-matched systems, the growth mode is governed by the interface and surface energies only. If the sum of the epilayer surface energy γ_2 and of interface energy γ_{12} is lower than the energy of the substrate surface γ_1, $\gamma_2+\gamma_{12} < \gamma_1$, i.e. if the deposited material wets the substrate, the Frank-van der Merwe mode occurs. A change in $\gamma_2+\gamma_{12}$ alone may drive a transition from FM to VW growth mode. For a strained epilayer with small interface energy, initial growth may occur layer-by-layer, but a thicker layer has large strain energy, and can lower its energy by forming isolated islands in which strain is relaxed, thus the SK growth mode occurs.[32]

2.1.3 Equilibrium Phase Diagram of the Lattice-mismatched Heteroepitaxial Systems

The equilibrium morphology of the system is analyzed under the constraint of a fixed amount of material assembled in the islands. The treatment is based only on the scaling behavior of various contributions to the total energy, and leads to a criterion for whether Ostwald ripening occurs or optimum-sized coherent islands form. Assuming the total amount of deposited material is Q, whose lattice constant is d_A, and the substrate has lattice constant d_B, then the lattice mismatch ε is $(d_A - d_B) / d_B$. Due to the lattice mismatch, in equilibrium, one expects that a certain fraction of Q forms a wetting layer of Q_1, and the rest of the material $Q - Q_1$ is distributed in three-dimensional (3D) islands, in which Q_2 is assembled in 3D coherently strained islands of a given shape, and $Q - Q_1 - Q_2$ assembled in ripened islands. Considering the possible coexistence of small islands of optimum size L_{opt} and of ripened islands considerably larger than L_{opt}, which grows indefinitely. The total energy per unit cell of substrate is

$$E = E_{WL}(Q_1) + Q_2 E_{islands}(Q_2) + (Q - Q_1 - Q_2)E_{rip}\,. \qquad (2\text{-}2)$$

Here the energy of the wetting layer is $E_{WL}(Q_1)$, $E_{island}(Q_2)$ is the energy of 3D islands per atom, E_{rip} is the energy of "ripened" island, which can be obtained if one takes the limit island size $L \to \infty$ of $E_{island}(Q_2)$.[33]

Equation 2-2 defines the total energy of the wetting layer and 3D islands, where the latter may exhibit bimodal behavior, i.e., both small islands of size L_{opt} and larger islands considerably larger than L_{opt} may be present in the system. By minimizing the energy from the equation with respect to Q_1 and Q_2, the equilibrium phase diagram of a lattice-mismatched heteroepitaxial system as a function of the lattice mismatch and of the total amount of the deposited material Q is obtained. The domains of the phase diagram in Figure 2-5 correspond to the following physical situation.[33]

FM phase: The deposited material contributes to the pseudomorphic growth of the wetting layer, and the 3D islands are absent, reminiscent of the Frank-van der Merwe growth mode. The total energy has its minima at Q_2=0 and Q_1=Q, indicating that the thickness of the wetting layer coincides with the nominal thickness of the deposited material Q.

R_1 phase: Above a certain value of $Q_{c1}(\varepsilon)$, the total energy has new minima at Q_2=0 and $0<Q_1<Q$. This implies that after formation of a wetting layer, the excess material contributes to the formation of ripened islands. These ripened islands, being infinitely large, may have zero areal density.

SK_1 phase: The total energy develops new minima at nonzero Q_1 and Q_2 such that $Q_1+Q_2=Q$, i.e., the deposited material (Q monolayer) is distributed between Q_1 monolayer of the wetting layer, and finite islands accumulating Q_2 monolayer, similar to the Strsnski-Krastanow growth mode. It should be noted that with an increase in the total amount of deposited material Q, the thickness of the wetting Q_1 continues to grow sublinearly. This is consequence of island-island repulsive interactions: in the dilute system limit, the wetting layer thickness is constant.

R_2 phase: In this phase, the total energy has minima at $0<Q_1<Q$ and $0<Q_2<Q$, indicating that the deposited material is distributed between a wetting layer, finite islands, ripened islands. The finite islands formed in the SK_1 phase will be preserved, being stable against ripening. Thus finite and ripened islands coexist in the R_2 phase.

VW phase: For large mismatch and for small coverage, the total energy has its minima at $Q_2=Q$ and $Q_1=0$, indicating that all deposited material is accumulated in finite islands. Due to the large mismatch, the wetting layer is absent and the islands are formed directly on the substrate, similar to the Volmer-Weber growth mode.

SK_2 phase: By increasing Q, we reach the SK_2 phase. The behavior of the systems is different from SK_1 growth mode. For a given ε, islands are already formed in the VW phase. In the SK_2 phase, the island density and the island size remain unchanged, and a wetting layer starts forming until its thickness reaches 1 monolayer, at which point we enter the SK_1 phase.

R_3 phase: The total energy has its minima at $Q_1=0$ and $0<Q_2<Q$, indicating the formation of ripened islands. Finite islands formed in the VW mode are preserved, and coexist with the ripened islands. However, in contrast to the R_2 phase, the wetting layer is absent.

The lattice mismatch between the ZnO epilayer and the sapphire substrate is about 18%. It is predicted that the growth mode should be from the VW phase to the R_3 phase.

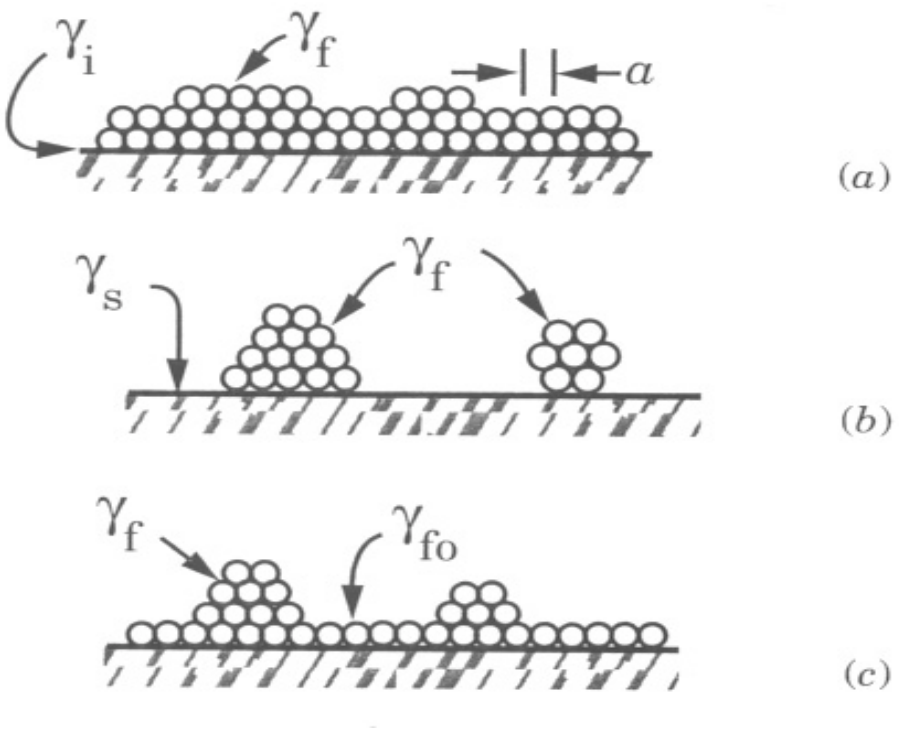

Figure 2.4 Three growth modes: (a) Frank-van Merwe mode; (b) Volmer-Weber mode and (c) Stranski-Krastanov mode.

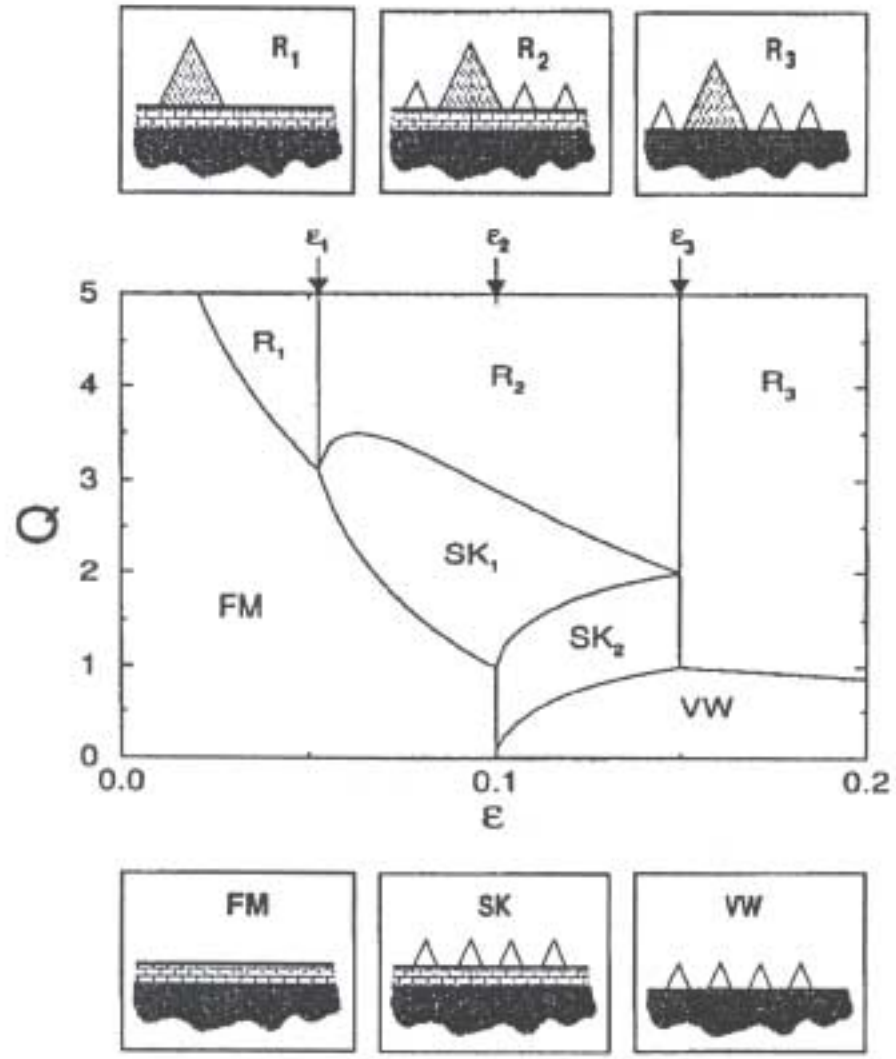

Figure 2.5 Equilibrium phase diagram of a lattice mismatched heteroepitaxial system.[33]

2.2 Epitaxial Growth of ZnO Films on Sapphire Substrates by rf Magnetron Sputtering

2.2.1 Introduction

Sputtering deposition is often used to grow ZnO films for various applications such as transparent electrodes, piezoelectric transducers, or varistors. Thin films for these applications are usually polycrystalline. Due to their poor crystalline quality, they are not suitable for optoelectronic applications, which require high quality thin films. High quality thin ZnO films have been obtained by plasma-assisted molecular-beam epitaxy (MBE) and metalorganic chemical vapor deposition (MOCVD). But these systems are expensive and complex. In this study, we grew high quality ZnO epilayers on sapphire substrates using a rf magnetron sputtering technique.

The quality of sputtered ZnO films is determined mostly by the following parameters.

Substrate temperature: The behavior of substrate temperature is very complicated and has different effects for different materials. Generally, high temperature deposition produces better oriented and denser films with good adhesion. This is believed to be due to enhanced surface adatom mobility. Deposition rate either decreases or stays the same with increasing temperature. In this study, the substrate temperature was varied in the range 400°C to 700°C.

Target-substrate distance: The target-substrate distance used in this study is in the range of 1.75 - 2.5 inches. If this distance is too small, highly kinetic particles can damage the film by striking the substrate and the uniformity of the film is not good. If the distance is too large, the sputtered particles will reach the substrate with low kinetic energy, which may result in poor adhesion and less dense films.

RF power: Normally rf power in the range of 40 to 70 Watts is used in the ZnO deposition. The power can be optimized for high quality film. High power may be required for low sputtering-yield materials.

Gas composition and pressure: Pure argon or mixture of argon and oxygen is often used for sputtering. Other gases may also be added depending on the need. Increasing the gas pressure usually increases the deposition rate, but beyond some point the deposition rate starts decreases.

2.2.2 Experimental Works

In this study, we have investigated the epitaxial growth of ZnO films on sapphire substrates. At present, sapphire is most popular substrate for growing high quality ZnO epilayers, which offer an opportunity for various ZnO based functional devices. Sputtering deposition provides a convenient and effective way to grow high quality ZnO films.

We used an rf magnetron sputtering system for the growth of ZnO film on sapphire. The sputtering target was 5N purity ZnO contained in a 2-inch diameter copper cup. The ZnO target was mechanically clamped to a water-cooled magnetron gun as the source for the deposition. The substrate was [1000] sapphire. The sapphire wafer was cleaned using the following procedure.

- Dipping in 1 volume NH_4OH plus 1 volume H_2O_2 solution for 3 minutes.
- Ultrasonic cleaning in deionized water for 5 minutes.
- Dipping in 1 volume HF plus 1 volume HNO_3 solution for 5 minutes.
- Rinsed in deionized water for several minutes.
- Blown dry with pure N_2.

After cleaning the wafer was immediately loaded into a growth chamber. The sputtering system was then pumped to a base pressure of 10^{-6} Torr by a turbomolecular pump, which is backed by a rotary vane pump. Prior to deposition the substrate temperature was raised to 700-750°C and the target was presputtered for 5-20 minutes in a pure Ar or Ar/O_2 mixture ambient to remove the contamination while the shield was closed to avoid the unintentional deposition on the substrate. A 0.005-3.0 μm-thick ZnO film was deposited in Ar or Ar/O_2 ambient by controlling the open time of the shield. The substrate temperature should be held at the desired temperature value. The following deposition parameters were optimized to obtain high quality epitaxial ZnO films.

Table 3 Conditions for ZnO Deposition

Target to substrate distance	1.75 inch
RF power	70 W
Gas	Ar or Ar/O_2
Gas pressure	2.0 mTorr
Substrate temperature	700°C
Deposition rate	120 Å/min.

X-ray diffraction was used to characterize the structure of the films. The nucleation of ZnO on sapphire was studied by atomic force microscope (AFM) and scanning electron microscope (SEM). The electrical properties were investigated using a TLM technique. The effect of film thickness on material properties was also studied.

2.3 Results and Discussion

2.3.1 Structure

X-ray diffraction was employed to study the crystal quality of the ZnO film. XRD θ-2θ scannings show the ZnO(0002) peak at 2θ = 34.4°, which corresponds to a *d* spacing of 2.603Å, in agreement with the lattice constant of bulk ZnO (c = 5.2066 Å) (see Figure 2-6). A 0.2 μm thick ZnO film was deposited at 700°C in an ambient of Ar/O_2 (95/5) gas. The peak at 2θ = 41.6° corresponds to sapphire single crystal (006) plane. The full-width-at-half-maximum (FWHM) of ZnO peak was measured to be 0.33° while the sapphire peak shows 0.1° of FWHM. Besides the instrumental broadening, which can be calibrated with a single crystal sapphire substrate, the FWHM of a Bragg peak in θ-2θ scanning includes two effects, crystalline size (along the direction normal to the substrate surface) and the non-uniform strain. Assuming the non-uniform strain is insignificant, and the instrumental broadening is 0.1°, the broadening due to the crystalline size is 0.23°. This number is quite comparable to those of typical ZnO films grown by MOCVD or MBE.

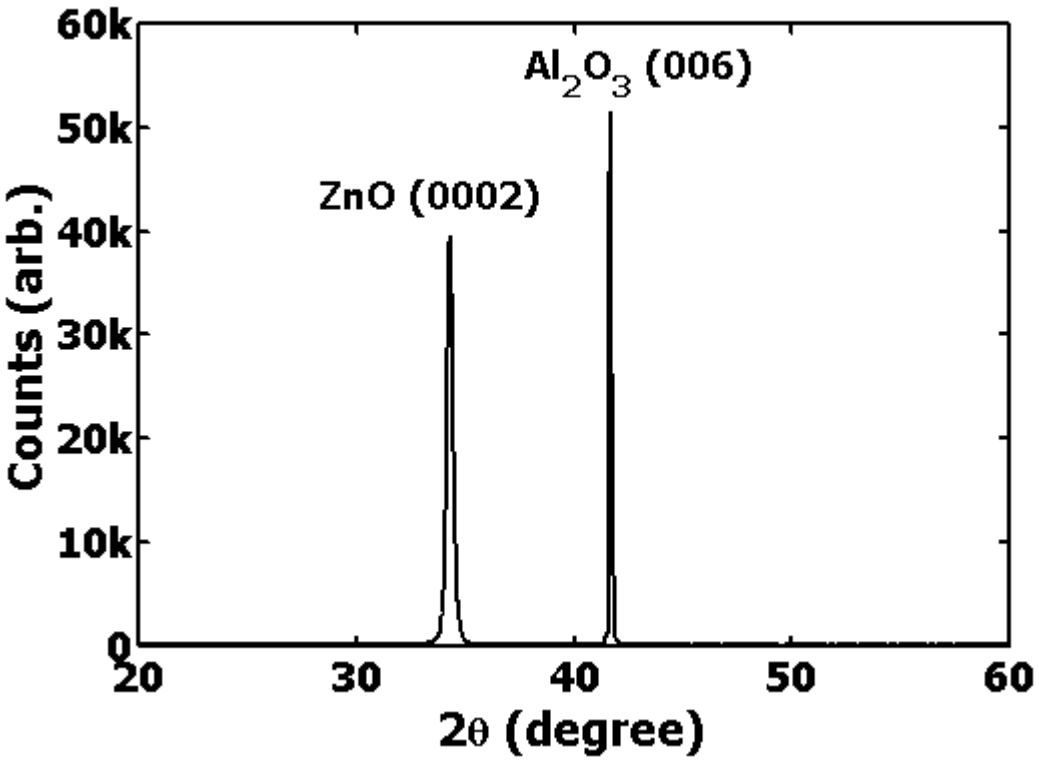

Figure 2.6 X-ray diffraction θ-2θ scanning of a ZnO film on sapphire deposited by rf sputtering.

The x-ray diffraction peaks obtained by a θ-2θ scanning corresponds to the crystalline planes parallel to the substrate surface. Therefore, the information on the structural perfection (or inperfection) of a film along the direction perpendicular to the substrate surface can be obtained from the absence (or presence) of unwanted peaks and the sharpness of the main peaks. As discussed above, the θ-2θ scan on the ZnO film shows a single peak with extremely strong intensity in the range of 20 to 60 degrees, and the peak corresponds to ZnO(0002) plane. This result clearly indicates that the crystalline planes parallel to the substrate surface are almost perfectly stacked (as single crystal case) along the growth direction. The XRD θ-2θ scan, however, does not reveal any information on the crystalline nature along other two directions (i.e., the directions parallel to the substrate surface).

The structural transition of ZnO growth from its initial nucleation was investigated by growing different thickness ZnO films, starting from 0.005 μm to 0.2 μm. Under the same conditions, a set of samples with different thickness was prepared by controlling the deposition time. The nominal film thickness is 0.005 μm, 0.01 μm, 0.02 μm, 0.04 μm, and 0.2 μm. Figure 2-7 shows the FWHM of Bragg peak (dotted line is the FWHM of the sapphire substrate, which is constant and corresponds to the instrumental broadening.) for variously different-thickness ZnO films. The FWHM monotonically increases with the decrease of the thickness. This is due to the decrease of the ZnO film thickness and the nonuniform stress in the film.

The finite crystalline size of the crystal versus the width of the diffraction curve is given by Scherrer formula[34]

$$B = \frac{0.9\lambda}{t\cos\theta_B}, \qquad (2\text{-}3)$$

where λ = 1.54Å is the wavelength of X-ray, t is the diameter of the particle, for single crystal, it is the thickness of the crystal, θ_B is Bragg angle of the reflection plane. This relationship is plotted in Figure 2-7 as dashed line. Comparing this with the experimental data, a large difference is observed. Even after the subtraction of the instrumental broadening (the FWHM of sapphire substrate), the measured values are much larger than the calculated values. Furthermore,

this difference increases with the decrease of film thickness (Figure 2-8). As we mentioned above, this is attributed to the nonuniform strain of the films. The origin of this strain might be thermal and/or lattice mismatch related. We know that there is very large lattice mismatch (18%) between the ZnO epilayer and the sapphire substrate, which will result in considerable compression in the epilayer. The large thermal mismatch (the in-plane thermal expansion coefficient of sapphire is more than two times greater than that of ZnO) makes the situation even more serious during the postgrowth cooling period.

The effect of uniform strain on the XRD curve can be shown on the Bragg angle shift with the thickness change. Figure 2-9 is the plot of θ_B of ZnO(0002) versus film thickness (θ_B was calibrated by the substrate value). The results show that the Bragg angle shifts to the lower angles with decrease of the ZnO film thickness, i.e., the distance between the planes parallel to the substrate surface increases with the decrease of the film thickness, referring to Bragg's law

$$\lambda = 2d \sin\theta , \qquad (2\text{-}4)$$

where λ is wavelength of the x-ray, 2θ is the diffraction angle which is the angle between the diffracted beam and the transmitted beam, d is the distance between the parallel (*hkl*) crystal planes. This suggests that thinner films (especially thinner than 0.01 μm or less) are more compressively strained along the in-plane direction.

The effect of strain, both uniform and nonuniform, on the direction of x-ray reflection is illustrated in Figure 2-10.[34] A portion of an unstrained grain appears in (a) on the left, and the set of transverse planes shown has uniform equilibrium spacing d_0. The diffraction line from these planes appears on the right. If the grain is given a uniform tensile strain at right angles to the reflection planes, their spacing becomes larger than d_0. The corresponding diffraction line shifts to lower angles, as shown in (b). In (c) the grain is bent and the strain is nonuniform; on the top (tension) side the plane spacing exceeds d_0, on the bottom (compression) side it is less than d_0, and somewhere in between it equals d_0. We may imagine this grain to be composed of a number

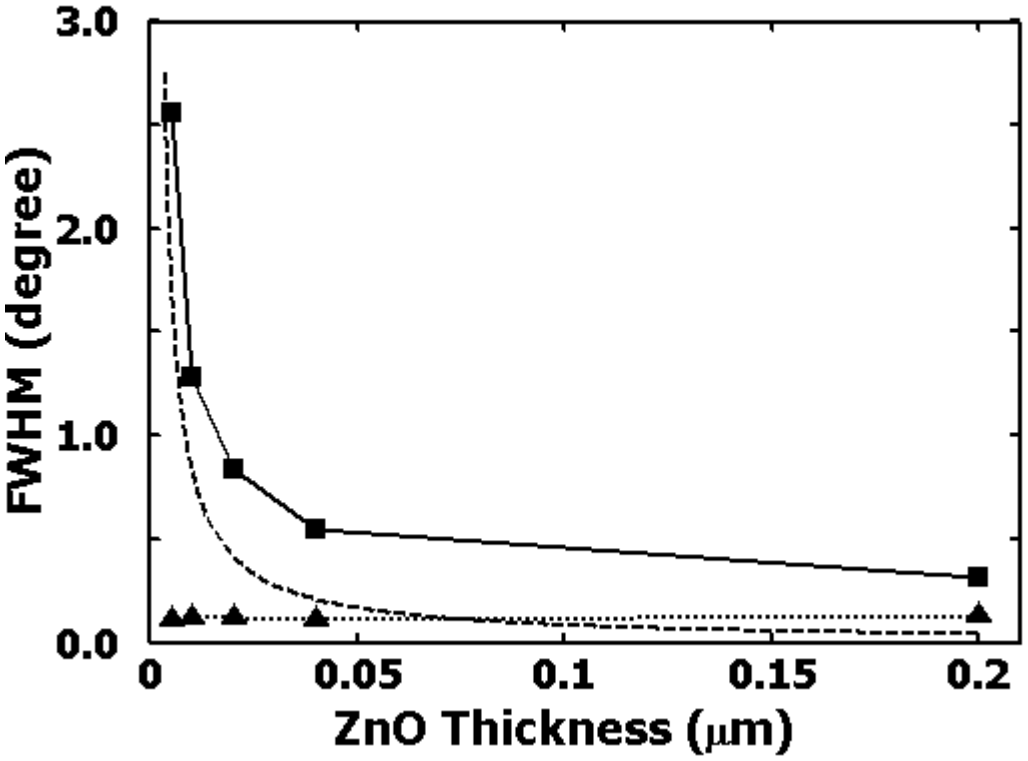

Figure 2.7 XRD θ-2θ scanning FWHMs of ZnO (0002) for films with different thickness and their sapphire substrates (Squares represent ZnO's data; triangles represent its sapphire substrate's).

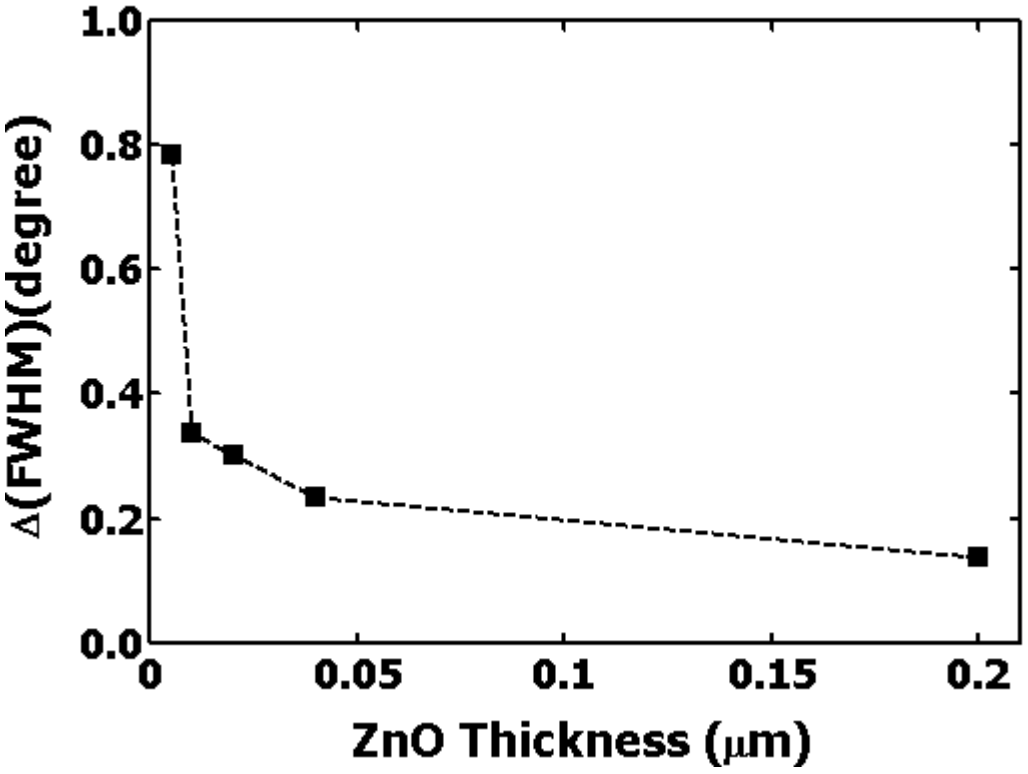

Figure 2.8 XRD θ-2θ scanning FWHM difference of ZnO (0002) between measured and calculated values of films with different thickness.

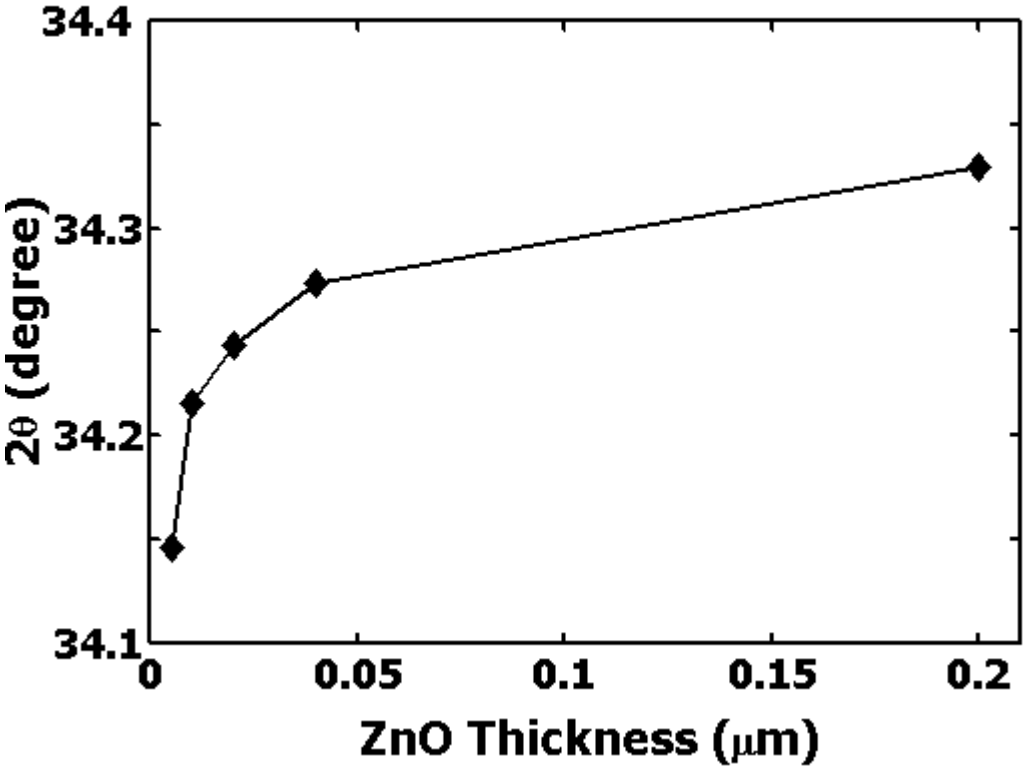

Figure 2.9 XRD 2θ of ZnO (0002) plane for films with different thickness.

of small regions in each of which the plane spacing is substantially constant but different from the spacing in adjoining regions. These regions cause the various sharp lines indicated on the right of (c) by the dotted curves. The sum of these lines, each slightly displaced from the other, is the broadened diffraction line shown by the full curve, which is the one experimentally observable.

In the case of heteroepitaxy, when the lattice constant of the epilayer material is different from that of substrate, this difference results in a lattice mismatch between the epilayer and the substrate. But as long as the lattice misfit is below approximately 10%, it is possible to grow an epitaxial film, which is in complete registry with the surface (i.e., it is pseudomorphic up to a thickness called critical thickness) [35]. Beyond the critical thickness, dislocations are produced and the strain relaxes. The pseudmorphic films below critical thickness are thermodynamically stable, i.e., even though they have strain energy, the relaxed state with dislocations has a higher free energy. These ideas are schematically illustrated in Figure 2-11. It shows how an overlayer with a lattice constant larger than the substrate grows below critical thickness. Above the critical thickness, thermodynamics favors dislocation generation. If the epilayer lattice constant is larger than that of substrate, a compressive stress is caused and the *d* value increases from its original value, which will results in Bragg angle (corresponds to the (*hkl*) plane parallel to the surface of the film) shifts to lower value. On the contrary, when the epilayer lattice constant is smaller than that of substrate, a tensile stress is caused and the *d* value decreases from its original value, which will result in Bragg angle shift to higher value. The *d* value of epilayer with dislocation relaxation changes less, so does the Bragg angle, but the dislocations will cause the broadening. Our experimental results are consistent with the first case, i.e., there is a compressive stress in the film, and the compressive stress increases with the decrease of the film thickness.

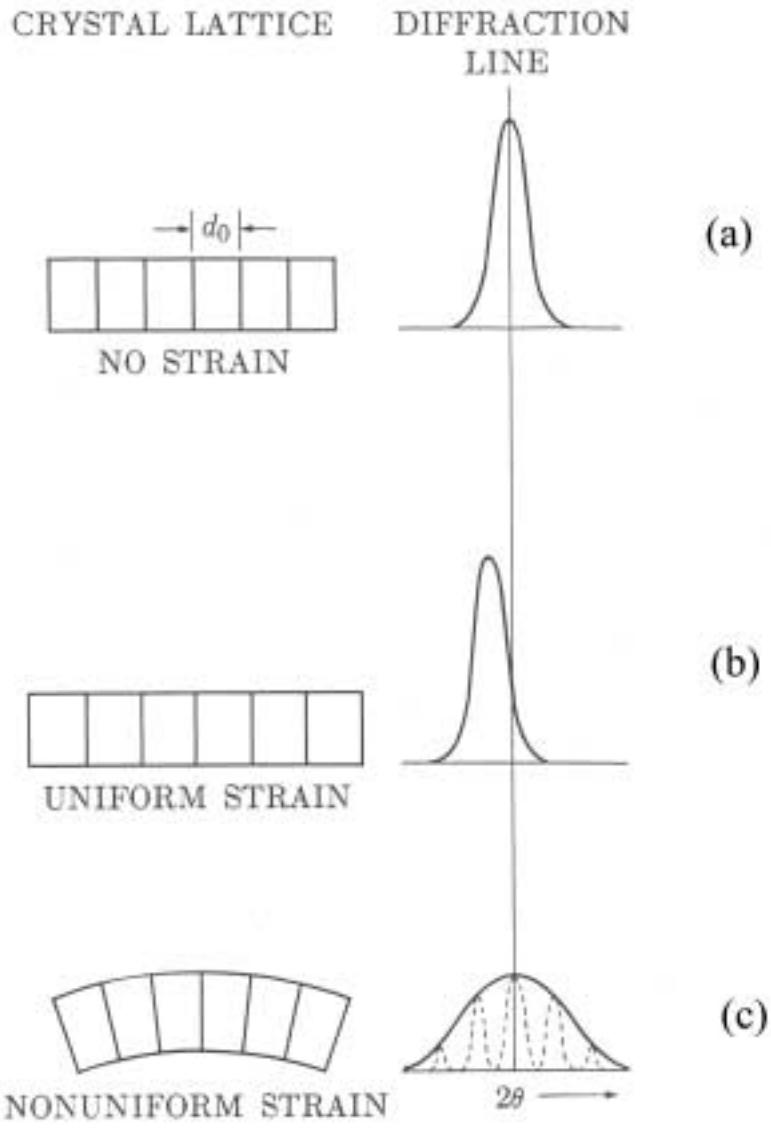

Figure 2.10 Schematic representation of effect of strain on the XRD patterns.[34]

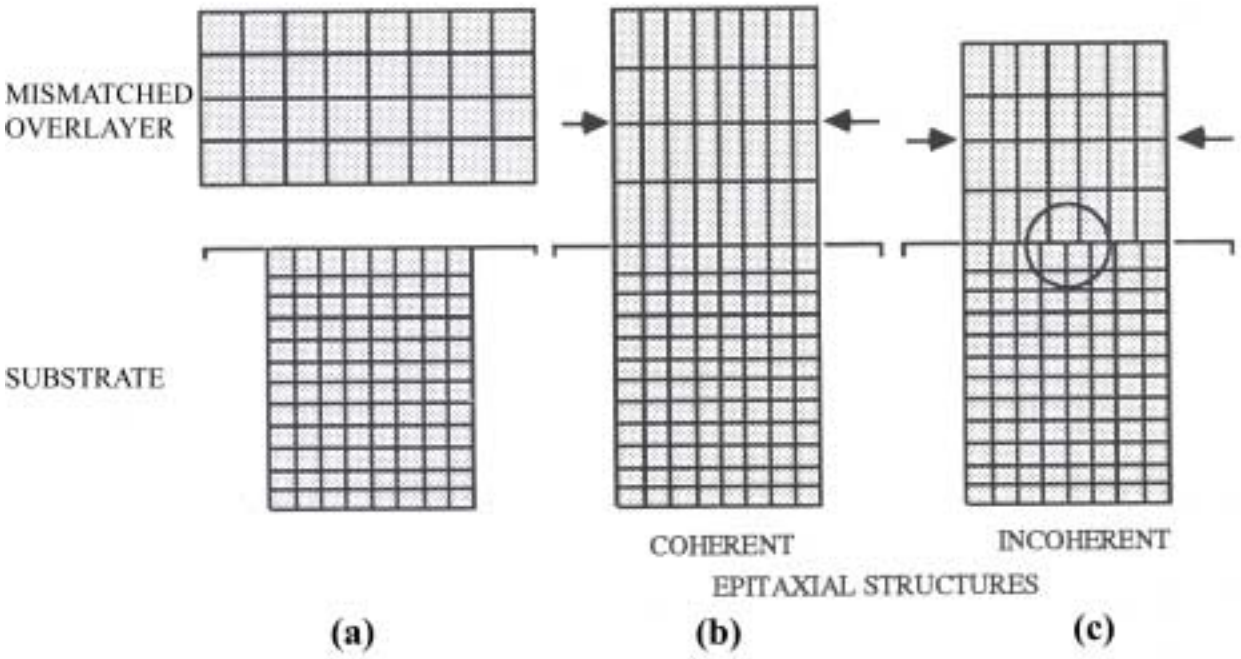

Figure 2.11 (a) A strain layer structure is formed forcing a mismatch overlayer on the substrate; (b) coherent strain epilayer and (c) incoherent epilayer.

2.3.2 Epitaxial Relationship Between ZnO Epilayer and Sapphire Substrate

In most semiconductor devices (including ZnO), device performances are critically affected by the structural imperfections of semiconductor materials. Single crystal films, therefore, are the most preferred over other films that show lower order of crystallinity such as polycrystalline films. The XRD θ-2θ cannot distinguish between polycrystalline films and single crystal films. In order to measure the in-plane crystallinity of the films, we performed X-ray pole Figure and phi scan analysis.

Figure 2-12 shows the XRD pole Figure measurement result of a ZnO film (100nm) grown on a sapphire substrate. The six-fold symmetric pattern is represented six (101) peaks of the ZnO, which has hexagonal wurtizite structure with c-axis normal to the sapphire basal plane, i.e., $(0001)_{ZnO}||(0001)_{Sapphire}$. This result clearly shows that ZnO film is grown epitaxially, i.e., as a single-crystal-like film.

Figure 2-13 represents the phi-scan of the same ZnO film in Figure 2-12. The six (101) diffraction peaks separated by 60° demonstrate the six-fold symmetry as we expected. Plotted with ZnO peaks are the three-fold-symmetry (104) planes of sapphire, which has rhombohedral structure. These two plots have 30° shift, which demonstrates a rotation of 30° of these two structures, i.e., the [1 $\bar{1}$ 0 0] and [1 $\bar{2}$ 1 0] directions being aligned for the ZnO film and the Al_2O_3 substrate (as in Figure 2-3), which is analyzed above and also demonstrated by other group.[9] The 30° rotation of the crystal orientation of the ZnO epilayer against the Al_2O_3 substrate occurs because the ZnO lattice aligns itself with oxygen sublattice in Al_2O_3, not Al sublattice; with this, the lattice mismatch is reduced from 32% to 18%.

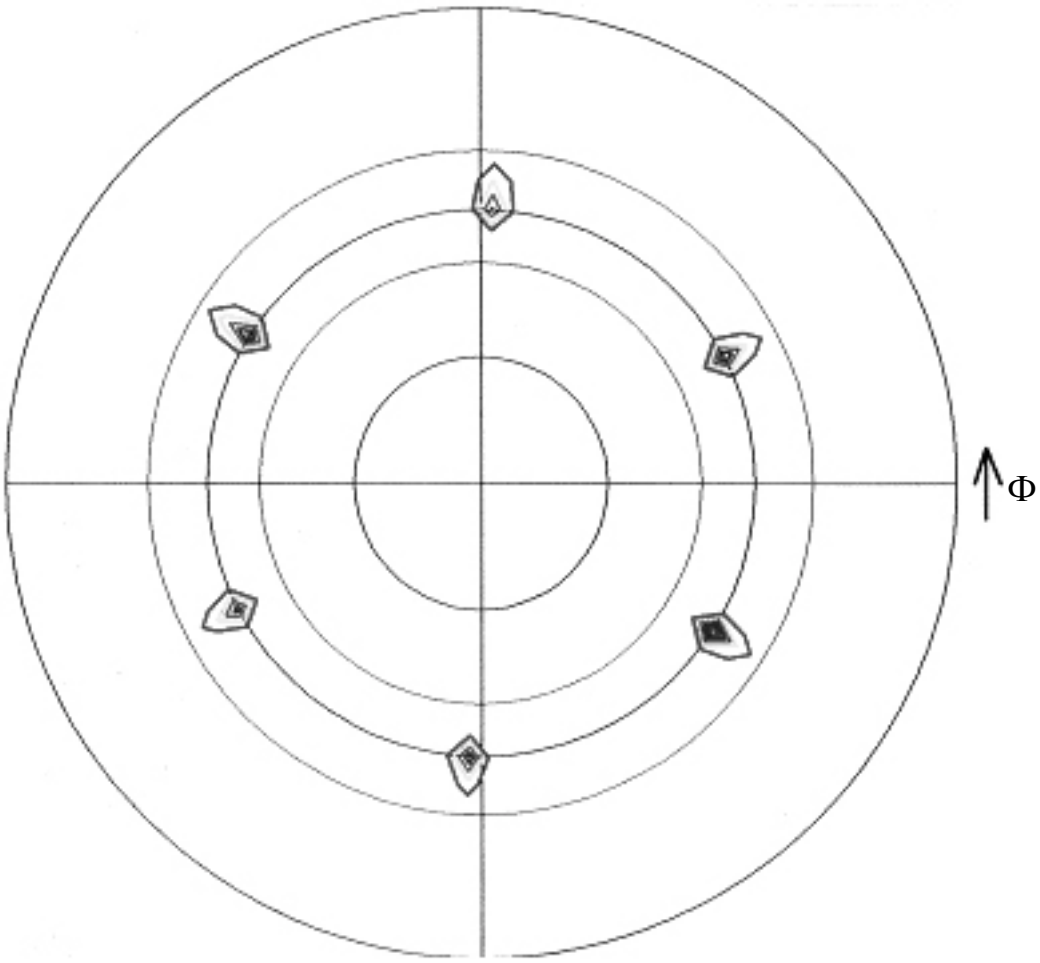

Figure 2.12 X-ray pole Figure of a rf sputtering deposited ZnO film on sapphire.

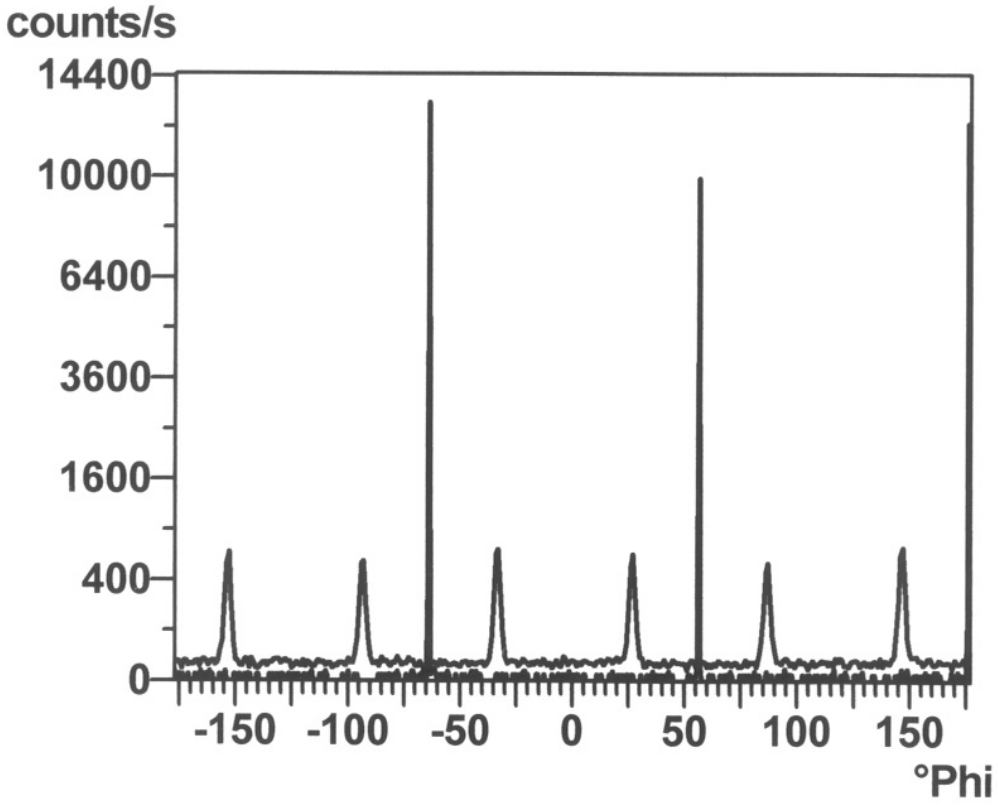

Figure 2.13 Phi scanning of ZnO epilayer (same as Figure 2-12) on (0001) sapphire (six relative weakly peaks are ZnO (101), and the three stronger and sharper peaks are sapphire (104)).

2.3.3 Effect of the Deposition Ambient on the Structures of the ZnO Films

It is common for the unintentional as-deposited ZnO film to be oxygen deficiency, which results in n-type ZnO. The Kroger-Vink-diagram (Figure 1-3) shows that increasing the O_2 pressure will reduce the O_2 deficiency of ZnO film and the film is more stoichiometric and the properties of the film is improved.[36] It reduces the electron concentration and increases the resistivity of film. Our electrical measurement results confirm this derivation. The effect of the deposition ambient on the structures of the ZnO films can be shown from XRD measurement. There is little difference of FWHM for the films deposited in pure Ar ambient and in Ar/O_2 (95/5) ambient (As in Figure 2-14). The ambient has no significant effect on the structures of ZnO films in this study.

2.3.4 Effect of the Postdeposition Annealing on the Structures of the Films

The effect of the annealing on the structure was studied by annealing the samples at 800°C or 1000°C. The crystallographic orientation of these annealed samples has been characterized by XRD θ-2θ scans before and after postdepositon heat treatment. It is obvious that the films' qualities were improved after the heat treatment. Annealing at 800°C had little effect on the film, whereas annealing at 1000°C greatly improves the (0002) orientation of the films. After annealing, the ZnO (0002) diffraction peak intensity increases for specimen with different thickness. Figure 2-15 shows the decrease of FWHM of the samples after annealing. It seems the postdepostion heat treatment reduces nonuniform strain and increases the crystalline size.

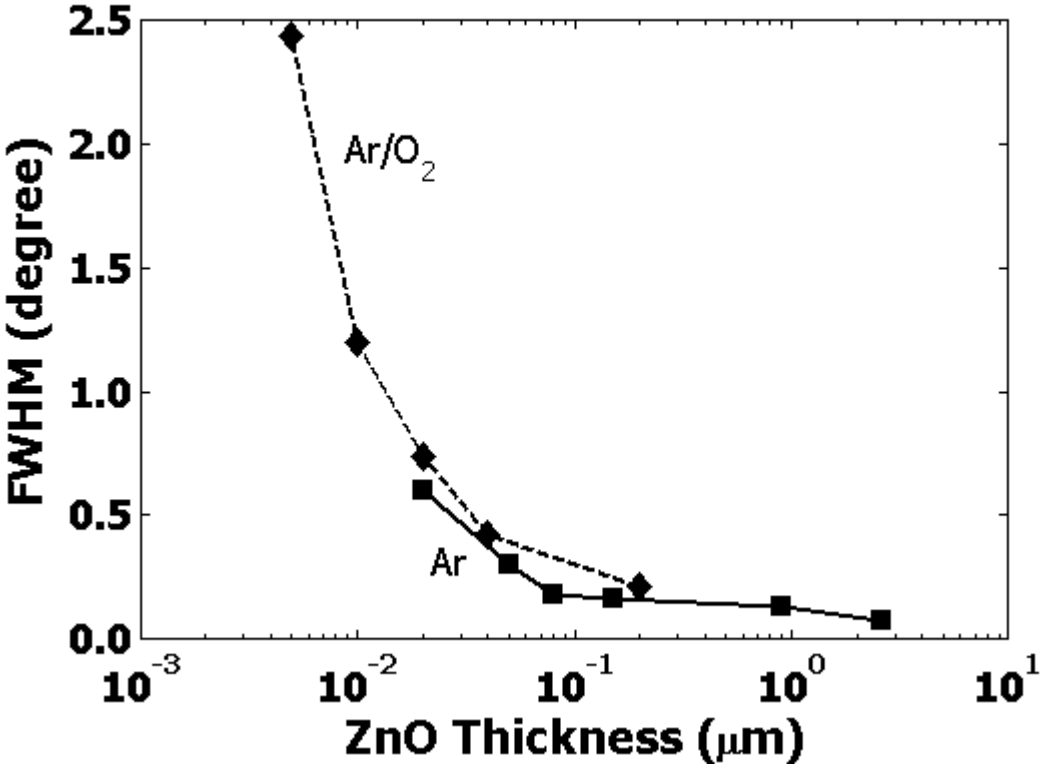

Figure 2.14 XRD FWHMs of ZnO (0002) as a function of film thickness (Diamonds, deposited in Ar/O_2 ambient; squares, deposited in Ar ambient)

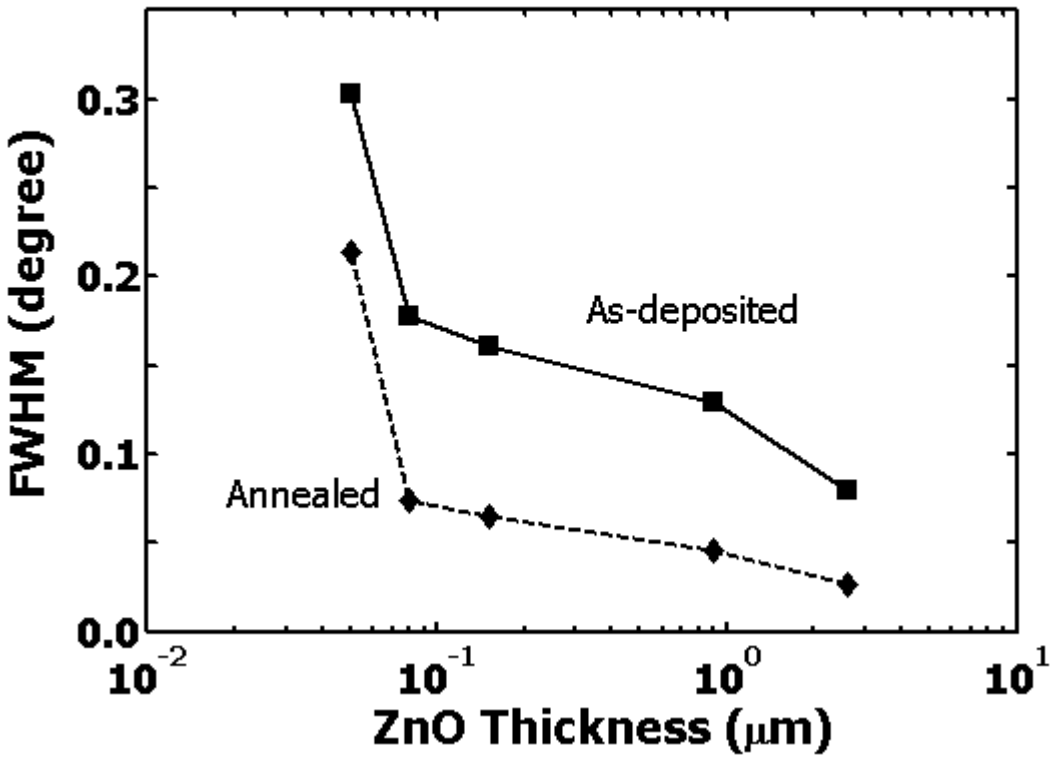

Figure 2.15 XRD FWHMs of ZnO (0002) as a function of film thickness. (Diamonds, as-deposited; squares, after annealing)

2.3.5 Growth Mechanism of ZnO Epilayer on Sapphire

We investigated the early-stage growth behavior of ZnO (2 to 20 nm thickness) on sapphire by performing electrical (sheet resistance measurement), structural (X-ray diffraction) and morphological (atomic force microscopy) characterizations. It is found that ZnO grows as mostly discontinuous, three-dimensional (3D) islands that are highly-aligned (with resolution-limited mosaicity) but incommensurate (with partial strain-relaxation) in 2 to 5 nm thickness range. In 5 to 10 nm range, the islands coalesce/merge and become fully connected, showing development of mosaicity (primarily with out-of-plane tilt).

ZnO films were grown on sapphire (0001) substrates at 700°C using radio-frequency (rf) magnetron sputtering. A 5N-purity ZnO target was sputtered in Ar/O_2 (95/5) ambient with the following deposition parameters: target-substrate distance of 1.75 inch, rf power of 70 W. and gas pressure of 2 mTorr. Under these conditions, ZnO deposition rate of 0.3nm/sec was obtained, as measured/calibrated over a broad range of film thickness using a surface profilometer (Tencor Alpha-step 200). Based on this calibration result, 2 to 20-nm-thick ZnO films were then deposited by controlling the deposition time. The grown materials were characterized by X-ray diffraction ($\theta/2\theta$, rocking curve, pole Figure, and reciprocal space mapping), atomic force microscopy (AFM), and electrical resistivity measurement. Although the results are not shown here, XRD Ψ-scan and pole Figure analysis results reveal that ZnO orients itself from the early stage of growth (2-5 nm) in such a way that the lattice mismatch is small (i.e. reduced 18% level from the nominal mismatch of 32%) and anisotropic interfacial energy is lowed.[37] In other words, ZnO grows with its lattice 30-degree rotated in-plane with respect to sapphire, showing an epitaxial relationship of ZnO[11$\underline{2}$0]//sapphire[$\underline{1}$010] along the in-plane direction and ZnO[0002]//sapphire[0002] along the vertical direction. Figure 2-16 shows the ω - rocking curves of the ZnO(0002) diffraction peak from the ZnO samples with nominal thickness 2, 5, 10 and 20 nm, which corresponds to deposition time 7, 17, 34, and 67 seconds, respectively. Two distinct features are clearly observed: a sharp specular peak with a full-width-half-maximum (FWHM) of 0.02°, which is resolution limited, and a much broader diffuse part with FWHM of 2 to 3°. The 2-nm-thick sample shows a specular only, which indicates that ZnO grew well aligned

to substrate with negligible degree of mosaicity, i.e. resolution-limited amount of out-of-plane tilt. At 5 nm thickness, a broad diffuse part begins to develop, although intensity remains negligible. The specular peak intensity grows as thickness increases 2 nm to 10 nm, and then stays at the same level for thickness greater than 10 nm (shown in Figure 2-17). A broad diffuse peak is clearly observed at 10 nm and the intensity grows as thickness further increases. It is interesting to note that the emergence of a broad peak coincides with the on-set of saturation of the specular peak intensity. This suggests that the ZnO growth evolves through two regimes divided at around 10 nm.

The microstructural evolution was further examined by performed X-ray diffraction reciprocal space mapping on the samples discussed above. Figure 2-18 shows the contour maps (plots on the angular domain) of ZnO (0002) and sapphire (006) peaks obtained by $\omega/2\theta$ scans for various ω. The ZnO peaks locate at the same ω value with the sapphire peaks, indicating that the c-axis of ZnO well aligned to the same direction as that of substrate. The ZnO peak of the 2-nm-thick sample is found narrow along the ω -direction and elongated along the $\omega/2\theta$ direction. (It should be noted here that the ZnO peak apparently looks narrower than sapphire. This is due to the fact that the intensity range in these plots was chosen such that ZnO peaks are better resolved than sapphire. In 2-nm case, for example, the outer-most line corresponds to an intensity level just above the background.) The FWHM value along the ω-direction is virtually resolution-limited, indicating that the out-of-plane tilt of ZnO is negligible. Along the $\omega/2\theta$ direction, the ZnO peak extends in a broad range. This broadening is attributed to mostly the small thickness of ZnO and also possibly to the nonuniform strain along the vertical (*c*-axis) direction. Separation of the two peaks along the vertical direction corresponds to different *d*-spacing values of ZnO(0002) and sapphire(0002) planes. Counting the sapphire peak as an unstrained reference and calculating the average *d*-spacing of ZnO from the center of the elongated peak, the 2-nm-thick ZnO is found compressively strained to ~5% level (Figure 2-19). This number is much smaller than the lattice-mismatched between ZnO and sapphire (18%), and indicates that strain-relaxation has already occurred to a significant degree in this film. This is not surprising in view of the fact the critical layer thickness for pseudomorphic growth of ZnO on sapphire is estimated to be one or two monolayer due to the large lattice-mismatch.[38] This partial strain-relaxation might be explained by domain epitaxial growth and interfacial misfit

dislocations generation, which are often observed in large lattice mismatch system.[39] The domain size basically corresponds to the repeat distance across which lattice match is maintained with reduced amount of strain. In each domain, *m* units of substrate lattice match with *n* epilayer lattices along with *(m-n)* number of misfit dislocations, where *m* and *n* are integers. A domain size na_x of the substrate does mot match perfectly with mb_x of the epilayer so that a residual mismatch strain is present in the film, given as $2(mb_x - na_x)/(mb_x + na_x)$ along the *x*-direction, where a_x and b_x are in-plane lattice constant of epilayer and substrate, respectively. In a domain with nine Al_2O_3-lattice matching with eight ZnO-lattice, for example, the mismatch strain is reduced to 5%, significantly lower than the intrinsic mismatch between ZnO and sapphire (18%). (In this case, each domain will be of ~3nm size and contain one misfit dislocation on average.) Dislocation generation is expected to cause a nonuniform distribution of strain in ZnO, which is believed to have contribution to the broadening of ZnO peak in Figure 2-18(a). Besides the interfacial dislocations generation, elastic deformation of 3D islands (and also of substrate) might also have contributed to the partial relaxation, similar to the case of coherent Stranski-Krasranow island formation observed in Ge/Si and InGaAs/GaAs material systems.[40, 41] At 5 nm thickness, the ZnO peak has started broadening in the ω direction (though it still remains narrow), and become less elongated along the $\omega/2\theta$ direction. Compared with the 2 nm case, the ZnO is found to have shifted towards the sapphire peak, indicating that strain has further relaxed. Impingement and coalescence of small islands might have occurred as will be discussed below in the AFM results. This would result in subgrain boundary formation, which in turn might induce tensile strain, reducing the overall amount of compressive strain in ZnO, as observed in the Volmer-Weber thin film.[42] At 10 nm, a broad peak associated with mosaicity has grown dramatically in breadth (along the ω-direction) and intensity, and appears superposed to the narrow one discussed above. This area mapping result well matches the ω-rocking curve profiles shown in Figure 2-17, i.e. a sharp specular peak superposed to a broad diffuse component. The continued presence of a specular component and no sign of attenuation of the peak intensity suggest that the diffuse component is from the region/layer that formed after the initial 5-nm ZnO growth. Considering the fact that the diffuse component corresponds to out-of-plane tilt,[43] the mosaicity development might have happened through the subgrain boundary development as

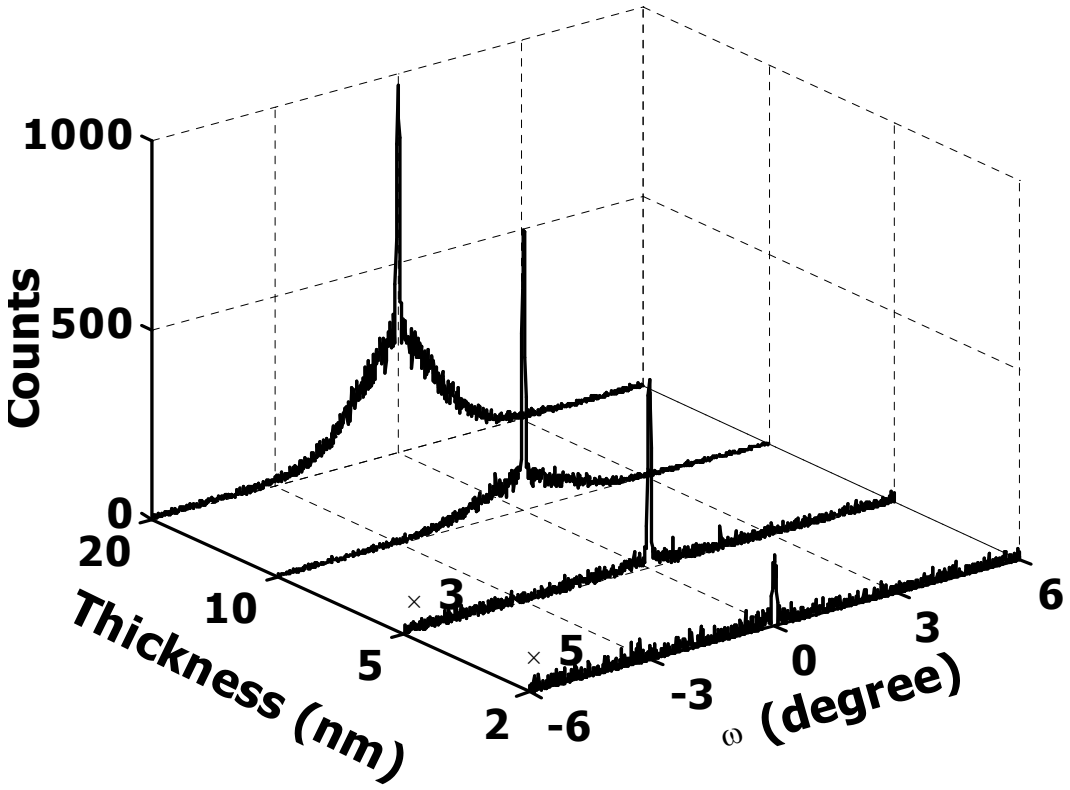

Figure 2.16 Evolution of the XRD ω-rocking curves of the ZnO (0002) diffraction peaks at the early stage of ZnO growth.

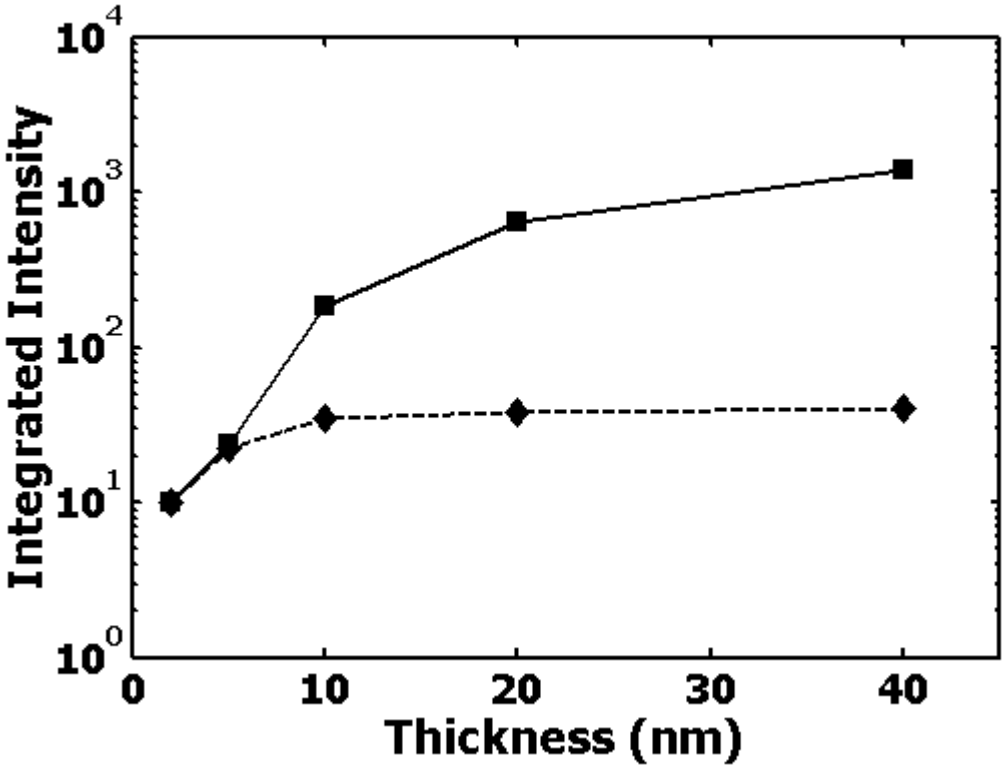

Figure 2.17 Integrated intensity of omega rocking curves as a function of ZnO film thickness (Squares represent the total peak intensity; diamonds represent the spectral parts).

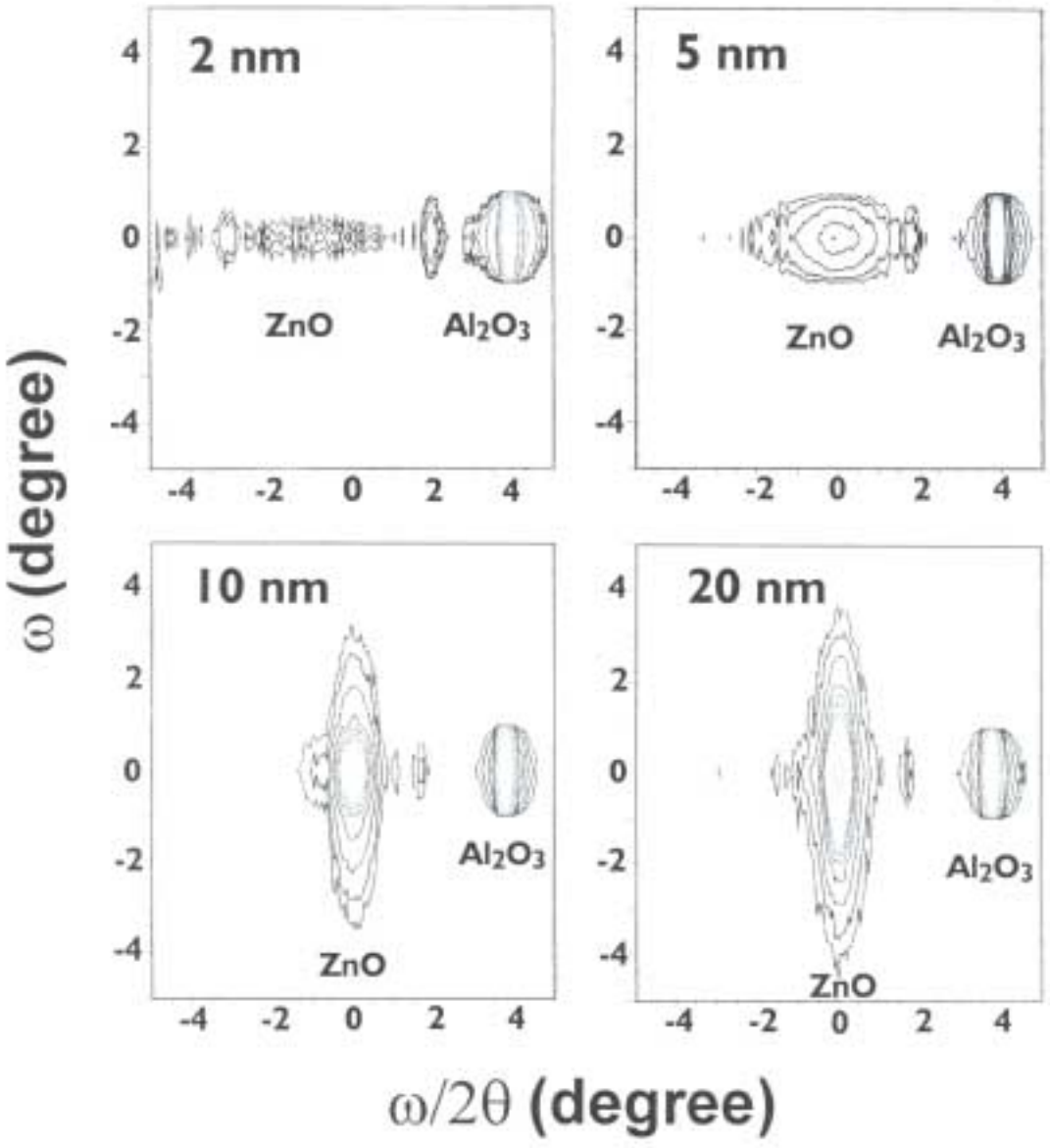

Figure 2-18 The reciprocal-space contour maps of the ZnO(0002) and Al_2O_3(006) peaks at thickness 2, 5, 10, and 20 nm.

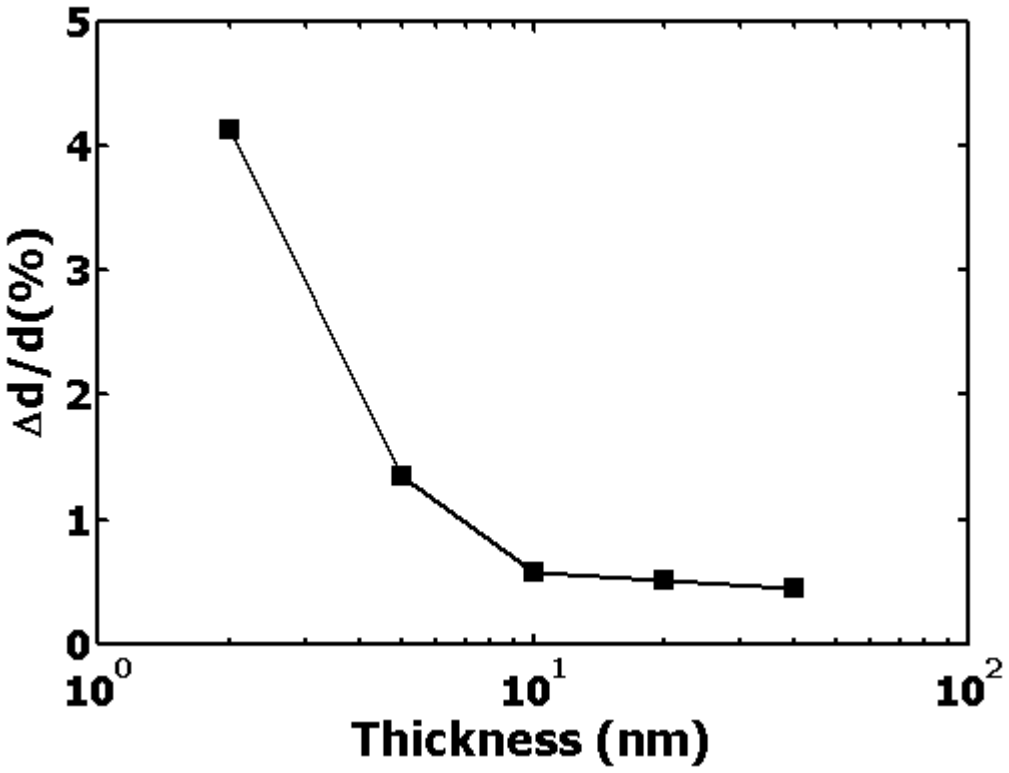

Figure 2-19 Lattice strain of ZnO epilayers as a function of film thickness.

3D islands coalesced and merged, fully covering the substrate surface. The separation between ZnO and sapphire spots remain the same indicating that strain relaxation did not continue. At 20 nm, the broad diffuse component grew stronger while the strain remains at the same level.

In order to elucidate the topographical nature of ZnO grown at each stage, an atomic force microscopy (AFM) analysis was performed on the samples discussed above. Digital Instruments NanoScope III Dimension 5000 was used in scanning 500nm×500nm area of each sample surface. Figure 2-20(a) to (d) shows the perspective view and sample section profiles of ZnO with nominal thickness of 2, 5, 10, and 20 nm, respectively. At 2 nm thickness, 3D islands features are observed with a tendency toward showing a bimodal size distribution, i.e. a mixture of relatively large islands with 7-8 nm height and 20-30 nm width and smaller ones with 2-3 nm height and 10-20 width. Some islands reveal finer peak profiles, indicating that they consist of islands impinged/coalesced together. At 5 nm, islands growth continued, forming larger ones with 10-15 nm height and 30-40 nm width. It is interesting to note that the islands show relatively uniform size distribution. The island density is counted to be approximately $10^{11}/cm^2$. Some of the larger islands clearly show coalescence of smaller ones. At 10 nm, a dramatic change is observed, i.e., majority of islands merged together and connected with neighbor ones. Thus, the density of major islands dropped significantly. Whereas the island width dramatically increased through merging, the height of most islands did not increase much. This suggests full coverage of substrate surface with ZnO. It is interesting to note that this coincides with the major development of mosaicity (i.e., out-of-plane tilt) as observed in the XRD from the same sample. At 20 nm, islands merge/growth continued forming major islands of around 20-25 nm height and 100-150 nm width. Between the major islands, small ones are observed, which provide connectivity of entire film.

In order to characterize the connectivity of islands and their evolution, we have performed electrical resistivity measurement. 100-nm-thick Al electrodes with the transfer length method (TLM) patterns were formed on ZnO surface using a photolithography and liftoff deposition process. The electrode patterns were designed to be 10μm wide and 100μm long with

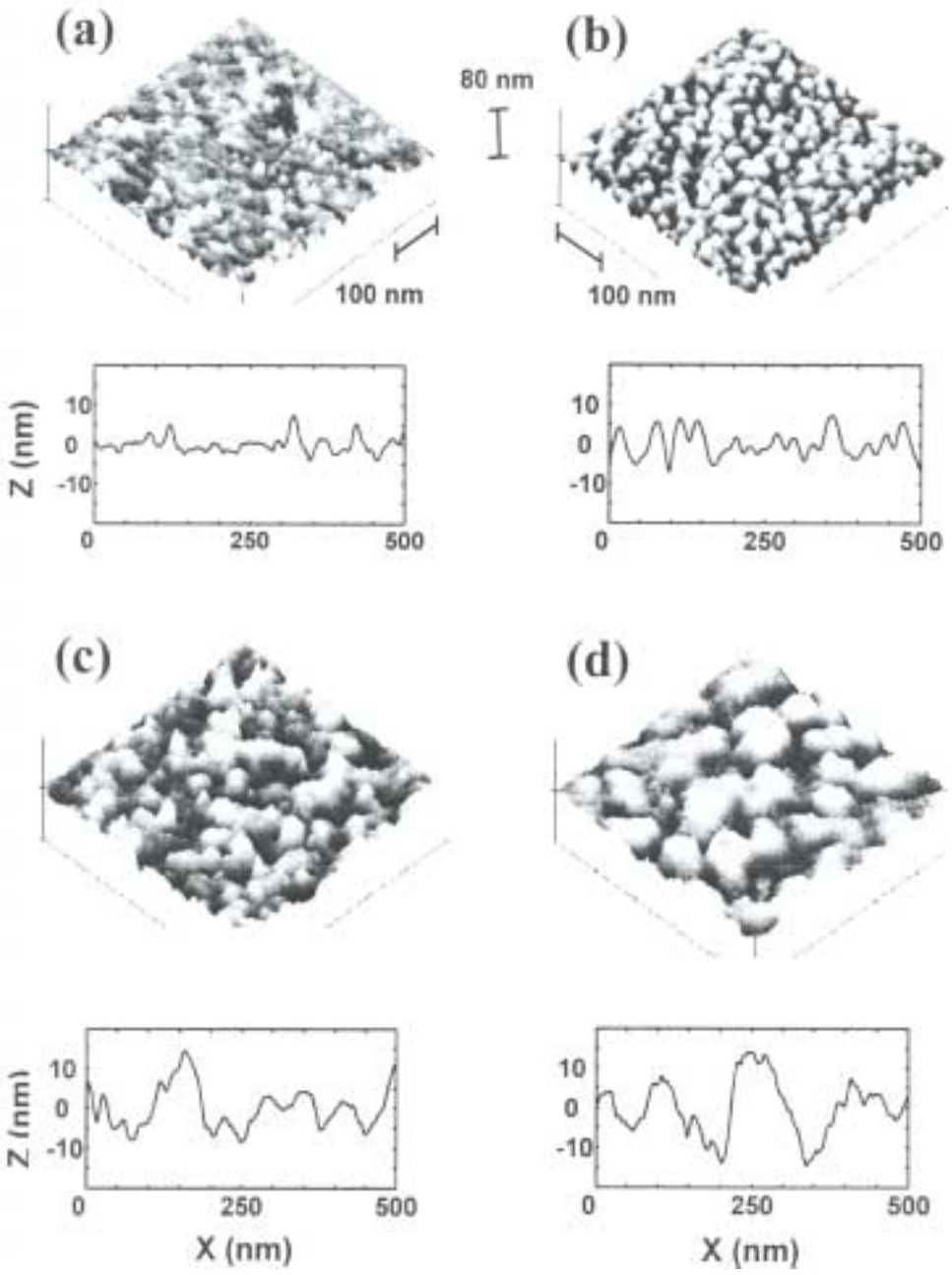

Figure 2-20 (a), (b), (c) and (d): AFM images and sample section profiles at ZnO thickness of 2, 5, 10, and 20 nm, respectively.

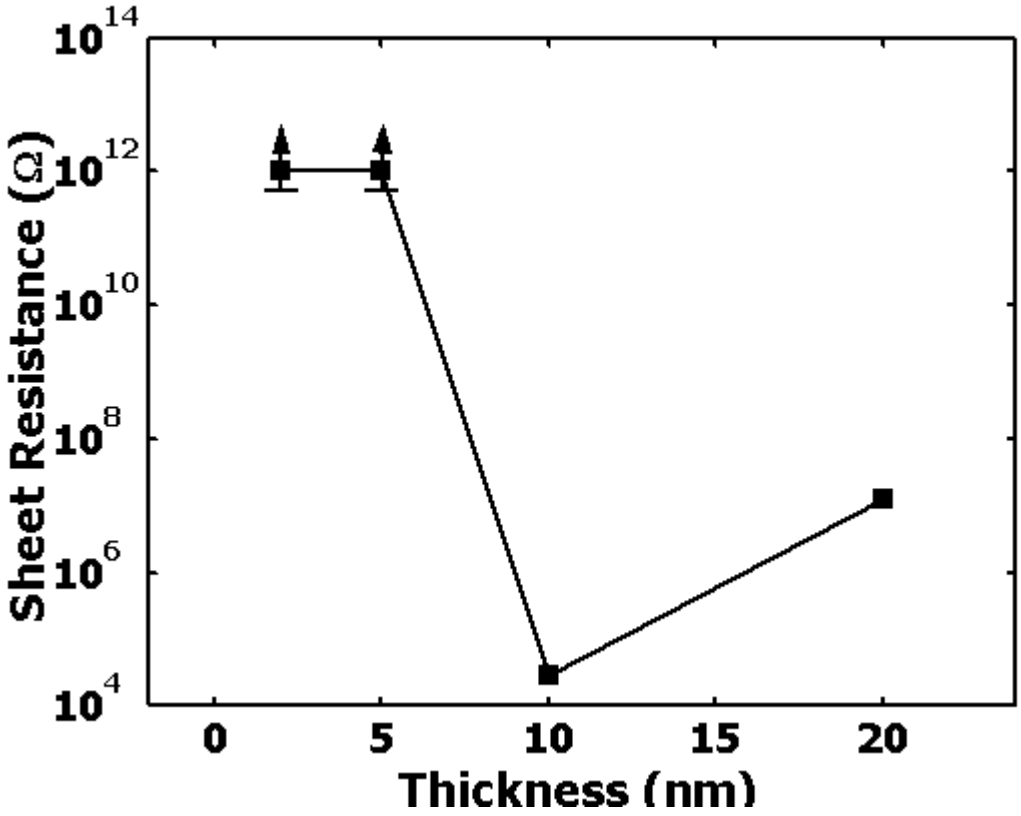

Figure 2-21 ZnO sheet resistance measured at 300 K and plotted as a function of nominal film thickness.

10-50μm spacing between electrodes. (Thus the area of the inter-electrode spacing ranges from 1,000 to 5,000μm^2.) Figure 2-21 shows the sheet resistance measurement result obtained with samples discussed above. ZnO samples with thickness less than 10nm show extremely high sheet-resistance (greater than 10^{12} Ω), virtually the same level as the insulating sapphire surface. This indicated that ZnO islands are electrically discontinous.[44] At 10 nm thickness, the sheet resistance dropped more than seven orders of magnitude to 10^4 Ω level. This corresponds to 0.01Ω•cm level of resistivity when a uniform film thickness is assumed with ZnO. The dramatic change in sheet resistance is consistent with the AFM analysis discussed above, which indicates that ZnO become physically connected at around 10 nm thickness as the islands merged together.

2.4 Conclusions

We have investigated the early-stage growth mode of ZnO on sapphire. The evolution of structural, morphological, and electrical properties was characterized with 2 to 20-nm-thick ZnO films grown at 700 ^oC with radio-frequency magnetron sputtering. X-ray diffraction results show that ZnO initially grows highly strained and epitaxial to substrate with negligible degree of mosaicity for up to ~5 nm thickness, despite the occurrence of partial strain-relaxation which indicates an incommensurate growth involving misfit dislocations. Then the mosaicity (out-of-plane tilt) develops as film thickness increases to around 10 nm. Both the atomic force microscopy (AFM) and resistivity measurement results suggest that ZnO grows as mostly discontinuous (electrically and physically) three-dimensional (3D) nano-islands at 2 to 5 nm thickness, and then the islands coalesce/merge and become connected, fully covering the substrate surface at 5 to 10 nm.

The Volmer-Weber 3D growth mode is believed to be favored by the large lattice–mismatch and the large surface energy of ZnO,[45] as well as the high growth temperature used in this work. Given the fact that these factors play a critical role in determining the growth mode, it would be interesting to investigate the growth behavior of ZnO on other substrates that show better lattice-match and lower interface energy than sapphire, and to explore the feasibility of growing nanometer-sized coherent islands.[46, 47]

3.0 ELECTRICAL CHARACTERISTICS OF ZNO THIN FILMS

3.1 Backgrounds

Most electrical properties of semiconductors are characterized by carrier concentration and mobility, The resistivity is an example and is determined by a production of the two. The high resistivity film is desirable for some application, such as photodetection, which requires low dark current. For the device to be connected to the outside with no adverse change to its current-voltage characteristics and no additional voltage drop, the low-resistance ohmic contacts are also necessary. We studied the electrical properties and the metal contact characteristics of ZnO films by TLM (transfer length method) method.

3.1.1 Metal Contacts on ZnO

An ideal contact is one where, when combined with the semiconductor, there is no barrier to the carrier flow in either positive or negative directions. This can occur when the work function of semiconductor is smaller than or equal to that of the metal work function. As the work function of semiconductor varies with doping, it is usually not easy to find the right combination.

Fortunately, this is not the case for ZnO. It is easy to fabricate ohmic contact on ZnO. Most metals form ohmic contacts on ZnO. On the contrary, it is very difficult to form Schottky contacts on ZnO. Only few metals were reported to form Schottky contacts on ZnO, such as gold, palladium, silver.[48, 49, 50] It is well known that chemical reactions between the metal and semiconductor, and diffusion of the metal into the semiconductor influence the formation of Schottky contacts. These effects are more pronounced in II-VI compound semiconductors compared to III-V semiconductors. In the case of ZnO, metals such as Al, which reacts strongly with chalcogenides (O in ZnO), are expected to produce the most dissociated cations (Zn in ZnO), thus lead to low n-type barrier height.[50] Other factors include the metal induced surface states[51] and the chemisorption of ZnO surface, which results in Fermi level pinning and relatively low Schottky barrier. When the Fermi level is pinned, the metal work function has little effect on Schottky barrier.

The ohmic contact is characterized by the specific contact resistance. For ohmic contact the ratio of the potential drop across the contact versus the current flowing through the contact is linear with a constant R_c. The production of R_c and the area of the contact is called the specific contact resistance expressed as

$$\rho_c = [\frac{\partial J}{\partial V}]^{-1}_{V=0} \ (\Omega \cdot \mathrm{cm}^2), \qquad (3\text{-}1)$$

where J is the current density through the contact, V is the voltage cross the contact. The specific contact resistance is determined by the barrier height and the doping concentration of the semiconductor.[52]

3.1.2 Transfer Length Method

The most widely used method for determining the specific contact resistance is the method of transfer length (TLM).[53] In this approach, a linear array of contacts is fabricated with various spaces between them. The pattern used and the resistance versus the gap space l (l_1, l_2, …) are depicted in Figure 3-1 (a). The total resistance is given by

$$R_T = 2R_C + l * \frac{\rho_s}{Z}, \qquad (3\text{-}2)$$

where R_c is the contact resistance, l is the distance, Z in the width, ρ_s is the sheet resistance of semiconductor.

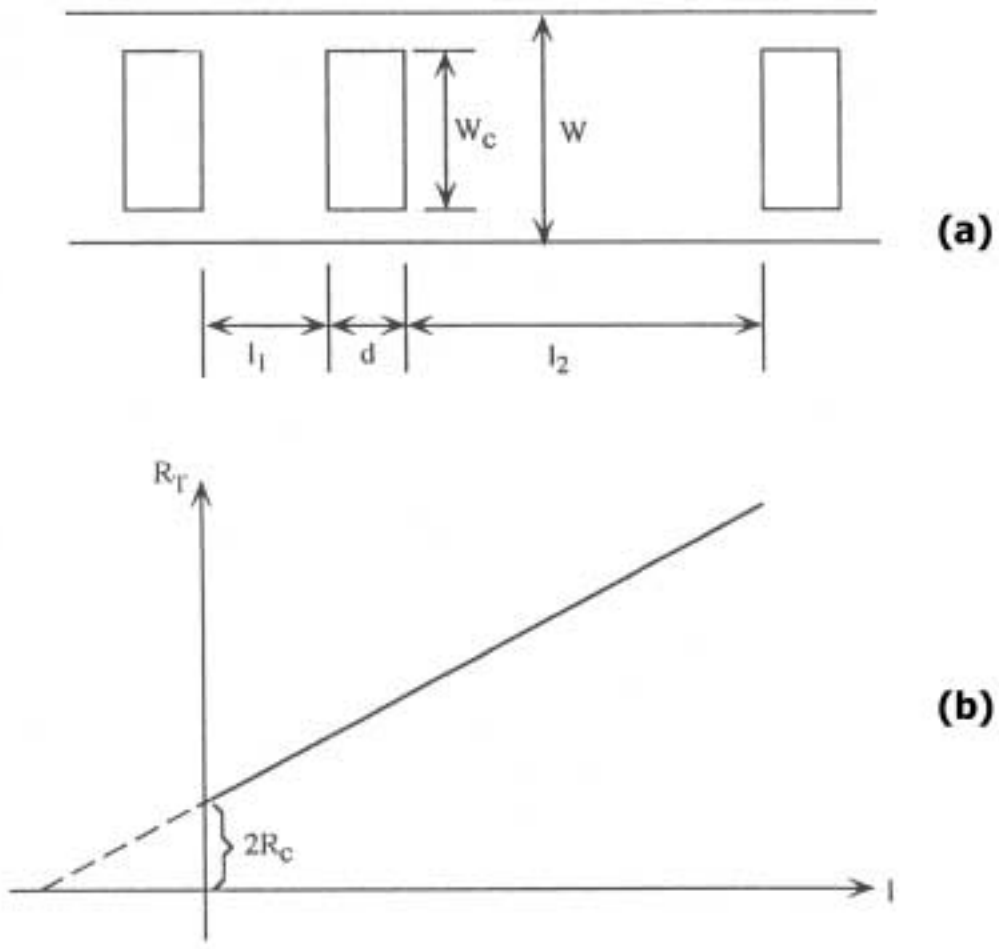

Figure 3.1 (a) Schematic pattern of TLM; (b) the total contact resistance versus the gap distance.

The total resistance is measured for various contact spaces l and plotting R_T as function of l as illustrated in Figure 3-1(b). Three parameters can be extracted from such a plot. The slope $\Delta(R_T)/\Delta(d) = \rho_s/Z$ leads to the sheet resistance, with the contact width Z independently measured. The intercept at $l = 0$ is $R_T = 2R_C$, giving the contact resistance. The intercept at $R_T = 0$ gives $l = 2L_T$, which in turn can be used to calculate the specific contact resistance with ρ_s known from the slope of the plot. The transfer length method gives a complete characterization of the contact by providing the sheet resistance, the contact resistance, and the specific contact resistance.

The contact resistance is related to the transfer length

$$R_C = \frac{\rho_s L_T}{Z} \qquad (3\text{-}3)$$

where ρ_s and L_T represent the sheet resistance in the contact region and the transfer length. Assuming that the sheet resistance under the contact is not modified, the transfer length can be determined and utilized to calculate the specific contact resistance through

$$\rho_C = R_C Z L_T . \qquad (3\text{-}4)$$

3.1.3 Resistivity of Semiconductor

The resistivity of a semiconductor ρ is defined by

$$\rho = \frac{1}{q(n\mu_n + p\mu_p)}, \qquad (3\text{-}5)$$

where n and p are the free electron and hole concentrations, and μ_n and μ_p are the electron and hole mobility, respectively. For external semiconductors in which the majority carrier concentration is much higher than minority carrier concentration, it is generally sufficient to know the majority concentration and the majority carrier mobility, as the case of unintentionally

doped ZnO, which is always n-type. In order to determine the resistivity, carrier concentration and mobility must be known. The carrier concentration may also be extracted from the measured resistivity.

For thin film semiconductor, it is often characterized by its sheet resistance ρ_s expressed in unite of ohms per square. The sheet resistance is given by

$$\rho_s = \frac{\rho}{t}, \qquad (3\text{-}6)$$

where ρ is the resistivity of semiconductor, and t is the thickness of the film. We can obtain the resistivity from the sheet resistance of thin film, which can be derived by TLM measurement.

3.1.4 Chemisorption Effects on the Thin Film Conductivity

The influence of chemisorption on the electrical conductivity of thin film semiconductor, especially compound metal oxide semiconductors with wide bandgap (> 2.0 eV), is critical to the electrical properties and attracts numerous experimental and theoretical studies. The microscopic understanding of charge transfer processes at the phase boundary is of importance in order to support a systematic development of reversible and selective thin film gas sensors, and wide bandgap semiconductor thin film photodetectors.

3.1.4.1 Difference Between Physical and Chemical Adsorption. Two types of adsorption can be distinguished, i.e. physical adsorption (physisorption) and chemical absorption (chemisorption). The difference between physisorption and chemisorption lies in the difference in the forces that retain the adsorbed molecules on the surface of the solid. For physisorption, the force between a solid and a foreign molecule, which produces absorption, is of electrostatic origin, such as Van der Waal's forces or forces of electrostatic polarization or image forces. For chemisorption, the forces responsible for the adsorption are of chemical nature. The adsorption constitutes a chemical combination of molecule with the solid. The forces making up the bond are convalent forces (overlapping between the adsorbate- and adsorbent-wavefunctions), but ionic interaction may be involved to a certain extent.

3.1.4.2 The Volkenstein Isotherm. Assuming that electronic equilibrium established on the surface and the adsorption, and equilibrium prevailed between the surface and the gaseous phase, in the case of nonactivated and non-dissociative adsorption, the conditions for adsorption equilibrium has the form[54]

$$\alpha p(N^* - N) = \nu^0 N^0 \exp(-\frac{Q^0}{kT}) + \nu^- N^- \exp(-\frac{Q^-}{kT}), \qquad (3\text{-}7)$$

where p is the pressure, $\alpha = s_0 A\sqrt{2\pi MkT}$ is the usual kinetic coefficient of the Langmuir iostherm, ν^0, ν^- are typical phonon frequencies of order $10^{13}s^{-1}$, N^* is the surface concentration of the adsorption centers, i.e., the maximum number of particles that a unit area of the surface can adsorb, the total number of chemisorbed species $N = N^0 + N^-$, and $Q^0 = E_a(\infty) - E_a$, $Q^- = E_c + E_a(\infty) - E_a^-$ are adsorption heats of the weak and strong chemisorbed state, respectively.

The total coverage θ is ratio of the total number of chemisorbed species and the number of the chemisorption sites, and

$$\theta = \frac{N}{N^*} = \frac{N^0}{N^*} + \frac{N^-}{N^*} = \theta^0 + \theta^- = f^0\theta + f^-\theta, \qquad (3\text{-}8)$$

where f^0 and f^- are the occupation probabilities of the weak and strong chemisorbed state. With the help of the grand partition function of chemisorption site, [55] they can be calculated,

$$f^0 = \frac{1}{\frac{1}{2}\exp(\frac{E_f - E_s}{kT}) + 1}, \qquad \text{(3-8a)}$$

$$f^- = \frac{1}{2\exp(\frac{E_s - E_f}{kT}) + 1}, \qquad \text{(3-8b),}$$

where $E_s = E_a^- - E_a^0$. Using equation 3-7, one obtains the Volkenstein isotherm

$$\theta(p) = \frac{\beta p}{\beta p + 1} \qquad \text{(3-9a)}$$

with

$$\beta = b\{f^0[1 + \frac{\nu^-}{2\nu^0}\exp(\frac{E_f - E_c}{kT})]\}^{-1}. \qquad \text{(3-9b)}$$

The coefficient *b* of physisorption in the Langmuir isotherm is only a function of temperature, but the coefficient β in chemisorption depends on the bulk Fermi level and surface state energy E_s. That means that in chemical adsorption the adsorptivity of the surface depends on not only the external parameters *p* and *T*, but also on the electronic state of the adsorptive system as a whole, which is determined by the location of the Fermi level.

3.1.4.3 Chemisorption Effect on the Thin Film Conductivity. For simplicity, there are several assumptions for the consideration, (1) acceptor-like chemisorption on n-type non-degenerate wide band gap semiconductor (Figure 3-2); (2) oxygen vacancies are the main donors in the film; (3) thin film semiconductor is ideally isolated from the substrate, no electron transfer between the thin film and substrate; (4) surface states are compensated.

The general expression of the thin film conductivity according to space charge region (SCR) theory of chemisorption is given by

$$\sigma(p) = e\mu_n^{SCR} < n(z, p) >, \qquad (3\text{-}10)$$

where μ_n^{SCR} is the electron mobility in the SCR and the average value of free conduction band electron is

$$< n(z, p) >= \frac{1}{D}\int_0^D dz n^0 \exp(-\frac{\psi(z, p)}{kT}), \qquad (3\text{-}11)$$

where *D* is the thickness of the film.

For a planar geometry ($x = 0$: surface, $x > 0$: bulk) the potential $\psi(x, p)$ is determined by the one dimensional Poisson equation with the charge density

$$\rho(x) = Q_s(E_f, p)\delta(x) + en_d - en(x) + ep(x), \qquad (3\text{-}12)$$

where n_d is the concentration of oxygen vacancies, $\delta(x)$ is the Dirac delta function and the chemisorbed surface charge density is given by

$$Q_s(E_f, p) = -e\theta^-(E_f, p)N_{chem} / A. \qquad (3\text{-}13)$$

In equation 3-12, we have assumed that all oxygen vacancies are singly ionized, and neglected the second ionization.

The Poisson equation can be written as

$$\frac{d^2\psi}{dx^2} = -\frac{q}{\varepsilon}[(p_0(e^{-\beta\psi} - 1) - n_0(e^{\beta\psi} - 1)], \qquad (3\text{-}14)$$

where $\beta = q/kT$, n_0, p_0 are carrier concentration in bulk film. With respect to the two appropriate boundary conditions (i) global charge neutrality (assuming no charge at the interface between film and the substrate)

$$\left.\frac{d\psi}{dx}\right|_{x=D} = 0, \qquad \text{(3-15a)}$$

and (ii) Gauss law

$$\left.\frac{d\psi}{dx}\right|_{t=0} = \frac{Q_s(E_f, p)}{\varepsilon}; \qquad \text{(3-15b)}$$

we integrate once and obtain equation 3-16

$$\frac{d\psi}{dx} = -\frac{\sqrt{2}}{\beta L_D}[F(\psi) - F(\psi_D)]^{1/2}, \qquad \text{(3-16)}$$

where $F(\psi) = \frac{p_0}{n_0}(e^{-\beta\psi} + \beta\psi) + (e^{\beta\psi} - \beta\psi)$, $L_D = \sqrt{\frac{\varepsilon}{qn_0\beta}}$, $\psi_D = \psi(x = D)$. It is noted that the pressure dependence of the potential is involved by the boundary conditions, where the surface charge density is determined by the coverage of the charged, strong chemisorbed species $\theta^- = f^-\theta$. Since the occupation probabilities are dependent on the difference $E_f - (E_s^0 + \psi(z = 0, p))$ and hence on the solution, therefore one has to solve the problem selfconsistently.

3.1.4.4 Numerical Computation of Wolkenstein's Isotherm on the Chemisorption Behavior of Oxygen on n-type ZnO. For numerical calculation on ZnO epilayers, the following parameters values are used: E_g = 3.3 eV, $m_{eff} = 0.25m_0$, $E_s(O_2)$ = -0.8eV, Q^0 = 0.1 eV, the sticking coefficient $s_0 = 10^{-15}/cm^2$ and $N^* = 10^{15}/cm^2$. The calculations were carried out for three different doping levels ($N_D = 10^{14}$, 10^{16}, $10^{18}/cm^3$ at film thickness 0.5 μm, and for four different film thickness 0.2, 0.1, 0.05, 0.02 μm, at $N_D = 10^{16}/cm^3$, at temperature $T = 300K$.

The equilibrium surface potential barrier (ψ) was calculated as a function of the oxygen pressure (p) for various doping levels. The results are shown in Figure 3-3. The surface potential is proportional to $\log_{10}p$ for a wide range of pressure. Figure 3-3 also demonstrates that the slope is independent of the doping level. There is a relationship, $d\psi / log_{10}p = 2.3kT$, which can be derived from Wolkenstein's isotherm under certain approximations.[56] In Figure 3-3, ZnO film thickness is 0.5 μm, which is not depleted under considering surface potential. When the film thickness is reduced, the film will be totally depleted by the chemisorbed oxygen molecules at certain oxygen pressure value (as shown in Figure 3-4). Before totally depleted, the surface potential is independent of the film thickness at an oxygen pressure. After the film is totally depleted, the surface potential is dependent on the film thickness, which is higher for thinner film, at an oxygen pressure. It can be understood as follows. At an oxygen pressure, the chemisorbed oxygen molecules generated a certain amount of charge at the surface, which must be neutralized by the charge in the film. For thin film, a higher surface potential is needed to produce this amount of charge than thick film. At the same time, in thin film regime (here 50 nm, 20 nm), the degree of coverage of chemisorbed oxygen species will also depend on the film thickness.

Substituting the results obtained for ψ as a function of p enables us to calculate the degree of coverage of oxygen chemisorbates (θ) as a function of oxygen pressure. Moreover, the degree of coverage of charged adions $\theta^- \equiv N^- / N^* = f_A^- \theta$ and neutral adatoms $\theta^0 \equiv N^0 / N^* = (1 - f_A^-)\theta$ can be calculated separately. The results are shown in Figure 3-5, which shows the dependence on the doping level and Figure 3-6, which shows the thickness dependence (with $N_D = 10^{16}/cm^3$), At low oxygen pressures ($p < 10^2$ Pa) $\theta \approx \theta^- >> \theta^0$, i.e.,

nearly all oxygen chemisorbates are in charged state. At higher pressure θ^- approaches saturation while θ^0 continues to grow monotonically. Eventually, at some point θ^0 becomes larger than θ^-. This complies with the expected behavior for such a depletive chemisorptin process. At low gas pressures the surface is relatively clean and the band bending is small. In this case, the adsorption heat of the charged form of chemisorption, $q^- = q^0 + (E_C^b - E_A^S)$ is greater than that of the neutral form, q^0. Thus, the charged state is energetically more favorable than the neutral state and most species chemisorb as charged adions. As the gas pressure increases, more and more adions chemisorb and the surface charge density increases in magnitude. Consequently, surface potential increases and the adsorption heat decreases, i.e., the charged form of chemisorption becomes less favorable with respect to the neutral form, whose heat of adsorption is independent of the degree of coverage. As a result, at some point the neutral form of chemisorption becomes predominant.

Figure 3-5&6 shows that θ^- approaches saturation when *p* increases and that the degree of coverage of charged adions does not exceeds a small fraction of monolayer. The saturation of the charged form of chemisorption results from the pinning of the Fermi level at the semiconductor surface when it becomes aligned with the energy level of the chemisorption-induced surface states.

In Figure 3-6, the degree of coverage is independent on the film thickness when the film is thick (500nm/250nm), as even the θ^- approaches saturation, the width of depletion layer is less than the film thickness, i.e., the film can provide enough charge to neutralize the surface charge due to the oxygen chemisorption. Therefore the chemisorption saturation is determined by the pinning of the Fermi level at the semiconductor surface. For thin films (50nm/20nm), before the Fermi level aligns with the energy level of the chemisorption-induced surface states, the semiconductor films are totally depleted, therefore the degree of coverage depends on the charge, which the film can provide, i.e., $N_D t+p-n$, where *t* is the film thickness, which is dependent on the film thickness. As the film is in depletion region, and ZnO has a bandgap of 3.3 eV at room temperature, the electron and hole concentration is negligible and the total charge is $N_D t$, which is fixed at given film. In Figure 3-6, for thin films (50/20nm), the degree of coverage saturates long before the thick films (500/250nm) saturate, which is determined by the Fermi

level pinning at semiconductor surface, because the thin films is totally depleted long before the Fermi level pinning, whose saturation is determined by the total charge, $N_D t$. It is interesting to note that it is possible to inverse the semiconductor through chemisorption, if the bandgap of the semiconductor is not too wide.

The degree of coverage of adions depends on the doping level at all pressures as shown in Figure 3-5. This arises from the fact that the chemisorption of adions involves free electrons and therefore the higher the doping level the more free electrons are available for this process and consequently θ^- increases. As opposed to the charged form of chemisorption, the neutral form involves no electronic charge transfer between the semiconductor and the adsorbates, and therefore θ^0 is independent of the doping level, as shown Figure 3-5. Thus, it could be expected that Langmuir's model should give a satisfying description of the chemisorption behavior of the neutral adsorbates, regardless to the existence of charged species on the surface. It is found that Wolkenstein's isotherm for neutral form of chemisorption actually reduces to the well-known Langmuir isotherm.[56]

In Figure 3-7, the oxygen pressure dependence of the average electron density is shown for different doping levels, and different film thickness (Figure 3-8), the power-law behavior, $< n > \propto p_{O_2}^{-m}$, can be seen in wide pressure range, 10^{-10}atm ~ 1atm, and the power m decreases with the increasing the doping levels and film thickness. Under certain oxygen pressure, when the doping level is high, the width of depletion is narrow, and insignificant comparing the total film thickness, the modulation of the film's conductance is not significant. The same situation for the thick film, the width of depletion region is only a small ratio to the film thickness and has less effect on the film conductance at certain doping level as shows in Figure 3-8.

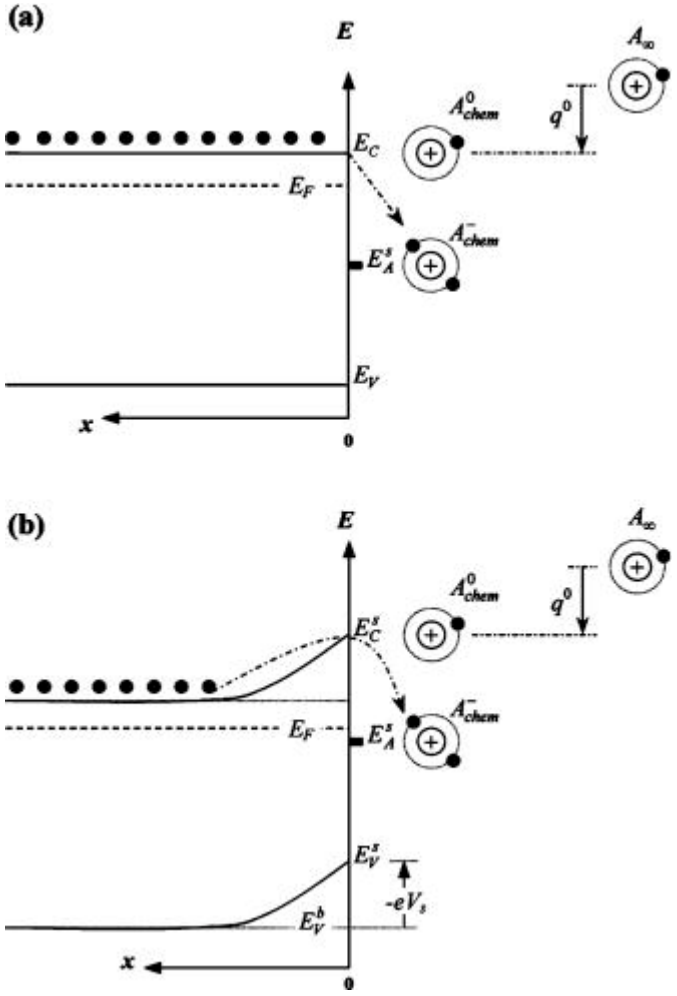

Figure 3.2 Energy-band diagram for acceptor-like chemisorption on an n-type semiconductor: (a) At the beginning of chemisorption; (b) at thermal equilibrium. A_∞, A^0_{chem} and A^-_{chem} designate a free atom in the gas phase, a neutral adatom, and a negatively charged adion, respectively.

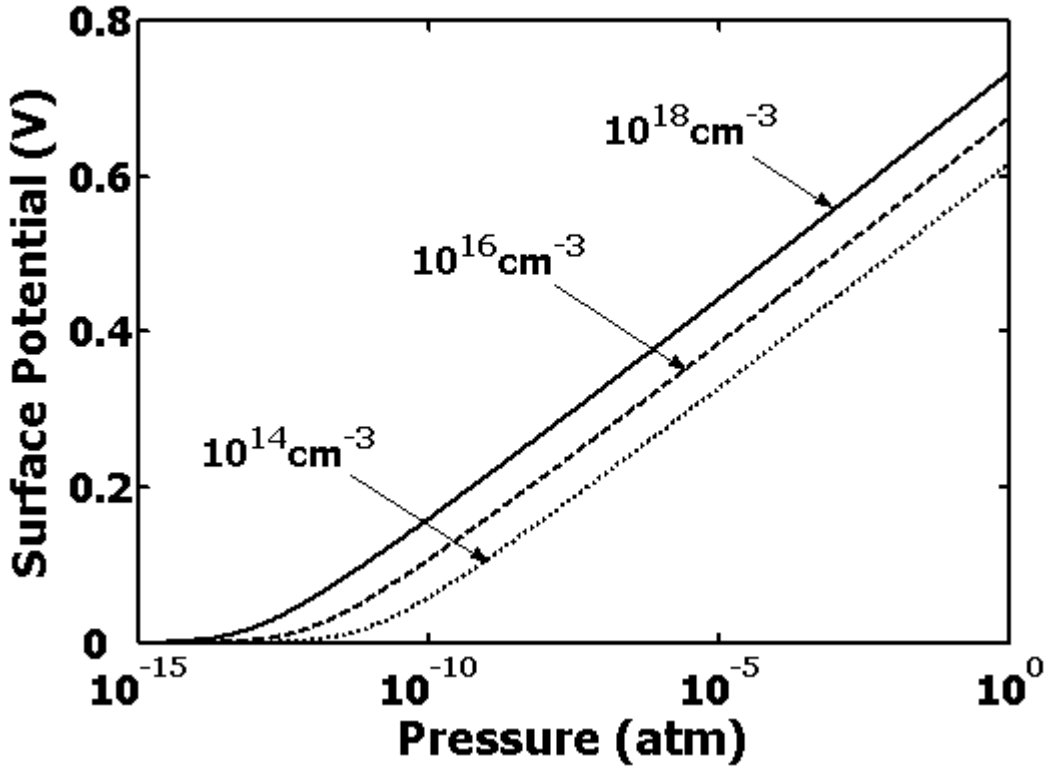

Figure 3.3 The equilibrium surface potential as a function of the oxygen pressure for different doping level at 300 K and film thickness 0.5 μm.

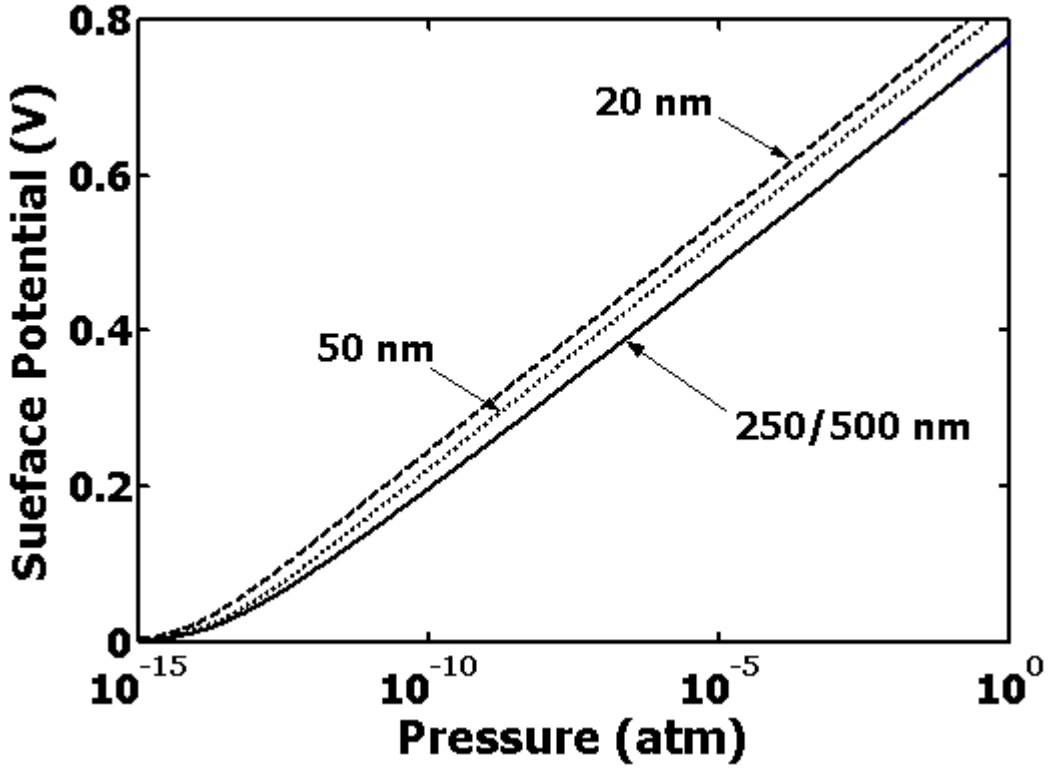

Figure 3.4 The equilibrium surface potential as a function of the oxygen pressure for different film thickness at 300 K and doping level $10^{16}cm^{-3}$.

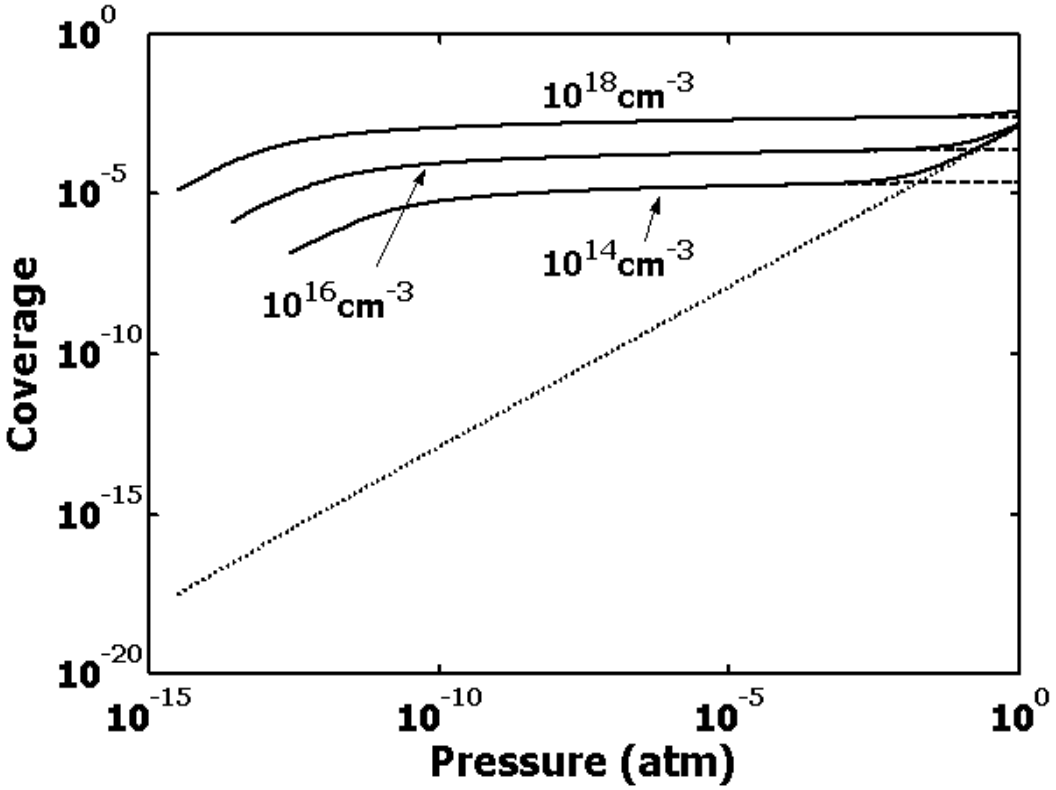

Figure 3.5 The degree of coverage of chemisorbed oxygen species as a function of oxygen pressure for different doping levels at 300K and film thickness 0.5 μm.

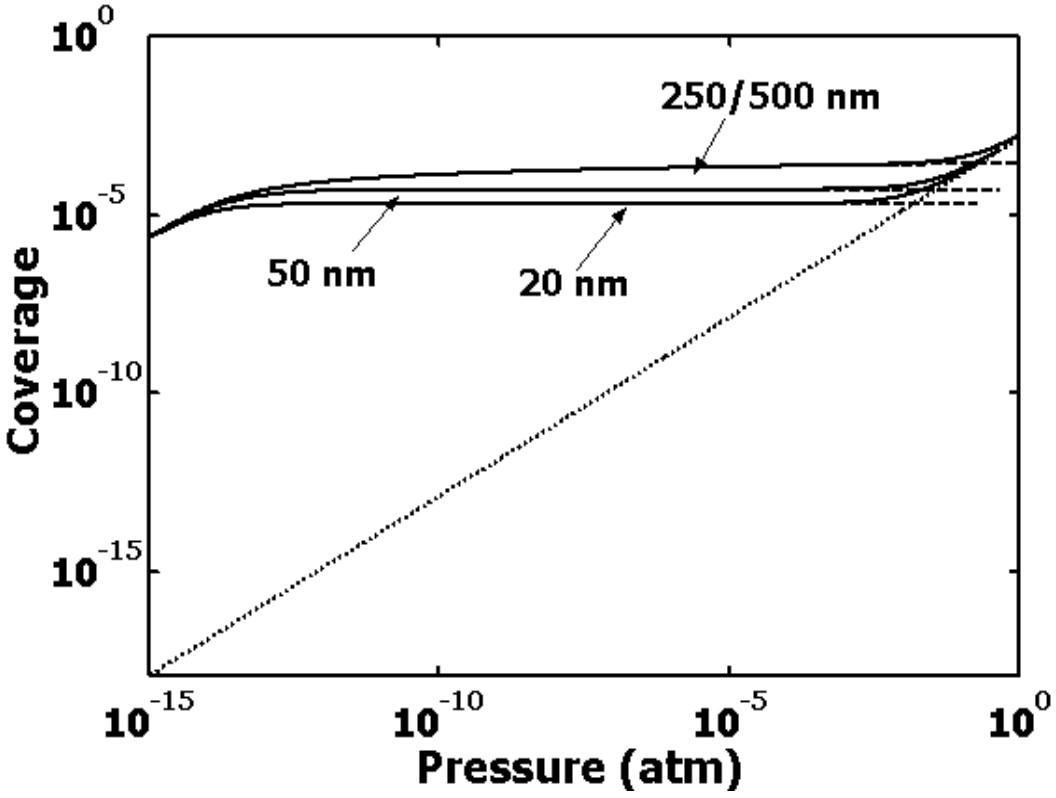

Figure 3.6 The degree of coverage of chemisorbed oxygen species as a function of oxygen pressure for different film thickness at 300 K and doping level $10^{16}cm^{-3}$.

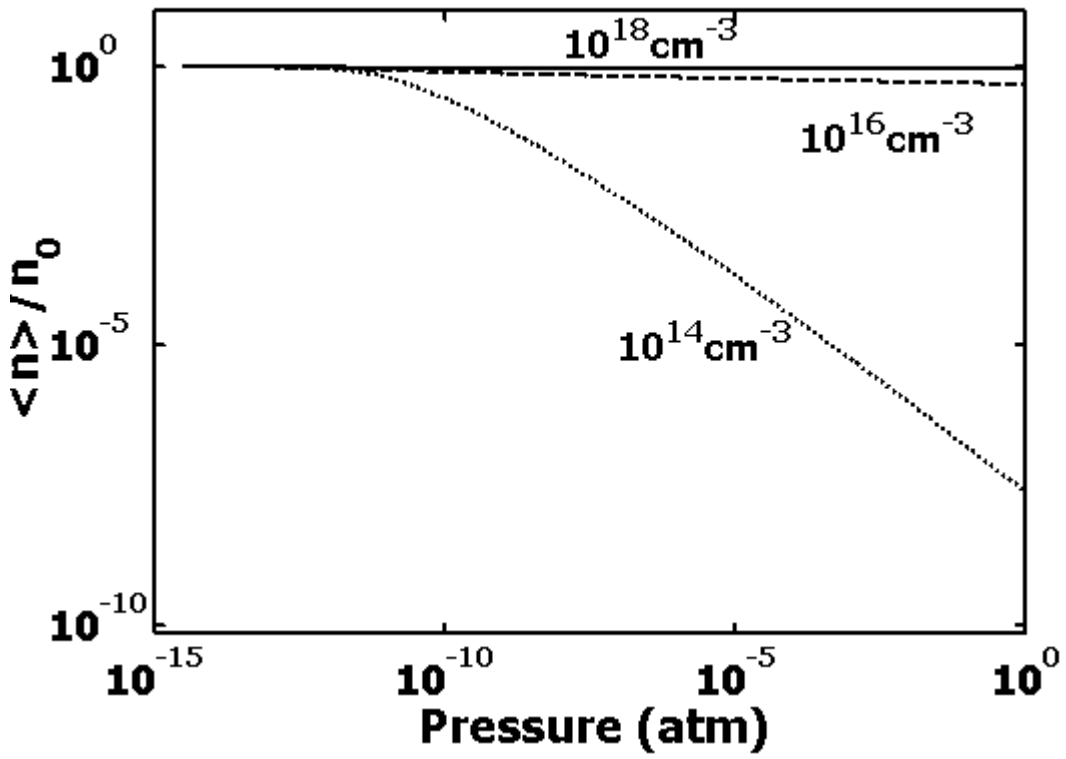

Figure 3.7 The normalized, average electron density as a function of oxygen pressure for different doping levels at 300K and film thickness 0.5 μm.

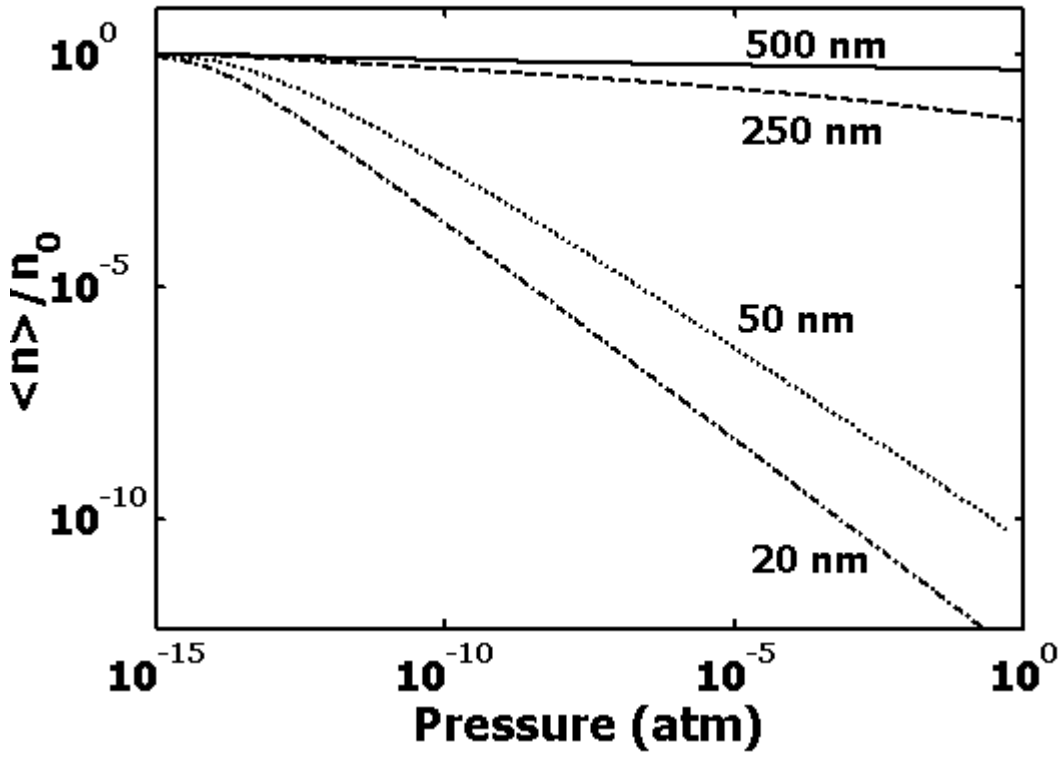

Figure 3.8 The normalized, average electron density as a function of oxygen pressure for different film thickness at 300 K and doping level $10^{16}cm^{-3}$.

3.2 Experimental Results and Discussion

Different thickness ZnO films were deposited on sapphire substrates by rf sputtering. X-ray diffraction and pole Figure measurements indicate that these films are epilayers, i.e., single crystal-like. TLM method was applied to characterize the electrical properties of these films. The pattern is shown in Figure 3-1(a). The distances between the electrodes are 6.0 μm, 8.0 μm, 16.0 μm, 24.0 μm, 32.0 μm, respectively. The width of the electrode is 60.0 μm, and the length 500.0μm. Aluminum was deposited by thermal evaporation to form the electrodes. Without annealing, the contacts show ohmic contact characteristics.

3.2.1 Electrical Properties of ZnO Epilayers

Figure 3-9 shows the specific contact resistance for ZnO films with different thickness. (Samples were deposited in Ar/O_2 ambient or pure Ar ambient). The specific contact resistance of ZnO epilayers deposited in Ar/O_2 ambient is lower than that of epilayers deposited in Ar ambient. The specific contact resistance decreases with decrease of the film thickness. The specific contact resistance is determined by the Schottky barrier height and the dopant concentration of the film. Assuming that the barrier height of Al on ZnO is constant, the dopant concentration is the only factor that determines the specific contact resistance. As $\rho_c \propto 1/\sqrt{N_D}$, it indicates that the thinner film has higher carrier concentration. This result is consistent with resistivity results of the film derived from this measurement (Figure 3-10). The resistivity of ZnO film monotonically decreases with the decease of the film thickness. This result seems to contradict chemisorption theory, in which the free electron density deceases as the decease of the film thickness, i.e., the resistivity increases, considering that it is impossible for the electron mobility increase with the decrease of the film thickness due to the surface scattering. This suggests that there be other factors that affect the resistivity of the film in thin regime, such as dislocations and other defects. ZnO epilayer on sapphire is similar to that of GaN epilayer on sapphire. The larger lattice mismatch between epilayer and substrate may cause a highly dislocated layer near the interface. A high conductive layer (0.3 μm ~ 0.5 μm) at the interface between GaN and sapphire has been observed.[57] The conduction in the interface layer arises from a donor impurity band due to the incorporation of high levels of impurity and/or native

defects during the initial stage of growth. Two-layer model, including the interface layer and the rest of layer, was proposed and succeeded explaining the electrical properties.[58] Two-layer model seems to be unsuitable for explaining our observations. In our case, the resistivity of ZnO film increases almost four orders when the thickness decreases one order. A highly conductive thin layer indeed forms at the very early stage of the growth. As the growth proceeds, however, this high conductive layer gradually disappears or the difference is not very obvious between this initial layer and the following layer. It is probably due to the indiffusion of the oxygen radicals during the deposition, which results in a relatively uniform resistivity epilayer. At the deposition environment temperature, the vapor pressure of ZnO is about 1.5×10^{-7} Torr,[59] which is smaller than the deposition ambient pressure, 1×10^{-4} Torr. There is high probability for oxygen radical diffusion into ZnO film during the deposition process.

3.2.2 Postdeposition Annealing Dependence of the Film Resistivity

Figure 3-11 is the comparison for the resistivity of ZnO films as-deposited and after annealed. Although the annealing was performed in an O_2 ambient at 1000°C, the resistivity reduced dramatically. It indicates that the O_2 pressure is not high enough to suppress the outdiffusion of oxygen component in ZnO films. The deficiency of oxygen results in the enhancement of the conductivity.[60]

3.2.3 Deposition Gas Dependence of the Film Resistivity

Figure 3-10 shows a comparison of the resistivity of ZnO films deposited in two different ambient, pure Ar, and Ar/O_2 (95/5) mixture. The films deposited in Ar/O_2 mixture have higher resistivity than those of in pure Ar in all measured thickness regime. The Kroger-Vink-diagram shows that increasing the oxygen pressure will reduce the oxygen deficiency of ZnO film and the films become more stoichiometric.[61] This reduces the electron concentration and increases the resistivity of the film.

3.2.4 Oxygen Pressure Dependence of the Film Resistivity

The resistivity of a ZnO epilayer (200 nm) was measured in oxygen ambient at different pressure (as shown in Figure 3-12, squares represent the measurement results). Using the oxygen chemisorption model (in Figure 3-12, dashed line), we fitted our measurement data with the following parameter Vo = $9\times10^{15}/cm^3$, and got the relationship $<\sigma> \propto p_{O_2}^{-m}$, m = 0.25.

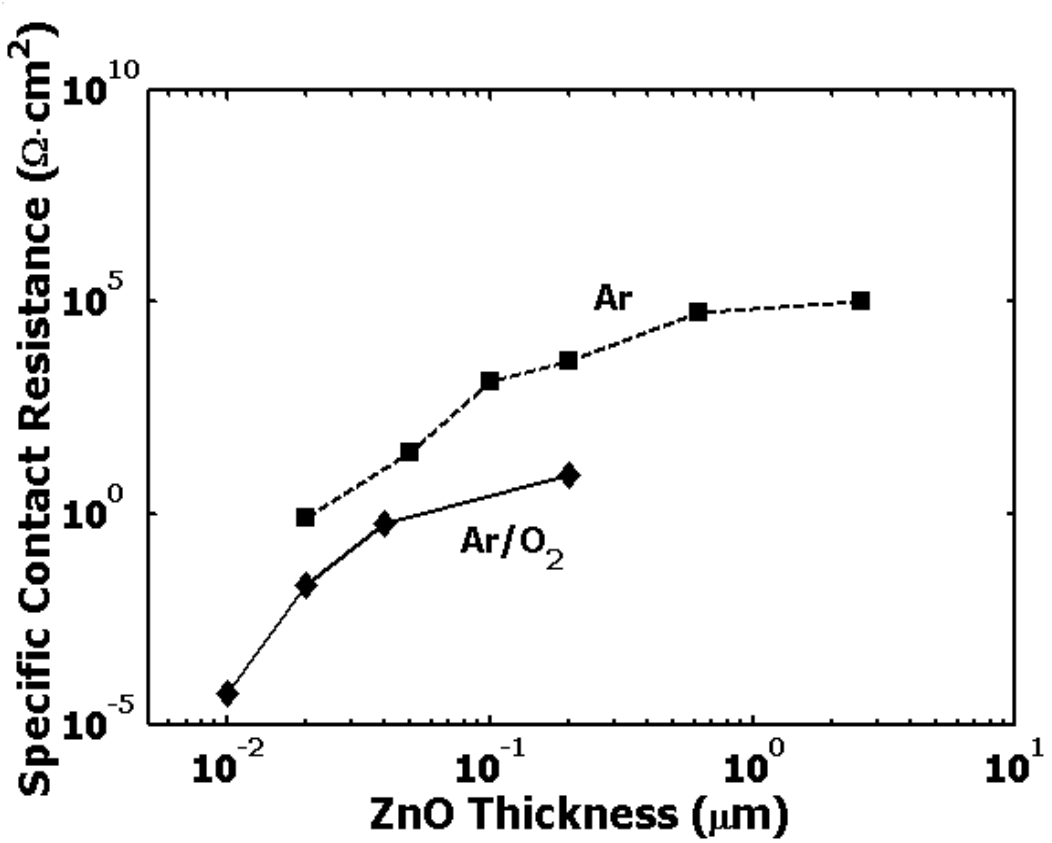

Figure 3.9 Thickness dependence of aluminum specific contact resistance on ZnO epilayers deposited in pure Ar ambient and Ar/O_2 ambient.

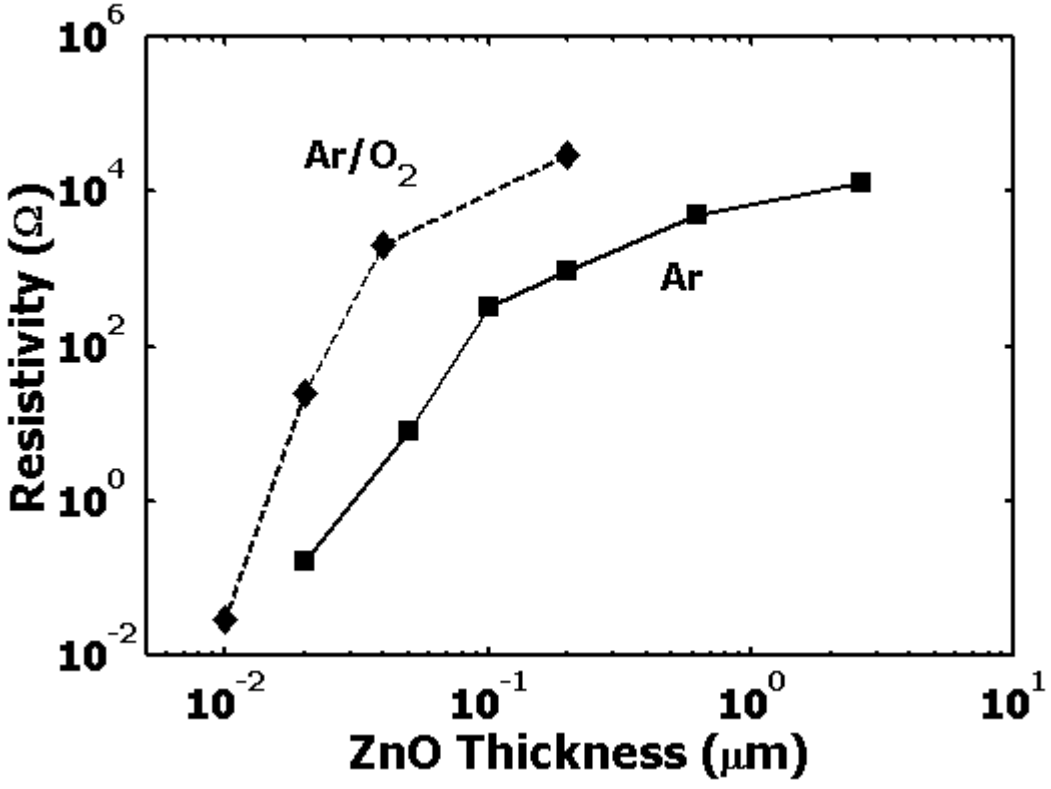

Figure 3.10 Thickness dependence of resistivity of ZnO epilayers deposited in pure Ar ambient and Ar/O_2 ambient.

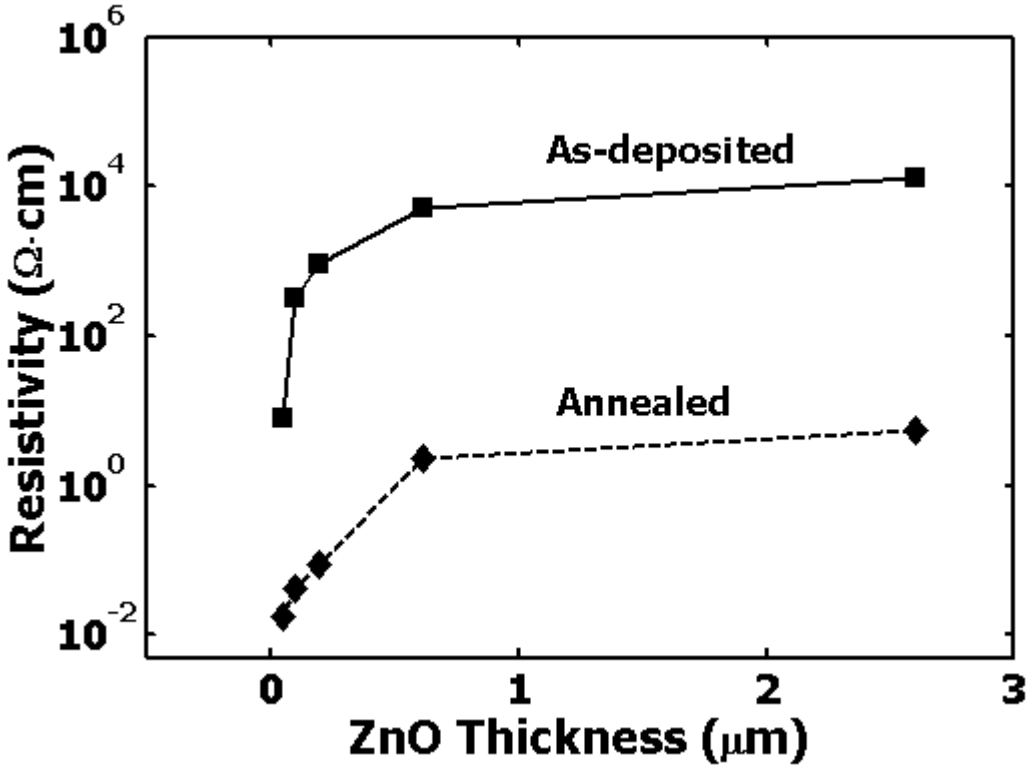

Figure 3.11 Annealing effect on the resistivity of ZnO epilayers deposited in pure Ar ambient.

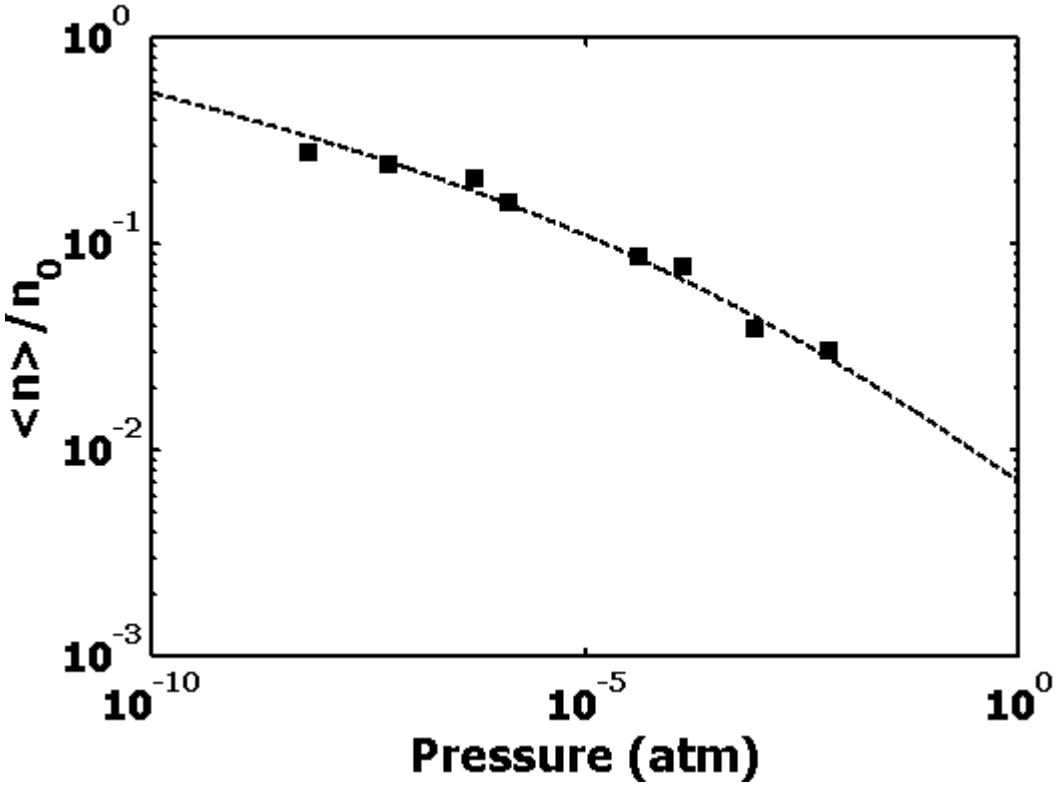

Figure 3.12 The average, normalized electron as a function of oxygen pressure (Squares represent measurement data, and dashed line is fitting curve with $N_D = 9\times10^{15}/\text{cm}^3$).

3.3 Conclusions

We have grown high quality ZnO epilayers on sapphire substrate and studied its electrical properties by TLM. The resistivity of the film decreases with the decrease of the film thickness, which is incompatible with the reported results. The chemisorption model is invalid in our case, so is the two-layer model, which is valid for GaN/sapphire systems. This suggests that initial high conductive layer evolutes into high resistivity during the deposition due to the indiffusion of the oxygen component. The resistivity increases with the increase of the oxygen pressure, which can be interpreted by the oxygen chemisorption on ZnO surface. This shows the oxygen chemisorption is a main factor to affect the electrical properties of the thin ZnO epilayers.

We also investigated the oxygen chemisorption effect on nanometer-scale ZnO films (< 50nm). The degree of coverage is dependent on doping level of the films and the thickness of the films. The higher is the doping level, the larger degree of coverage is. As the thin films can't provide enough charge to neutralize the surface charge resulting from oxygen chemisorption, thinner film has less degree of coverage. These results would extend to other low-dimensional structures of ZnO, such as quantum dots, nano wires and ribbons.

4.0 ZNO-BASED UV PHOTODETECTORS

4.1 Introduction

A photodetector is an optoelectronic device that absorbs optical energy and converts it to electrical energy, which usually manifests as a photocurrent. There are generally three steps involves in the photodetection process: (1) absorption of optical energy and generation of carriers, (2) transportation of the photogenerated carriers across the absorption and/or transit region, with or without gain, and (3) carriers collection and generation of a photocurrent, which flows through external circuitry. The process of detection is sometimes associated with demodulation, when high-frequency optical signal is converted into a time-varying electrical signal and further processed and rectified. Photodetectors are used to detect optical signals ranging over a very wide range of the optical spectrum.

Photodetectors are widely used in optical communication systems. In this application, detectors receive the transmitted optical pulses and convert them into electronic pulses that can be used by telephones, computers, or other terminals at the receiving end. The performance requirements from the detectors are high sensitivity, low noise, wide bandwidth, high reliability, and low cost. Another common application of photodetector is the monitoring of laser transmitters. A large-area detector is placed close to one facet of a transmitting laser source. The photocurrent generated in the detector is used in a circuit to maintain the laser output at a near-constant level in spite of the temperature fluctuation. For communication applications, there is usually a need for high-speed detectors. For several other applications, high gain is necessary. Therefore, bandwidth and gain are fundamental physics trade-offs and the final application decides which photodetector is the most suitable.

The three main types of semiconductor photodetectors are photoconductors, PIN diodes, and avalanche photodiodes. The first and the third types have internal gain. PIN photodiodes have no internal gain but have very large bandwidths. Other specialized photodetectors include phototransistor, the modulated photodiode, and the metal-semiconductor-metal (MSM), etc.

Photodetectors are also classified into intrinsic and extrinsic types. An intrinsic photodetector usually detects light of wavelength close to the bandgap of the semiconductor. Photoexcitation creates electron-hole pairs, which contribute to the photocurrent. An extrinsic photodetector detects light of energy smaller than the bandgap energy. In these devices the transition corresponding to the adsorption of photos involves deep impurity and defects levels within the bandgap. Thus, adsorption of a photo usually raises electron from a deep level to the conduct band, or/and electron from the valence band to the deep level, leaving behind a hole in the valence band. The electron or hole in the respective bands contributes to the photocurrent. There is another type of extrinsic photodetector, which involves transitions between subband energies in a quantum well. Since the energy difference between these subband energies is usually small and of the order of 100 meV, such devices are used for far-infrared detection. There are, however, some drawbacks and limitations regarding the polarization of light that can be absorbed.

4.1.1 Properties of Semiconductor Photodetectors

Certain fundamental rules govern all semiconductor photodetectors. These include quantum efficiency, responsivity, and response time. The following section will examine them from a general point of view.

4.1.1.1 Quantum Efficiency. The quantum efficiency η ($0 \leq \eta \leq 1$) of a photodetector is defined as the probability that a single photo incident on the device generates a photocarrier pair that contributes the detector current. When many photos are incident, as is almost the case, η is the ratio of the flux of generated electron-hole pair that contributes to the detector current to the flux of incident photos. Not all incident photos produce electron-hole pair because not all incident photos are absorbed. Some photos simply fail to be absorbed because of the probabilistic nature of the absorption process. Other may be reflected at the surface of the detector, thereby reducing the quantum efficiency further. Furthermore, some electron-hole pairs produced near the surface of the detector quickly recombine because of abundant of recombination centers there and are therefore unable to contribute the detector current. Finally, if the light is not properly focused

onto the active area of the detector, some photos will be lost. This is not included in the definition of the quantum efficiency, however, because it is associated with the use of the device rather than with its intrinsic properties.

The quantum efficiency can therefore be written as [62]

$$\eta = (1-\Re)\zeta\,(1-\exp(-\alpha d)), \qquad (4\text{-}1)$$

where R is the optical power reflectance at the surface, ζ the fraction of electron-hole pairs that contribute successfully to the detector current , α the absorption coefficient of the material, with unit cm $^{-1}$, and d the detector depth.

Equation 4-1 is a production of three factors:

- The first factor (1 - R) represents the effect of the reflection at the surface of the device. Reflection can be reduced by the use of antireflection coating.
- The second factor ζ is the fraction of electron-hole pairs that successfully avoid recombination to the material surface and contribute to the useful photocurrent. Surface recombination can be reduced by carefully material growth.
- The third factor, $\int_0^d e^{-\alpha x}dx \,/ \int_0^\infty e^{-\alpha x}dx = (1-e^{-\alpha d})$, represents the fraction of the photo flux absorbed in the bulk of the material. The device should have a sufficiently large value of d to maximize this factor.

The quantum efficiency η is a function of wavelength, principally because of the absorption coefficient α depends on wavelength. For photodetector materials of interest, η is large within a spectral window that is determined by the characteristics of the material. For sufficiently large λ_o, η becomes small because absorption cannot occur when $\lambda_O \geq \lambda_g = hc_O / E_g$ (the photo energy is then insufficient to overcome the bandgap). The bandgap wavelength λ_g is the long-wavelength limit of the semiconductor material. E_g is bandgap energy of the semiconductor

materials. For sufficiently small values of $\lambda_{g,}$ η also decreases, because most photos are then absorbed near the surface of the device. The recombination lifetime is quite short near surface, so that the photocarriers recombine before being collected.

4.1.1.2 Responsivity. The responsivity relates the electric current flowing in the device to the incident optical power. If every photo were to generate a single photoelectron, a photo flux Φ (photos per second) would produce an electron flux Φ, corresponding to a short-circuit electric current $i_p = e\Phi$. An optical power $P = h\nu\Phi$ (watts) at frequency ν would then give rise to an electric current $i_p = eP/h\nu$. Since the fraction of photos producing detected photoelectrons is η rather than unity, the electric current is

$$i_p = \eta e\Phi = \frac{\eta eP}{h\nu} = \Re P . \qquad (4\text{-}2)$$

The proportional factor $\Re$, between the electric current and the optical power, is defined as the responsivity of the device. $\Re = i_p / P$ has units of A/W and is given

$$\Re = \frac{\eta e}{h\nu} = \eta \frac{\lambda_O}{1.24}, \qquad (4\text{-}3)$$

where λ_o in μm. $\Re$ increases with λ_o because photoelectric detectors are responsive to the photo flux rather to the optical power. As λ_o increases, a given optical power is carried by more photos, which, in turn, produce more electrons. The region over which $\Re$ increases with λ_o is limited, however, since the wavelength dependence of η comes into play for both long and short wavelengths.

The responsivity can be degraded if the detector is presented with an excessively large optical power. This condition, which is called detector saturation, limits the detector's linear dynamic range, which is the range over which it responds linearly with the incident optical power.

4.1.1.3 Devices with Gains. The formulas presented above are predicted on the assumption that each carrier products a charge *e* in the detector circuit. However, many devices produce a charge *q* in the circuit that differs from *e*. Such devices are said to exhibit gain. The gain *G* is the average number of circuit electrons generated per photocarrier pair. *G* is distinguished from η, which is the probability that an incident photo produces a detectable photocarrier pair. The gain, which is defined as

$$G = \frac{q}{e}, \qquad (4\text{-}4)$$

can be either greater than or less than unity, as will be seen subsequently. Therefore, more general expressions for the photocurrent and responsivity are

$$i_p = \eta q \Phi = G \eta e \Phi = \frac{G \eta e P}{h\nu} \qquad (4\text{-}5)$$

and

$$\Re = \frac{G\eta e}{h\nu} = G\eta \frac{\lambda_O}{1.24} \qquad (4\text{-}6)$$

respectively, where i_p is photocurrent, $\Re$ in A/W, λo in μm.

4.1.1.4 Response Time. In photodetector material, the charge delivered to the external circuit by carrier motion is not provides instantaneously but rather occupies an extended time. It is as if the motion of the charged carriers in the material draws charges slowly from the wire on the device and pushes slowly into the wire at the other side so that each charge passing through the external circuit is spread out in time. This phenomenon is known as transit-time spread. It is an important limiting factor for the speed of operation of all semiconductor photodetectors.

A photo generates an electron-hole pair in a photodetector material, and actually generated charge is *e* not 2*e*. Considering an electron-hole pair generated (by photo absorption, for example) at an arbitrary position in the semiconductor material of width *w* to which a voltage *V*

is applied, as shown in Figure 4-1, we restrict out attention to motion in the *x* direction. A carrier of charge *Q* (a hole of charge $Q = e$ or in electron of charge $Q = -e$) moving with a velocity *v(t)* in the direction creates a current in the external circuit given by

$$i(t) = -\frac{Q}{w} v(t) \ . \qquad (4\text{-}7)$$

This formula is known as Ramo's theorem.[62]

In presence of a uniform charge density ρ, instead of a single point charge *Q*, the total charge is ρAw, where *A* is the cross-sectional area, so that Ramo's theorem is gives $i(t) = -(\rho Aw/w)v(t) = -\rho Av(t)$ from which the current density in the *x* direction (to the right) $J(t) = -i(t)/A = -\rho v(t)$.

In presence of an electric field *E*, a charge in a semiconductor will drift at a mean velocity

$$v = \mu E \ , \qquad (4\text{-}8)$$

where μ is the carrier mobility. Thus, $J = \sigma E$, where is $\sigma = \mu\rho$ the conductivity.

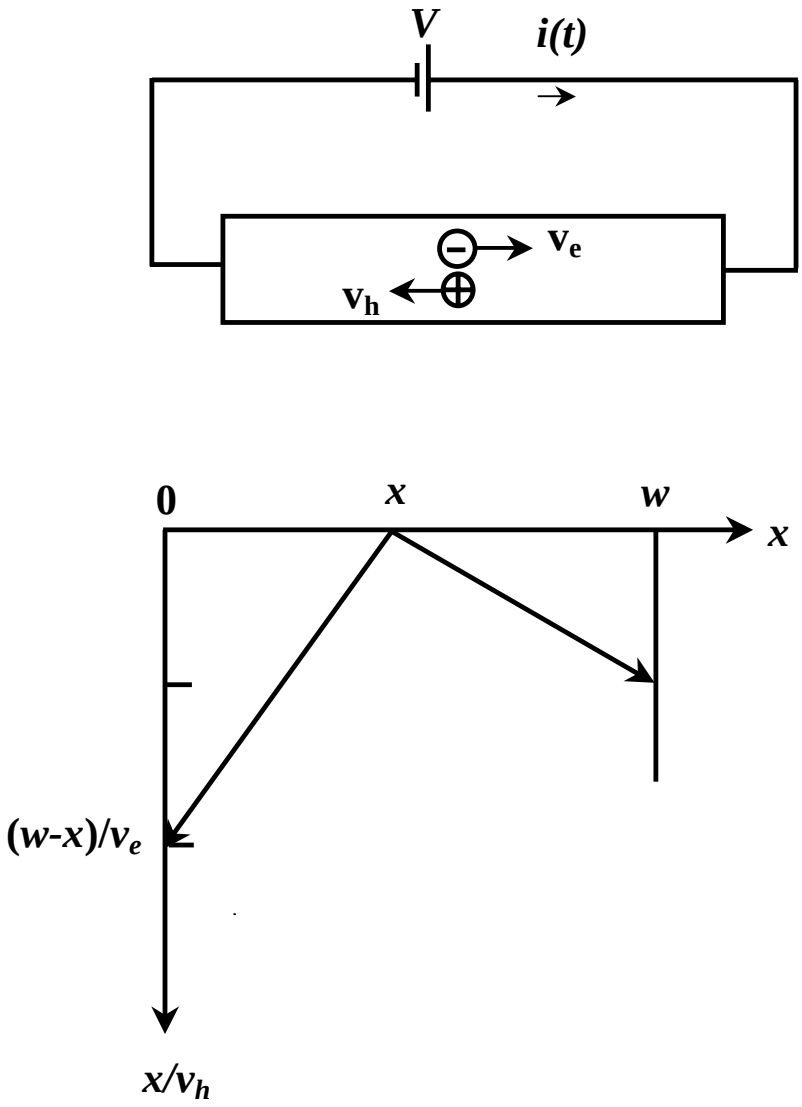

Figure 4.1 An electron-hole pair is generated at the position x. The hole moves to the left with velocity v_h and electron moves to the right with velocity v_e.

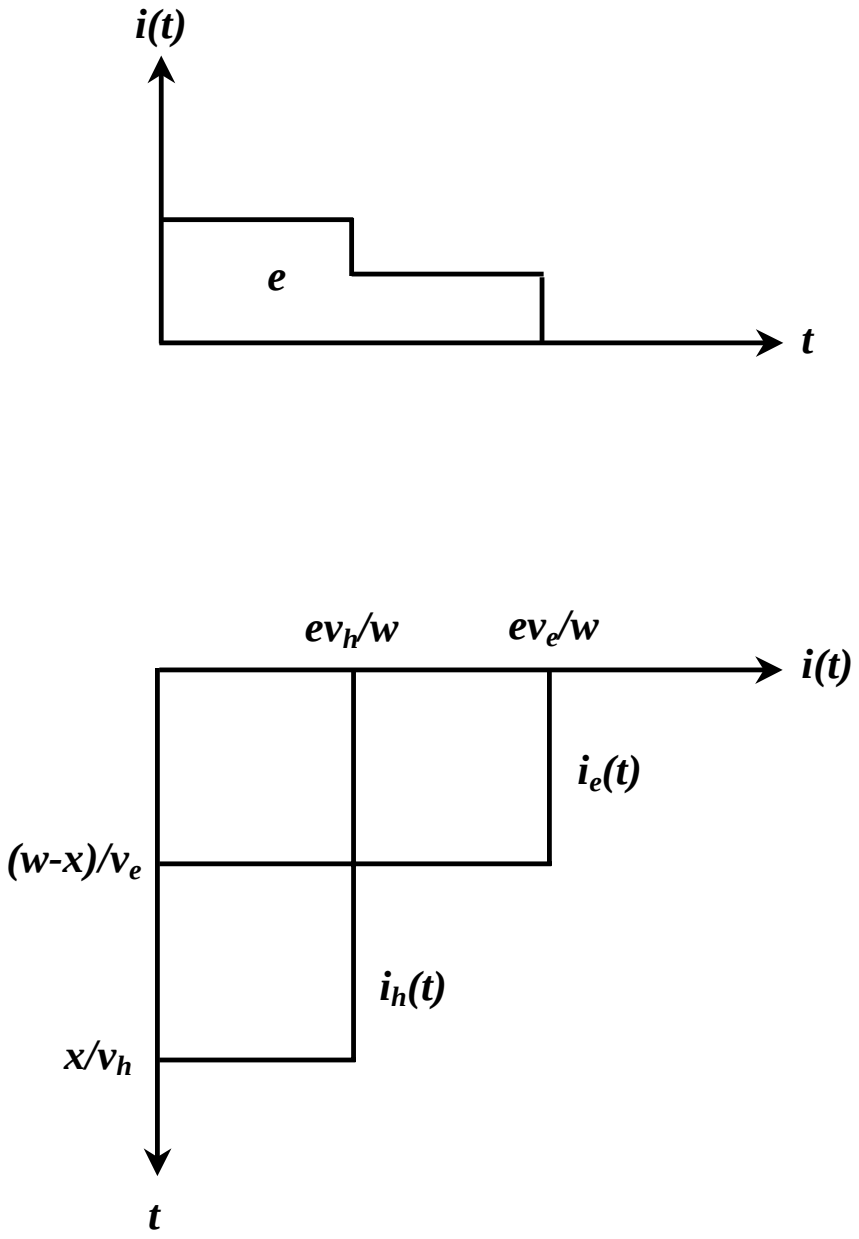

Figure 4.2 Hole current $i_h(t)$, electron current $i_e(t)$, and total current $i(t)$ induced in the circuit.

Assuming that the hole moves with constant velocity v_h to the left, and the electron moves with constant velocity v_e to the right, from equation 4-7, the hole current is $i_h = -e(-v_h)/w$ and the electron current $i_e = -e(-v_e)/w$, as illustrated in Figure 4-2. Each carrier contributes to the current as long as it is moving. If the carriers continue their motion until they reach the edge of the material, the hole moves for a time x/v_h, and the electron moves for time $(w-x)/v_e$. In semiconductors, v_e is generally larger than v_h so that the full width of the transit-time spread is x/v_h.

The total charge q induced in the external circuit is the sum of the areas under i_e and i_h

$$q = e\frac{v_h}{w}\frac{x}{v_h} + e\frac{v_e}{w}\frac{w-x}{v_e} = e. \qquad (4\text{-}9)$$

The result is independent of the position x at which the electron-hole pair was created. It indicates that although a photo generates an electron-hole pair in a photodetector material, the charge generated in an external circuit is e.

The transit-time spread is even more severe if the electron-hole pairs are generated uniformly through the material, as shown in Figure 4-3. For $v_h < v_e$, the full width of the transit-time spread is then w/v_h rather than x/v_h. This occurs because uniform illumination produces carrier pairs, including at $x = w$, which is the point at which the holes have farthest to travel before being able to recombine at $x = 0$.

Another response-time limit of semiconductor detectors is the *RC* time constant formed by the resistance *R* and capacitance *C* of the photodetector and its circuitry. The combination of resistance and capacitance serves to integrate the current at the output of the detector, and thereby to lengthen the impulse-response function. The impulse-response function in the presence of transit-time and simple *RC* time-constant spread is determined by convolving *i(t)* in Figure 4-2 with the exponential function $(1/RC)\exp(-t/RC)$. Photodetectors of different types have other specific limitation on the speed of response. [63]

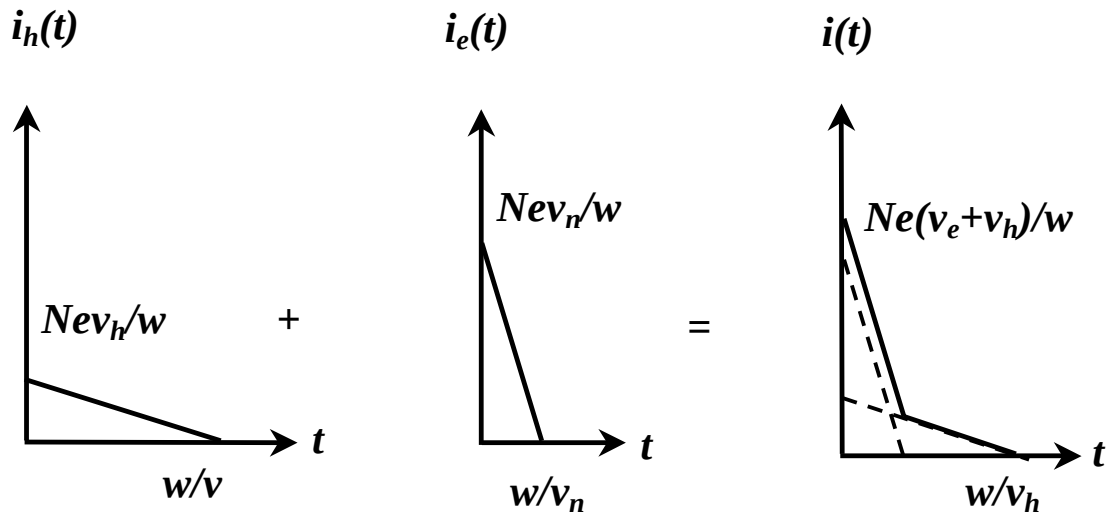

Figure 4.3 Hole current $i_h(t)$, electron current $i_e(t)$, and total current $i(t)$ induced in the circuit for electron-hole generation by N photos uniformly distributed between 0 and w.

4.1.2 Photoconductors

When photos are absorbed by a semiconductor material, mobile charge carriers are generated (an electron-hole pair for every absorbed photo). The electrical conductivity of the material increases in proportional to the photo flux. An electrical field applied to the material by an external voltage source causes the electrons and holes to be transported. This results in a measurable electric current in the circuit, as shown in Figure 4-4. Photoconducotor detectors operate by registering either the photocurrent i_p, which is proportional to the photo flux Φ, or the voltage dropped across a load R placed in series with the circuit.

Semiconductor material may take the form of a slab or a thin film. The anode and cathode contacts are often placed on the surface of the material, interdigitaling with each other to maximize the light transmission while minimizing the transit time (see Figure 4-4). Light can also be admitted from the bottom of the device if the substrate has a sufficiently large bandgap (so that it is not absorptive).

The increase in conductivity arising from a photo flux (photos per second) illuminating a semiconductor volume wA may be calculated as follows. A fraction η of the incident photo flux is absorbed and gives rise to excess electron-hole pairs. The pair-generation rate R (per unit volume) is therefore $R = \eta\Phi / wA$. If τ is the excess-carrier recombination lifetime, electrons are lost at the rate $\Delta n / \tau$ where Δn is the photoelectron concentration. Under steady-state conditions both rate are equal ($R = \Delta n / \tau$) so that $\Delta n = \eta\tau\Phi / wA$. The increase on the charge carrier concentration therefore results in an increase in the conductivity given by[64]

$$\Delta\sigma = e\Delta n(\mu_e + \mu_h) = \frac{e\eta\tau(\mu_e + \mu_h)}{wA}\Phi, \qquad (4\text{-}10)$$

where μ_e and μ_h are the electron and hole mobilities. Thus the increase in conductivity is in proportion to the photo flux.

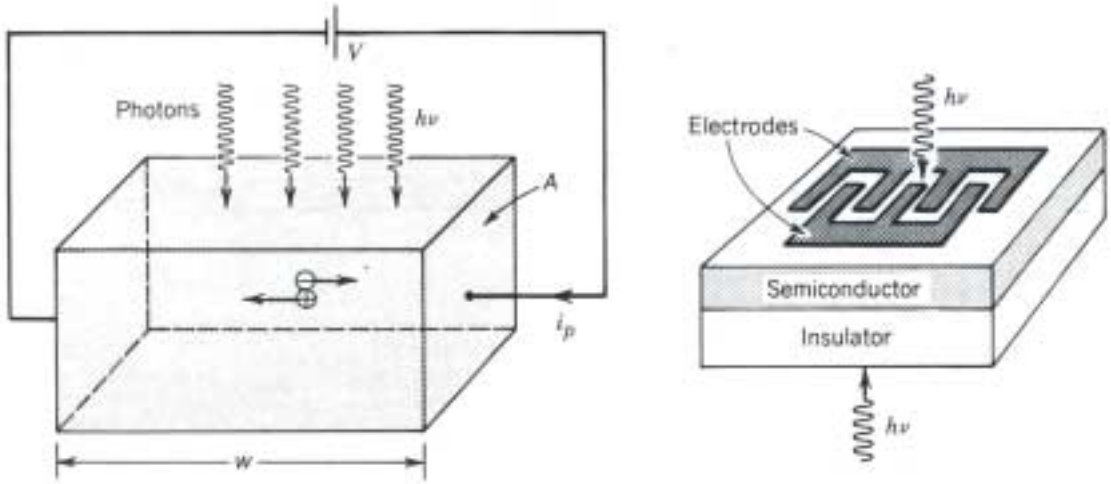

Figure 4.4 Schematic drawing of the photoconductor detectors.

Since the current density $J_p = \Delta\sigma E$ and $v_e = \mu_e E$ and $v_h = \mu_h E$ where E is the electric field, gives $J_p = [e\eta\tau(\mu_e + \mu_h)/wA]\Phi$ corresponding to an electric current $i_p = AJ_p = [e\eta\tau(\mu_e + \mu_h)/w]\Phi$. If $\mu_h << \mu_e$ and $\tau_e = w/v_e$,

$$i_p \approx e\eta\frac{\tau}{\tau_e}\Phi. \qquad (4\text{-}11)$$

In accordance with equation 4-5, the ratio τ/τ_e in equation 4-11 corresponds to the detector gain.

4.1.2.1 Gain in Photoconductor. The responsivity of a photoconductor is given by equation 4-3. The device exhibits an internal gain which, simply viewed, comes about because the recombination lifetime and transit time generally differ. Supposed that electrons travel faster than holes and that the recombination lifetime is very long, as the electron and hole are transported to opposite sides of the photoconductor, the electron completes its trip is sooner than the hole. The requirement of current continuity forces the external circuit to provide another electron immediately, which enters the device from the wire at the left. This new electron move quickly toward the right, again completing its trip before the hole reaches the left edge. The process continues until the electrons recombine with the holes. A single photo absorption can therefore result in an electron passing through the external circuit many times. The expected number of trips that the electron makes before the process terminates is

$$G = \frac{\tau}{\tau_e}, \qquad (4\text{-}12)$$

where τ in the excess-carrier recombination lifetime and $\tau_e = w/v_e$ in the electron transit time across the sample. The charge delivered to the circuit by a single electron-hole pair in this case is $q = Ge > e$ so that the device exhibits gain.

However, the recombination lifetime may be sufficiently short such that the carriers recombine before reaching the edge of the material. This can occur provided that there is a ready availability of carriers of the oppose type for recombination. In that case $\tau < \tau_e$ and the gain is less than unity so that, on average, the carries contribute only a fraction of the electronic charge *e* to the circuit. Charge is conserved and the many carrier pairs present deliver an integral number of electronic charges to the circuit. In the case of hole traps, the excess holes are trapped and the excess electrons and the holes are separated, the electrons are difficult to recombine with the holes. This results in very large excess carrier lifetime and gain.

4.1.2.2 Response Time. The response time of photoconductor is constrained by the transit-time and *RC* time-constant. The capacitance of photodetector is small. The carrier-transport response time is approximately equal to the recombination τ. Since the gain *G* is proportional to τ in accordance to equation 4-11, increasing τ increases the gain, so does the responsivity, which is desirable, but it also increase the response time, which is undesirable.

4.2 ZnO-based UV Photoconductors

ZnO has a direct and wide band gap of 3.3 eV at room temperature, which can be used for ultraviolet (UV) photo detection. Its high radiation hardness enables it to be used in harsh environment.[65] ZnO UV detector is expected to be found in many applications, such as solar UV radiation monitoring, ultra-high temperature flame detection, and airborne missile warning systems, etc.[66]

It is known that oxygen chemisorption plays a central role on regulating the photosensitivity of bulk or thin film ZnO, where a UV-sensitivity of similar magnitude has been observed.[67] In the dark, oxygen molecules adsorb on the film surface as negatively charged ions by capturing free electrons from n-type ZnO, thereby creating a depletion layer with low conductivity near the film surface:

$O_2(g) + e^- \rightarrow O_2^-(ad).$ (4-13)

When the light with energy higher than the fundamental absorption band of the ZnO is illuminated, photo-generated holes migrate to the surface, and discharge the adsorbed oxygen ions through surface electron-hole recombination, and destruct the depletion layer, increasing the conductivity:

$h^+ + O_2^- \rightarrow O_2(g).$ (4-14)

At the same time, the photo-generated electrons also significantly increase the conductivity of the films.

Chemisorption and photodesorption are slow processes, which were dominant in polycrystalline ZnO due to multiple grain boundaries and surfaces. For fast process to be dominant, it is critical that the quality of ZnO film should be improved to reduce trap density and minimize carries recombination. Further improvement on the photoresponse speed can be achieved by suppressing the effects due to O_2 adsorption-photodesorption through reduction of the electron concentration and surface passivation isolating the ambient from ZnO surface.

Due to the oxygen chemisorption effect, the photoresponse of ZnO based UV photoconductors is strongly dependent on the ambient gas condition, being slow in vacuum and inert gases, and fast in the air.[67] With the material size becoming small, chemisorption effect on the performance of the devices becomes significant. Surface modification becomes essential for the improvement of the performance of the devices. In this study, we have grown high quality ZnO epilayers on sapphire substrates, which is critical for the performance of ZnO UV photoconductors. We investigated the oxygen plasma treatment on ZnO epilayers. It demonstrated that oxygen plasma treatment is an efficient way to suppress the oxygen chemisorption of thin ZnO epilayers. For the first time, we developed and demonstrated high responsivity, high speed UV photoconductors based on the oxygen plasma treated thin (20 nm) ZnO epilayers.

4.2.1 Experimental Works

ZnO epitaxial films used in this study were grown on *c*-plane sapphire substrates with a radio-frequency magnetron sputtering technique. A 5N-purity target was used in conjunction with Ar/O_2 gas as an ambient gas for sputtering. The films were deposited at 700 ºC. The following deposition parameters were optimized to obtain highly epitaxial ZnO films: target to substrate distance (1.75–2.25 inches), rf power (50-80 W), and gas pressure (2–10 mTorr). The x-ray diffraction θ-2θ scans and ω rocking curves were performed to determine the crystalline quality of the films. The electrical properties of the ZnO films were determined by transfer length method. ZnO UV photodetectors with interdigital metal electrodes were fabricated and characterized with MSM structures. To characterize the UV detectors, He-Cd laser with wavelength 325nm is as the excitation source. A HP 4145B semiconductor parameter analyzer was employed for current-voltage (I-V) characterization and temporal response measurements. ZnO oxygen plasma treatment was performed in ICP oxygen plasma produced with Unaxis 790 series plasma processing system at room temperature. The rf power was 100W-500W, oxygen pressure 3-15mTorr and flowing at 10-30 sccm. Time was varied from 1 minute to 60 minutes. After oxygen plasma treatment, ZnO electrical property measurement was performed. MSM UV photodetectors with oxygen plasma treated ZnO epilayers were also fabricated and characterized.

4.2.2 Results and Discussion

4.2.2.1 Oxygen Plasma Treatment on ZnO Epilayers. The crystalline nature of the ZnO films before and after oxygen plasma treatment was characterized through X-ray diffraction. Although the results are not shown here, XRD Ψ scan and pole Figure analysis results reveal that ZnO orients itself with sapphire substrate in such a way that the lattice mismatch is small (i.e., reduced to 18% level form nominal mismatch of 32%) and the anisotropic interfacial energy is lowered.[68] In other word, ZnO grows with its lattice 30-degree rotated in plane with respective to sapphire, showing epitaxial relationship of ZnO[1120]//sapphire[1010] along the in-plane direction and ZnO[0002]//sapphire[0002] along vertical direction. Figure 4-5 shows θ-2θ scans of a ZnO (with nominal thickness 20 nm) epilayer grown on sapphires, in which solid line is obtained before oxygen plasma treatment, the dashed line is obtained after treatment. The peak at $2\theta = 34.4\ ^\circ$ is ZnO (0002) diffraction peak. Peak at $2\theta = 36.4\ ^\circ$ is from sapphire (006) crystalline

planes. The Figure shows that the sapphire peaks has negligible shift, but the ZnO peak shifts to lower 2θ angle after oxygen plasma treatment. It indicates that the oxygen plasma treatment increases the strain of ZnO epilayer and the ZnO lattice elongates along the vertical direction. It is probably due to the diffusion of oxygen radicals into ZnO, which occupy the oxygen vacancies, as the as-grown ZnO is usually zinc-riched and there exist oxygen vacancies.[69]

Compared these two curves, there is no significant difference in terms of peak intensity and curve patterns, which indicates that the oxygen plasma treatment has no significant effect on the crystalline microstructure of ZnO epilayer. As the inductively coupled plasma (ICP) has high-radical concentration, but low sheath voltage.[70] In this Figure, we observe the interference fringes on the wings of ZnO (0002) diffraction peak. The fringes arise when an X-ray beam is diffracted by a thin nearly perfect heteroepitaxial layer.[71] This indicates the films in this study have high quality with excellent interface. From the fringe space, we calculated the thickness of the ZnO epilayer is about 18nm, which is approximately equal to the nominal thickmess. The fringe space in the curve after oxygen plasma treatment is a littile larger than that of curve before oxygen plasma treatment. It indicates that the oxygen plasma has a little etching effect on ZnO epilayer, but it is very small. Figure 4-6 shows the ω-rocking curves of the ZnO(0002) diffraction peak of the sample, solid line is from as-deposited sample, dashed line is after oxygen plasma treatment. Two distinct features are clearly observed: a sharp specular peak with a full-width-half maximum (FWHM) of 0.02°, which is resolution-limited, and a much broader diffusion part with FWHM of ~2°. The specular part arises from the initial well-aligned ZnO part on sapphire. The diffusion part is due to generation of misfit dislocation resulting in out-of plane tilt, i.e., mosaicity.[72]

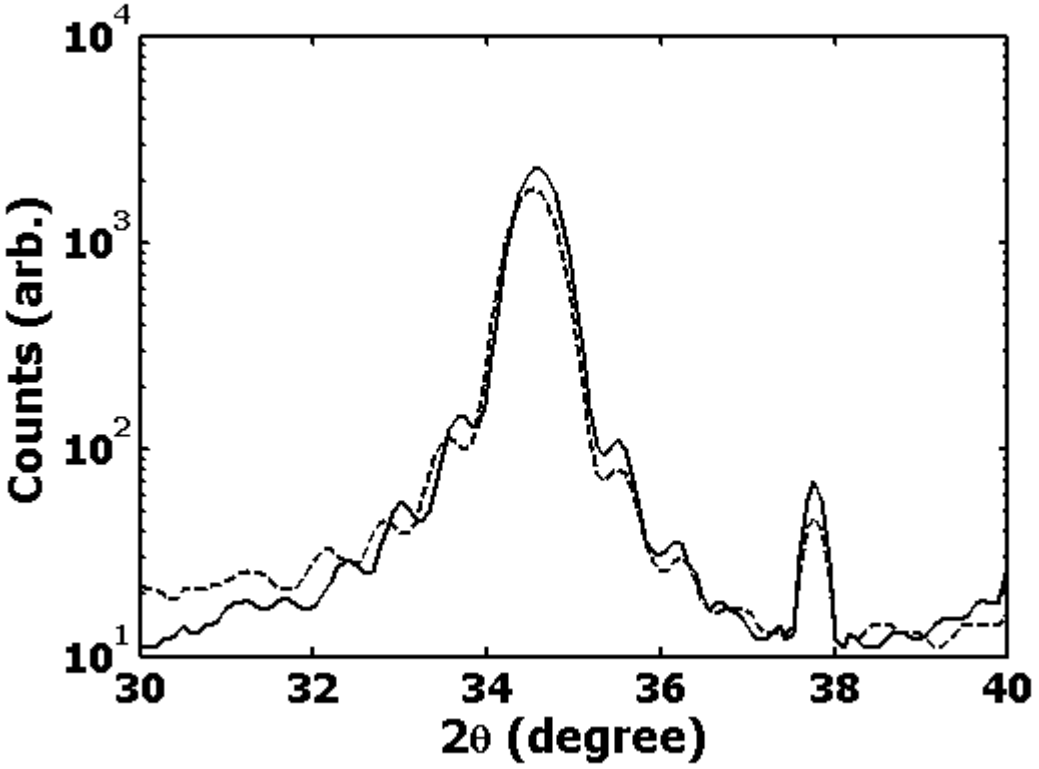

Figure 4.5 XRD θ-2θ scans of a ZnO film with nominal thickness 20 nm, solid line: as-deposited; dashed line: after oxygen plasma treatment.

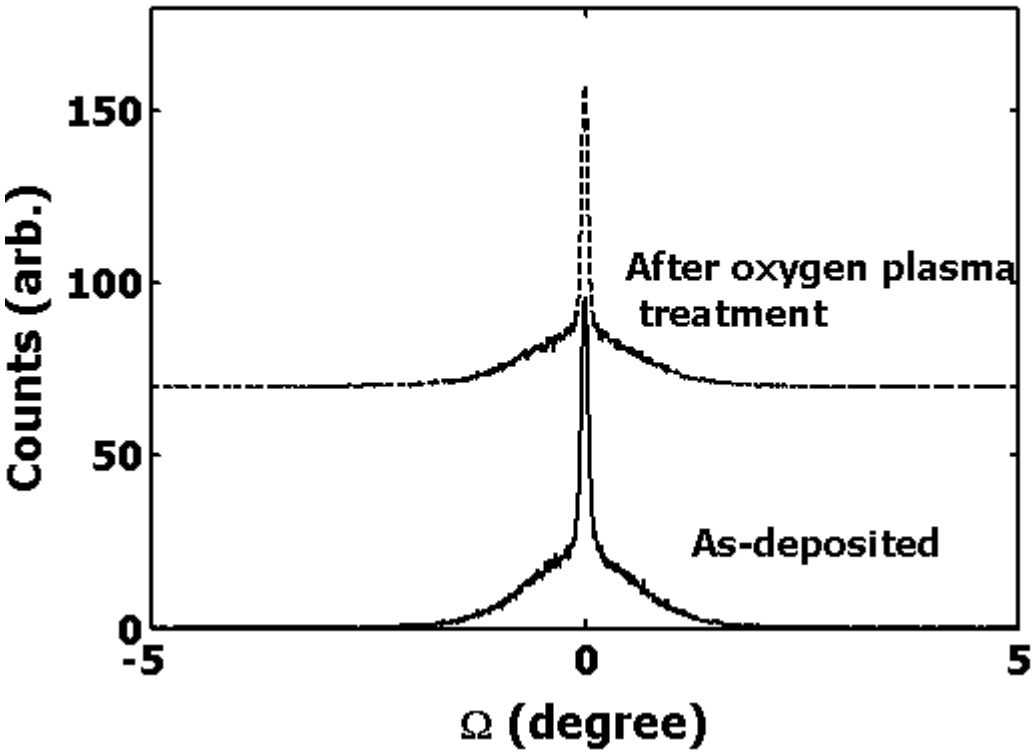

Figure 4.6 XRD Ω rocking curves of a ZnO film (same as Figure 4-5), solid line: as-deposited; dashed line: after oxygen plasma treatment.

To test the stability of oxygen plasma treatment effect on ZnO epilayers (with nominal thickness 20 nm), we annealed the treated samples at different temperatures from 300°C to 650°C in the vacuum (5×10^{-5} Torr) for 30 minutes. Their sheet resistance was measured, shown in Figure 4-7, in which the sheet resistance was plotted as a function of annealing temperature. All the samples were treated with oxygen plasma at room temperature, rf power 125W, oxygen pressure15mTorr and flowing at 30 sccm. It shows that the oxygen plasma treatment increases the sheet resistance more than 7 orders, which is due to the diffusion of the radical oxygen and occupation of oxygen vacancies in ZnO epilayers. In ICP oxygen plasma, there exists a high-radical concentration. The electrical properties of treated samples is stable to vacuum annealing at temperature ~ 300°C. Figure 4-7 also shows that, in this study, the sheet resistance is recovered to its original value after annealing at 500°C. For comparison, in Figure 4-7, we also show the annealing behavior of the as-grown (without oxygen plasma treatment) samples, illustrating that annealing at temperature below ~ 500°C has a negligible effect on the sheet resistance of as-grown samples. The sheet resistance of as-deposited and treated samples dramatically decreases after annealed at 650°C, which is probably due to outdiffusion of oxygen components resulting in higher oxygen vacancy concentration and higher carrier concentration.

We also investigated the penetration depth of oxygen plasma through ZnO epilayers. In this study, we varied the treatment time from 1 minute up to 60 minutes, and kept other parameters the same. The film thickness is 800 nm. Figure 4-8 shows the sheet resistance of the film as a function of treatment time. The sheet resistance increases fast at the early stage, then gradually become slow. Considering the thickness of ZnO film is as thick as 800 nm, it is impossible for oxygen plasma to penetrate the whole thickness. The oxygen plasma only has influence on the surface, as the treatment was performed at room temperature.

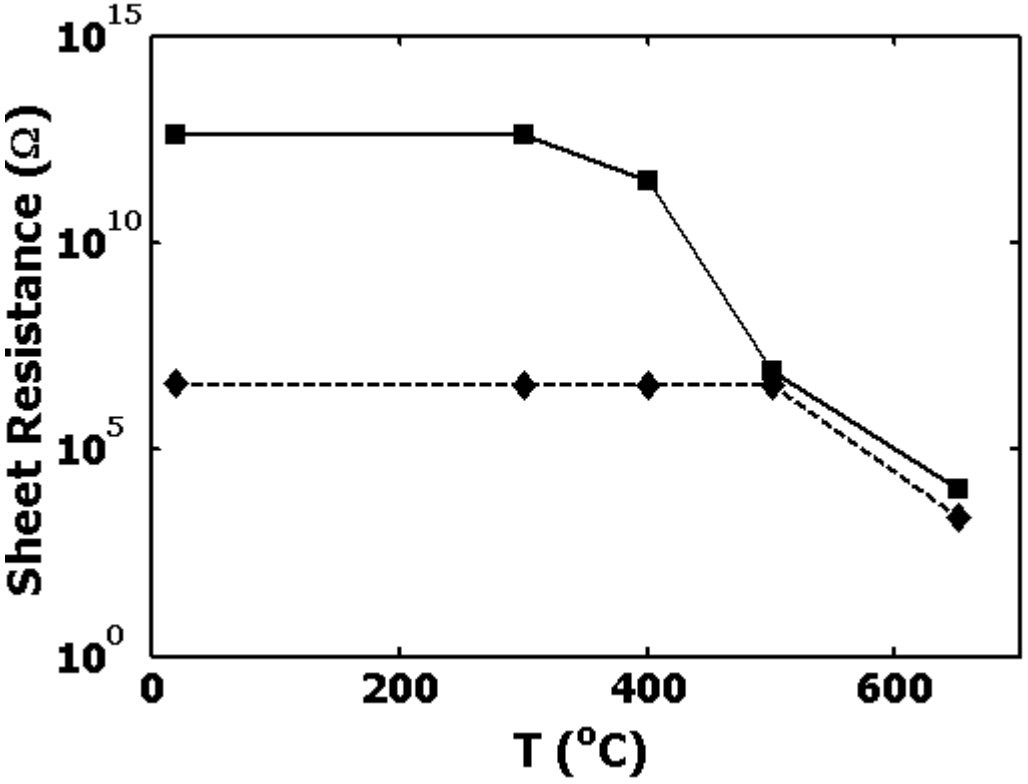

Figure 4.7 Sheet resistance as a function of annealing temperature for ZnO epilayers (20 nm) (Diamonds: as-deposited; squares: after oxygen plasma treatment).

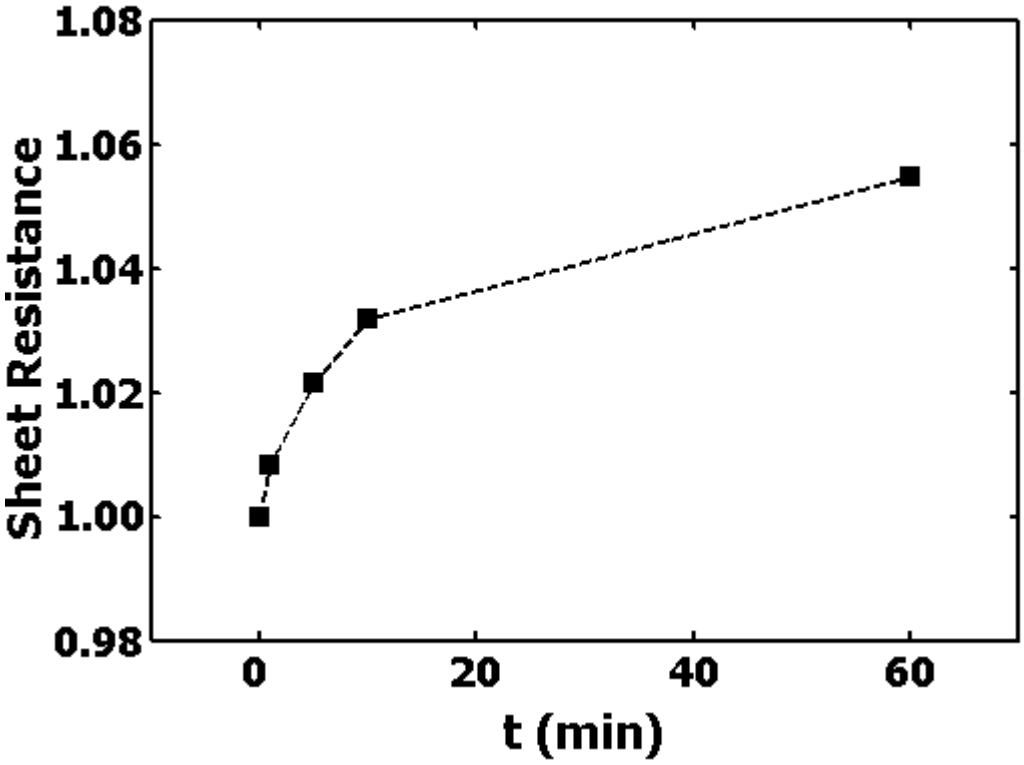

Figure 4.8 Normalized sheet resistance as a function of oxygen plasma treatment time for a ZnO epilayer (thickness 800 nm).

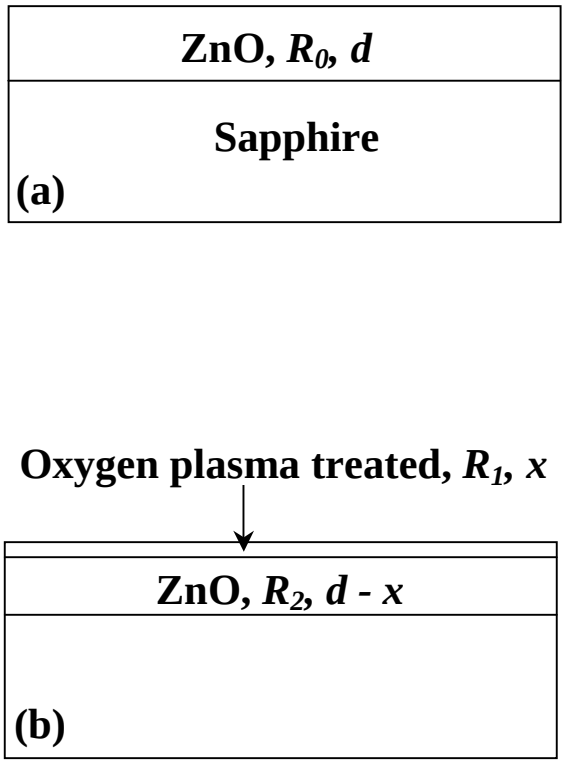

Figure 4.9 Schematic diagram of an as-deposited ZnO epilayer (a) after oxygen plasma treatment, ZnO epilayer modeled as a high resistive layer, *x*, and a bulk layer, d-*x*.

By comparing the oxygen-plasma induced high resistive layer near the surface with the bulk ZnO epilayer, a two-layer model is applied to explain the sheet resistance evolution with the treatment time, and to extract the penetration depth of the oxygen plasma. The cross section of an as-deposited ZnO epilayer and a oxygen plasma treated epilayer with two layers are illustrated schematically in Figure 4-9(a) and (b). Assumed a constant film thickness, *t*, for both as-deposited and oxygen plasma treated ZnO films, R_0 and R_t are measured sheet resistance for the as-deposited and treated films. According to the two-layer parallel resistor model, we have

$$R_t = \frac{R_1 R_2}{R_1 + R_2}, \qquad (4\text{-}15)$$

where R_1 and R_2 are sheet resistance of high resistive surface layer with thickness *x*, and bulk film with thickness *t-x*, as shown in Figure 4-9(b). As $R_1 >> R_2$, equation 4-15 can be simplified as $R_t \approx R_2$. Assuming bulk ZnO epilayer has uniform electrical properties, we have

$$R_0 = (1 - \frac{x}{d}) R_t \qquad \textbf{(4-16)}$$

and

$$x = (1 - \frac{R_0}{R_t}) d \,. \qquad (4\text{-}17)$$

Using equation 4-17, we calculated the oxygen plasma penetration depth, which are for treatment time 1 minute, 5 minutes, 10 minutes, and 60 minutes, 4 nm, 10 nm, 15 nm, 25 nm, respectively. It was estimated that the penetration depth was about 20 nm for 30 minutes treatment. It is possible that the whole film of ZnO epilayer with nominal thickness 20 nm is affected by the oxygen plasma and become high resistive.

4.2.2.2 Performance of ZnO-based UV Photodetectors. UV photodetectors were designed and fabricated based on MSM interdigital structure. Figure 4-10 is the photograph of a fabricated photodetector with size $50\times5220\mu m^2$. The interdigital metal electrodes are defined on ~ 1000 Å aluminum layer by conventional photolithography and lift-off processes, with finger width 16 μm, finger length 500 μm and finger space 50 μm. Linear I-V curves in the dark and under illumination of a photodetector with as-deposited ZnO epilayer (nominal thickness 20 nm) were obtained as shown in Figure 4-11. The detector operates in the photoconductive mode. Under 3V bias, the measured average dark current is ~ 5 mA, and the UV current ~5mA. The detector has a larger dark current, which is a disadvantage for practical use. It also has a large UV current, indicating a large photo responsivity, ~ 3000 A/W. Figure 4-12 shows the I-V curves of a photodetector with oxygen plasma treated ZnO epilayer and nominal thickness 20 nm. Under 3V bias, the measured average dark current ~ 400 pA, and UV current ~600 nA. The extremely low dark current is helpful to enhance the detector's signal to noise ratio (S/N) since the shot noise, which exceeds the Johnson and 1/f noise if the operating frequency is not too low, is proportional to the dark current.[73] The responsivity of this detector is ~ 50 A/W. These results show that the oxygen plasma treatment on thin ZnO epilayer increases the resistivity and reduces the dark current of the photodetector. This probably is due to the diffusion of radical oxygen in oxygen plasma into ZnO film and occupation of oxygen vacancies, resulting in the reduction of carrier concentration.

The responsivity measurement was performed on ZnO photoconductors (nominal thickness 20 nm) with He-Cd laser (wavelength 325 nm), as shown in Figure 4-13, in which circles represent data from as-deposited ZnO epilayer photodetector, diamonds represent data from oxygen plasma treated ZnO epilayer photodetector.

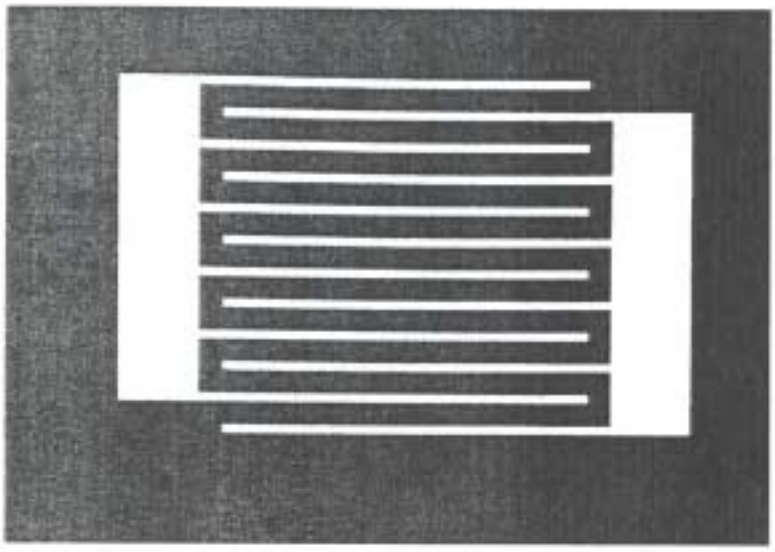

Figure 4.10 Photograph of a fabricated ZnO photodetector.

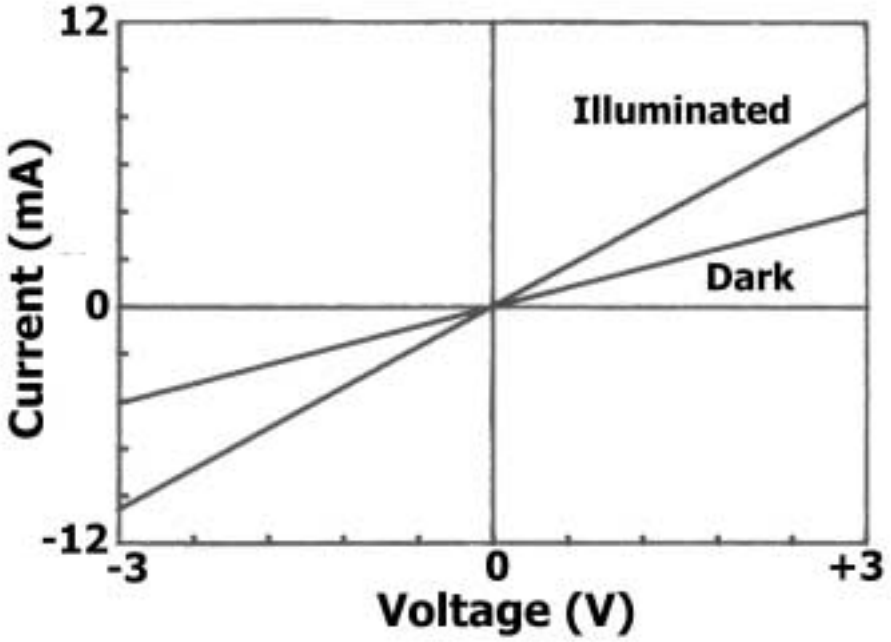

Figure 4.11 Dark and photoilluminated I-V characteristics of a ZnO (as-deposited, with nominal thickness 20 nm) MSM photodetector.

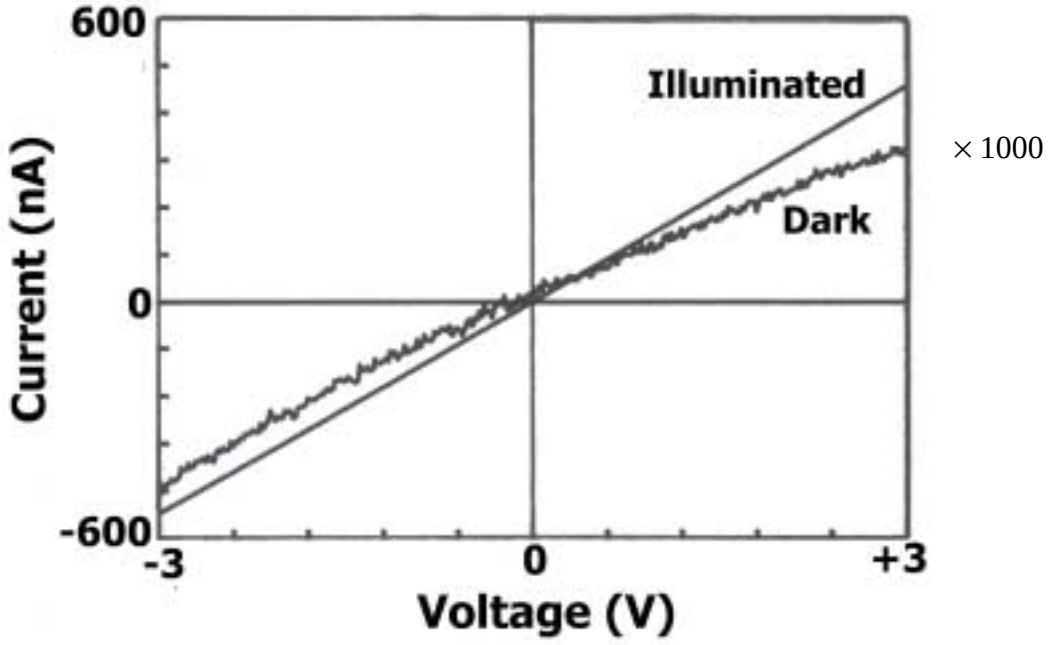

Figure 4.12 Dark and photoilluminated I-V characteristics of a ZnO (after oxygen plasma treatment, with nominal thickness 20 nm, same as Figure 4-11) MSM photodetector.

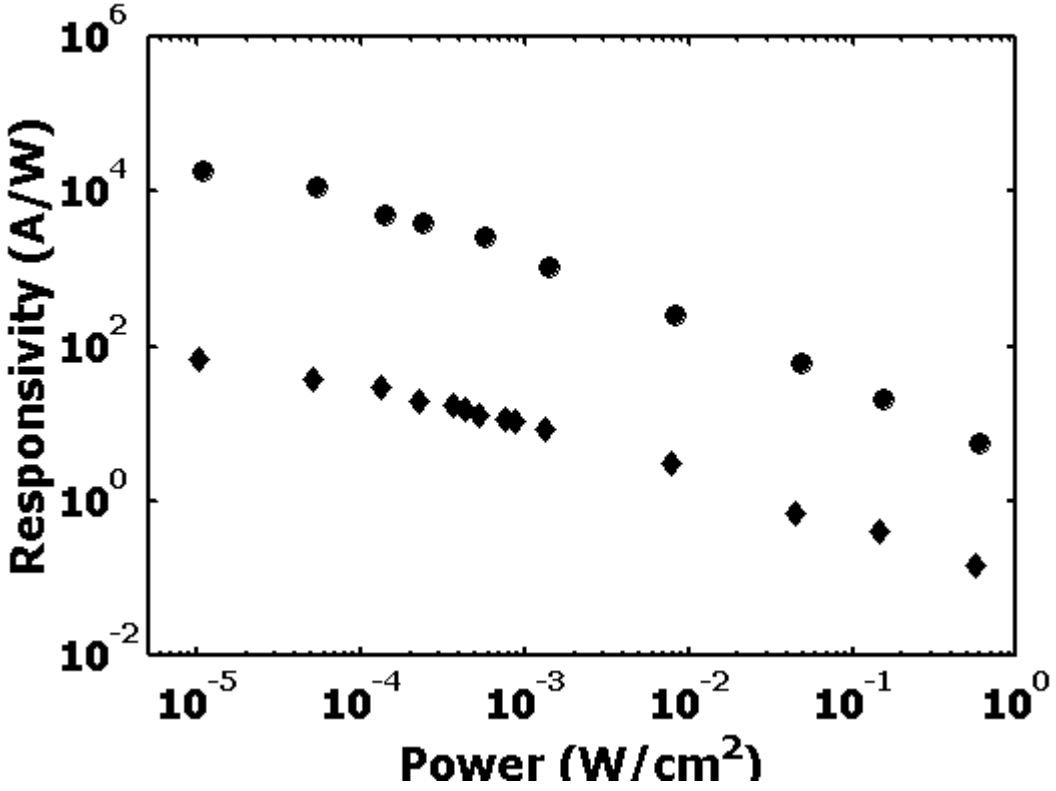

Figure 4.13 Responsivity as a function of power density for ZnO photoconductors with nominal thickness 20 nm (Circles: as-deposited; diamonds: after oxygen plasma treatment).

Temporal response of ZnO UV photodetectors, with as-deposited 20 nm ZnO epilayer is shown in Figure 4-14, and with oxygen plasma treated 20 nm ZnO epilayer shown in Figure 4-15&16. For as-deposited ZnO photodetectors, the UV photoresponse speed is very slow, indicating that the slow oxygen chemisorption process plays a dominant role in the UV response of the detector. After oxygen plasma treatment, the UV photoreponse speed of ZnO photodetector is very fast, with 10%-90% rise and fall time less than 40 μs. It indicates that the oxygen plasma treatment has effectively suppressed the chemisorption of ZnO epilayers. This point is further supported by the transient measurement results performed in the vacuum. Figure 4-17 shows the temporal response of ZnO UV photodetector with oxygen plasma treated 20 nm ZnO eipilayer in the air and in the vacuum chamber, 4×10^{-6} Torr. There is negligible difference, indicating that the photoresponse of the detector is independent of the ambient conditions. The photoresponse of ZnO UV photodetectors are usually strongly dependent on the ambient gas conditions, being slow in vacuum and inert gas, and fast in the air due to the oxygen chemisorption of ZnO.[74, 75] For comparison, temporal responses of detectors with as-deposited ZnO epilayers in the air and in the vacuum are also shown here. In the vacuum, the UV response speed is much slower than that in the air (Figure 4-18).

In the oxygen plasma, there are components O^+, O_2^+, O^* .[70] The positive ions neutralize the negatively charged oxygen molecular ions adsorbed on ZnO surface, and remove them from the ZnO surface. The radical oxygen atoms, O^*, diffuse into ZnO epilayer and occupy the oxygen vacancies, resulting in the reduction of carrier concentration, which suppresses the oxygen adsorption-photodesorption effects [76] and discussed in section 3. At the same time, the oxygen atoms occupy the surface sites of ZnO and passivate the dangle bonds, which make the ZnO surface less reactive and suppresses the oxygen chemisorption as well.

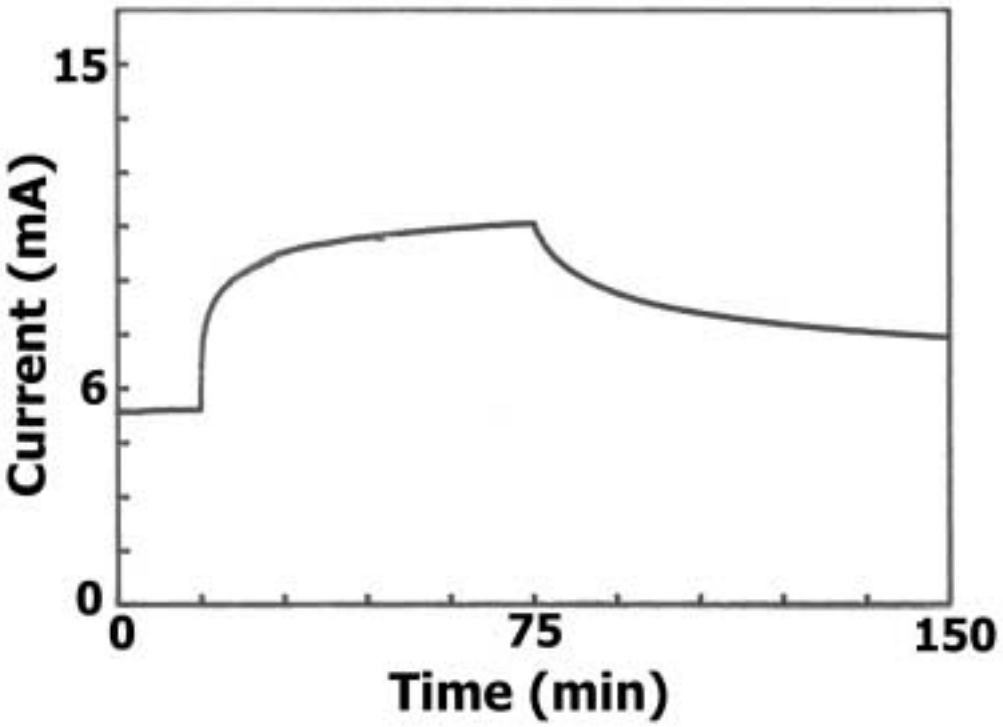

Figure 4.14 Temporal response of a ZnO photodetector (as-deposited, with thickness 20 nm, same as Figure 4-11).

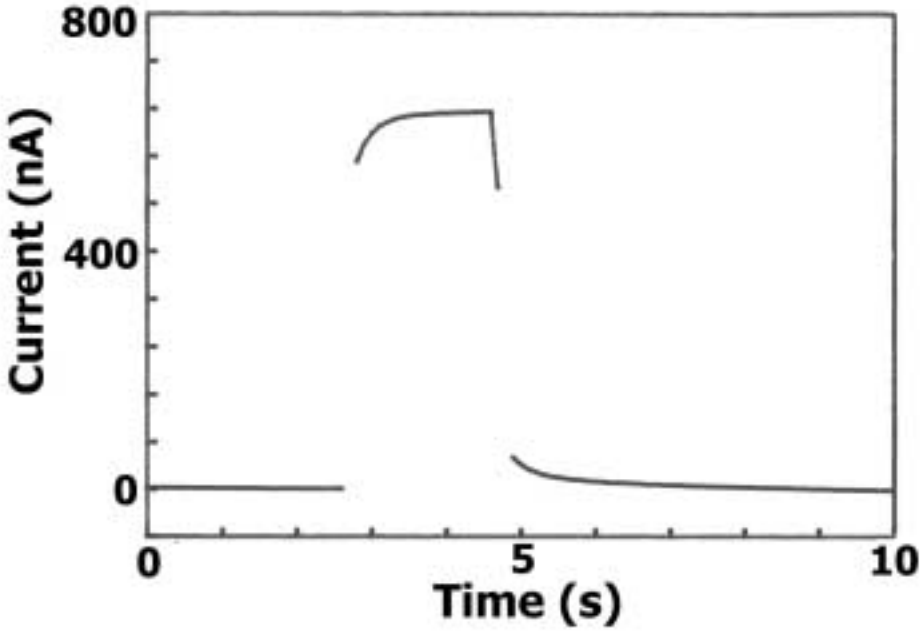

Figure 4.15 Temporal response of a ZnO photodetector (After oxygen plasma treatment with thickness 20 nm, same as Figure 4-12).

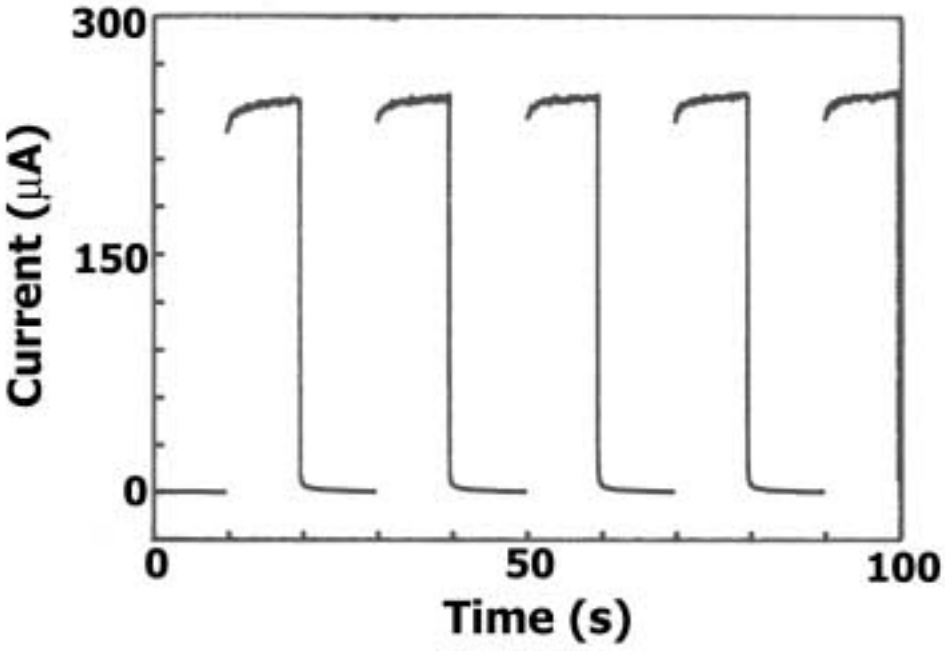

Figure 4.16 Temporal response of the ZnO photodetector (After oxygen plasma treatment with thickness 20 nm, same as Figure 12).

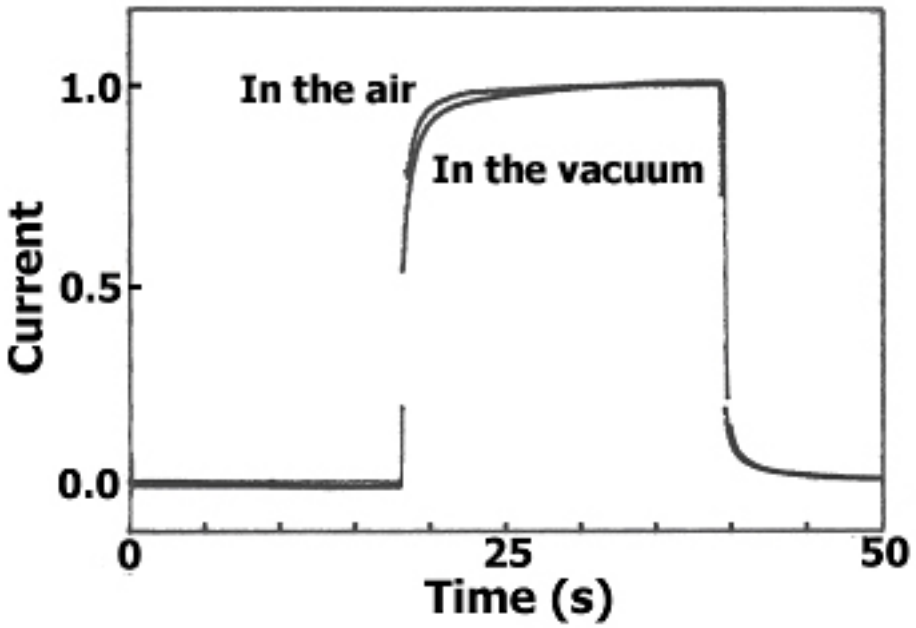

Figure 4.17 Temporal responses of UV photodetector with oxygen plasma treated ZnO thin film (20 nm) (In the air (1atm); in the vacuum (4×10^{-6} Torr), same as Figure 4-12).

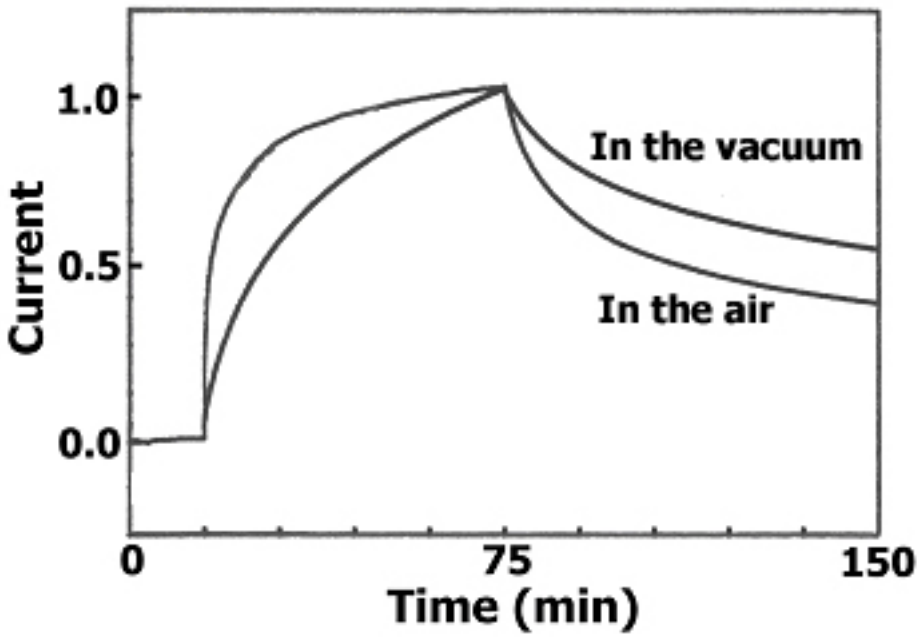

Figure 4.18 Temporal response of UV photodetector with as-deposited ZnO thin film (20 nm) (In the air (1atm); in the vacuum (4×10^{-6} Torr), same as Figure 4-11).

For comparison, ZnO thin epilayers (20 nm) were treated in oxygen ambient. In this experiment, an as-deposited ZnO epilayer wafer with nominal film thickness 20 nm were cut into four pieces, one is as reference, as-deposited; the second one was treated in oxygen plasma at room temperature; the third one was treated in oxygen ambient with pressure 10 Torr at 100°C, and the fourth one was treated in oxygen ambient with pressure 10 Torr at 300°C. Their structural and electrical properties were then characterized with XRD and TLM. Results show that oxygen ambient has negligible effects on the ZnO epilayers, but after oxygen plasma treatment, the sheet resistance of ZnO film increases more than four orders and the UV photoresponse speed increases as well in this study. It indicates that oxygen plasma treatment has unique effect on ZnO epilayers, which is an effective way to modify thin ZnO epilayers.

4.2.2.3 Thickness Dependence. Dark current of ZnO photoconductor is strongly dependent on the film thickness in this study, 5 mA for thickness of 20 nm, but 10μA for thickness of 500 nm, shown in Figure 4-19. Thin ZnO epilayer also has a slow photoresponse speed than that of thick film, as shown in Figure 4-20. These results are in contradiction with the observations of polycrystalline ZnO films grown on glass plates.[67] In their observations, the dark conductivity decreases exponentially with decrease of film thickness, and thin films have much larger magnitude and significantly faster response rate than thick films. These observations were explained by adsorption of oxygen on thin films surface and grain boundaries, which substantially lowers the effective carrier density, making the width of the barrier so thick as to effectively low the dark electrical conductivity. This mechanism can't explain our observations. There should be other factors that affect the conductance of the film in thin regime, such as dislocations and other defects. ZnO epilayer on sapphire is similar to that of GaN epilayer on sapphire. The larger lattice mismatch between epilayer and substrate may cause a highly dislocated sublayer near the interface. A high conductive layer (0.3 μm ~ 0.5 μm) at the interface between GaN and sapphire has been observed.[77] The conduction in the interface layer arises from a donor impurity band due to the incorporation of high levels of impurity and/or native defects during the initial stage of growth. Two-layer model, including the interface layer and the rest of layer, was proposed and succeeded explaining the electrical properties.[78] Two-layer model

seems to be unsuitable for explaining our observations. In our case, the resistivity of ZnO film increases almost four orders when the thickness decreases one order. A high conductive thin layer indeed forms at the very early stage of the growth. But with the proceeding of the growth, this high conductive layer gradually disappears or the difference is not significant between this initial layer and the following layer. It is probably due to the indiffusion of the oxygen radical during the deposition, which results in a relative uniform resistivity epilayer. At the deposition environment temperature, the vapor pressure of ZnO is about 1.5×10^{-7} Torr,[79] which is smaller than the deposition ambient pressure, 1×10^{-4} Torr. There is high probability for oxygen radical diffusion into ZnO film during the deposition process. In our case, thin ZnO epilayers have higher conductivity than those of thick film, as discussed in section 3, the higher the carrier concentration of the film, the more serious effect of the oxygen chemisorption on ZnO epilayer, i.e. larger surface potential, which results in the slow photoresponse speed of the thin film photoconductors.

The dependence of the photo responsivity on the film thickness is negligible, as shown in Figure 4-21. It suggests that chemisorption is dominant factor regulating the ZnO epilayer photo response in a wide thickness range (20 nm ~ 500 nm).

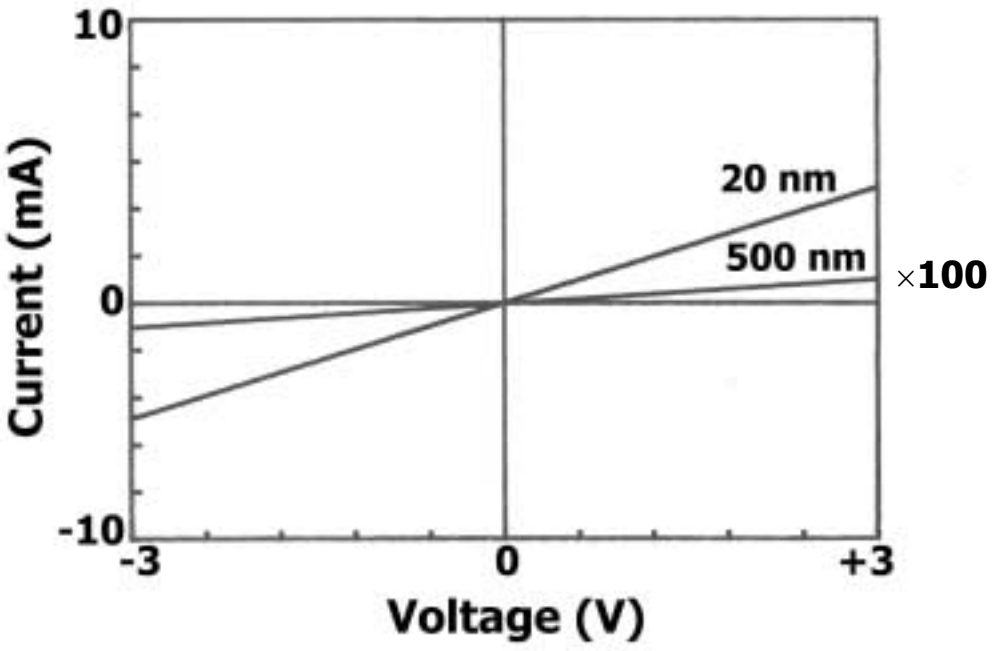

Figure 4.19 Dark I-V characteristics from ZnO (as-deposited) MSM photodetectors (with film thickness 500 nm and 20 nm).

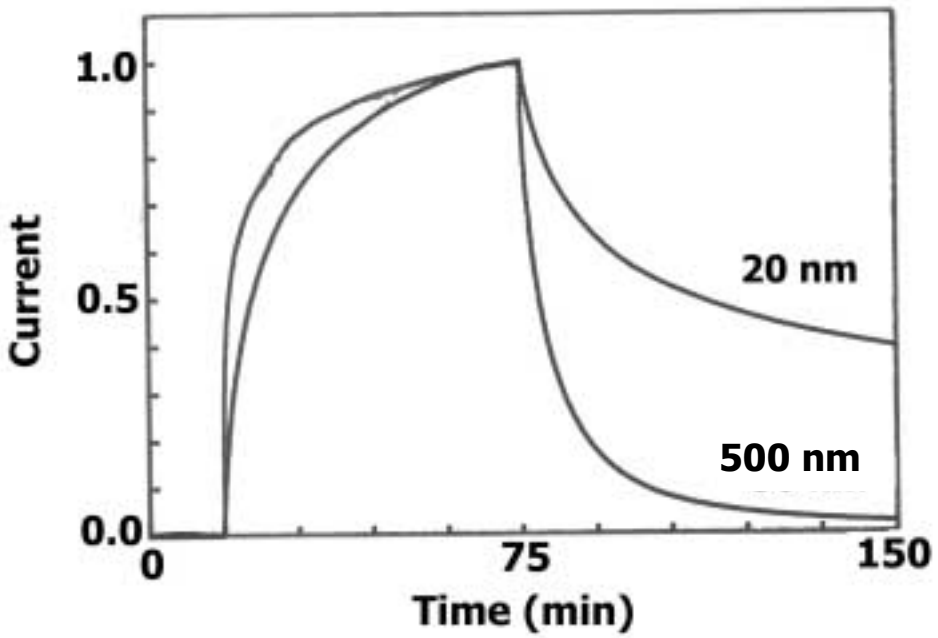

Figure 4.20 Temporal response from ZnO (as-deposited) MSM photodetectors (with film thickness 500 nm and 20 nm).

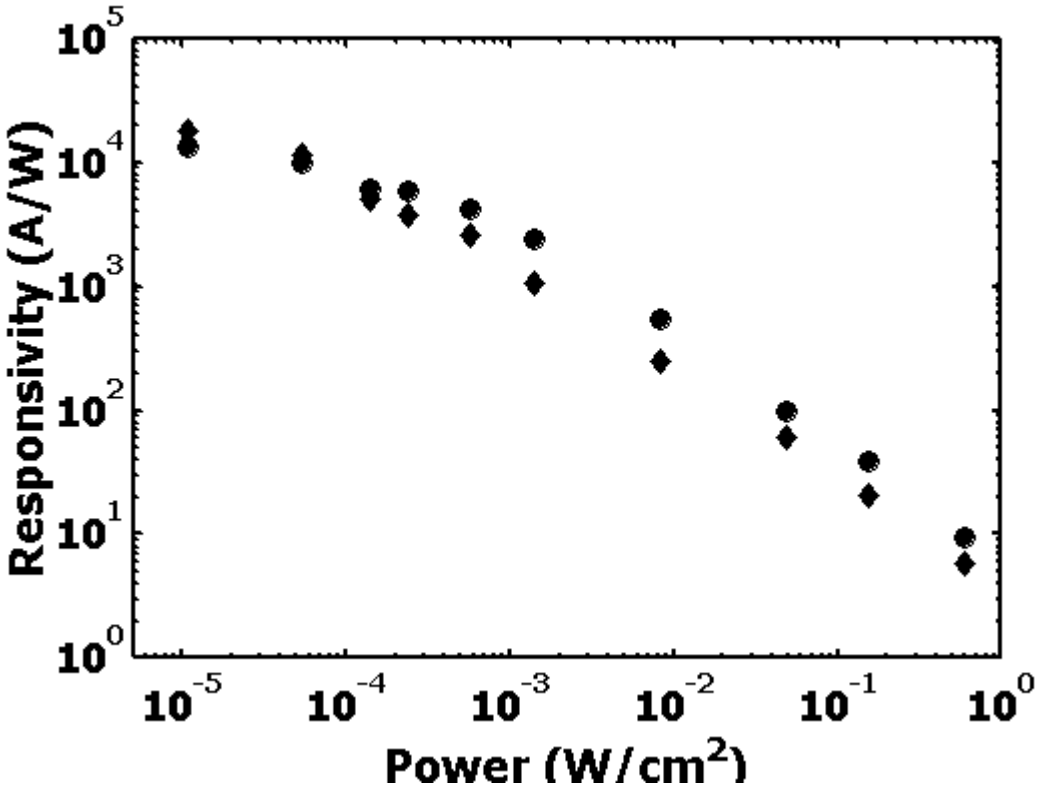

Figure 4.21 Resposivity of ZnO (as-deposited) MSM photodetectors as a function of power density (Circles: 500 nm; diamonds: 20 nm).

Oxygen plasma treatment on thick ZnO film has similar effects to the thin film except that the dark current has no significant reduction for the MSM structure after the treatment as oxygen plasma only affect the surface of the film. The oxygen plasma treatment also effectively suppressed the chemisorption of ZnO epilayer and increased the photoconductors' response speed. Figure 4-22 shows the temporal response of the photoconductors with as-deposited and oxygen plasma treated thick ZnO epilayer (500 nm). Oxygen plasma treated thick ZnO epilayer shows fast photo response. Figure 4-23 shows the temporal response of oxygen plasma treated thick ZnO epilayer in the air and in the vacuum (4×10^{-6} Torr). The air pressure has negligible affects on the photo response after oxygen plasma treatment, indicating that oxygen plasma treatment has effectively suppressed the chemisorption of thick ZnO epilayers. For comparison, temporal response in the air and in the vacuum (4×10^{-6} Torr) of as-deposited thick ZnO epilayer was plotted in Figure 4-24. In the vacuum, the response becomes very slow.

The dependence of responsity on power for thick film is similar to that of thin film, as shown in Figure 4-25, in which circles represent data from as-deposited ZnO epilayer, diamonds represent data from oxygen plasma treated ZnO epilayer, $R \propto P^{-k}$, here k = 0.8 for as-deposited film, k = 0.5 for oxygen plasma treated film.

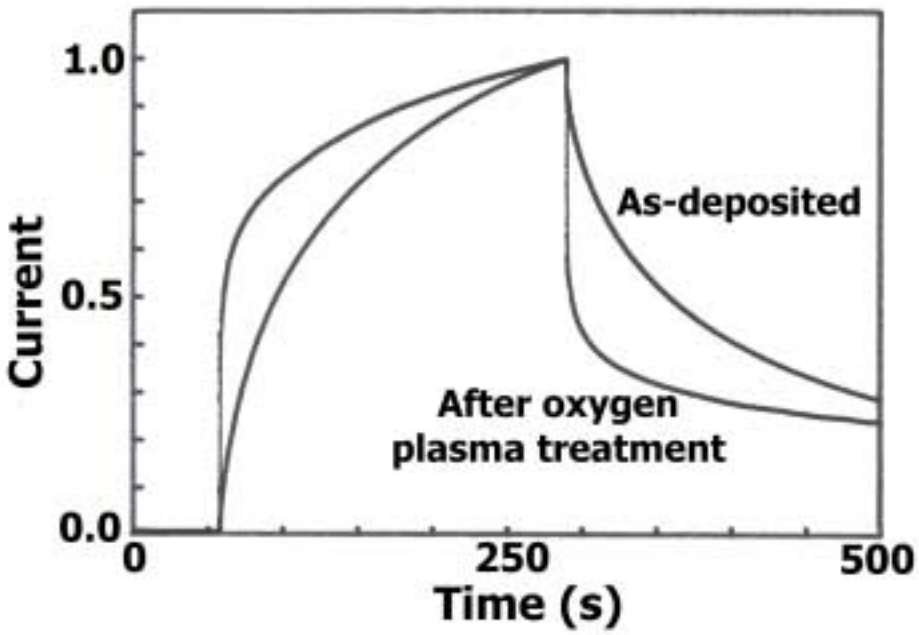

Figure 4.22 Temporal response of ZnO MSM photodetectors with thickness 500 nm (with as-deposited and after oxygen plasma treated epilayers).

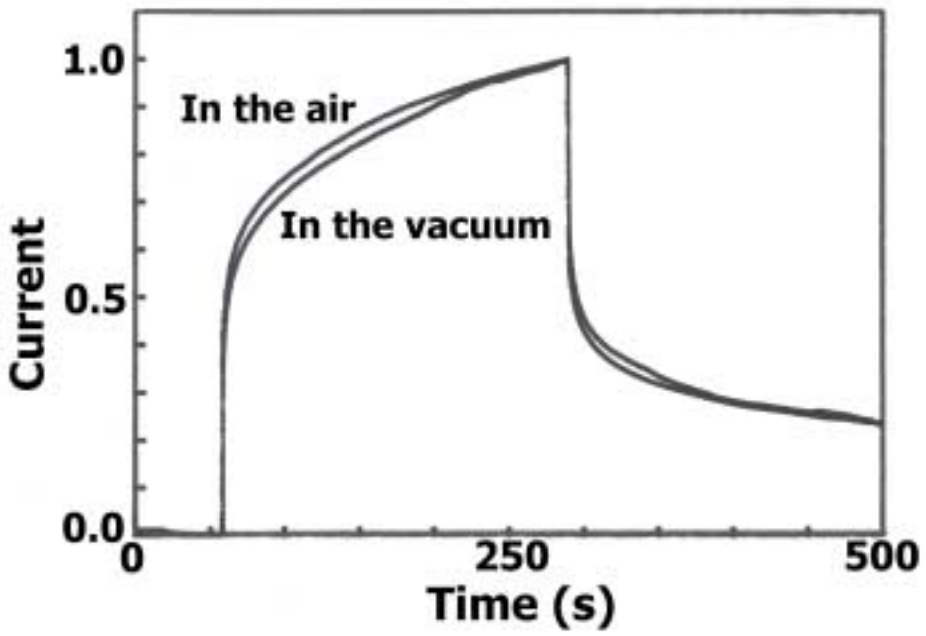

Figure 4.23 Temporal responses of a UV photodetector with oxygen plasma treated ZnO epilayer (500nm) (In the air (1atm) and in the vacuum (4×10^{-6} Torr)).

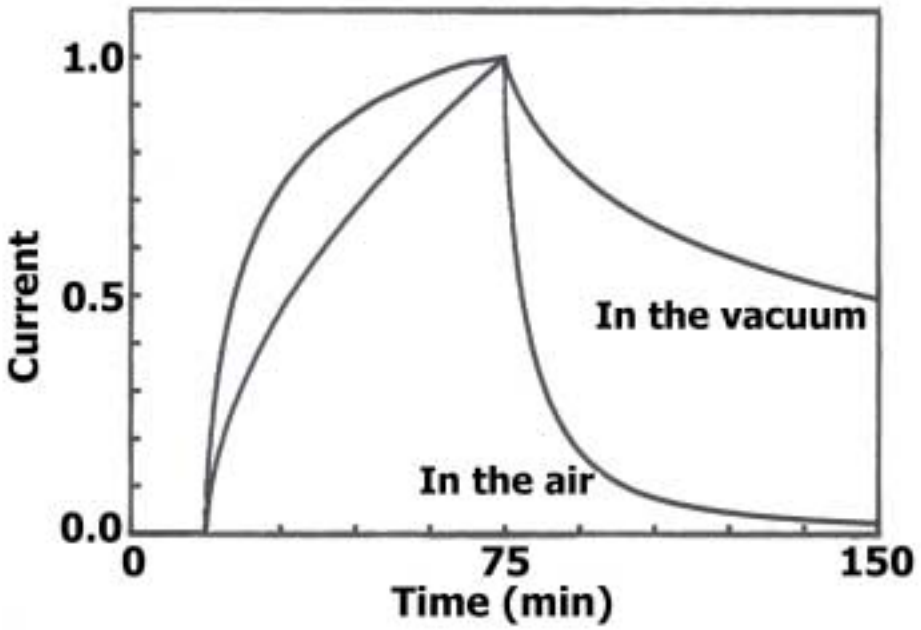

Figure 4.24 Temporal responses of a UV photodetector with as-deposited ZnO epilayer (500nm) (In the air (1atm) and in the vacuum (4×10^{-6} Torr)).

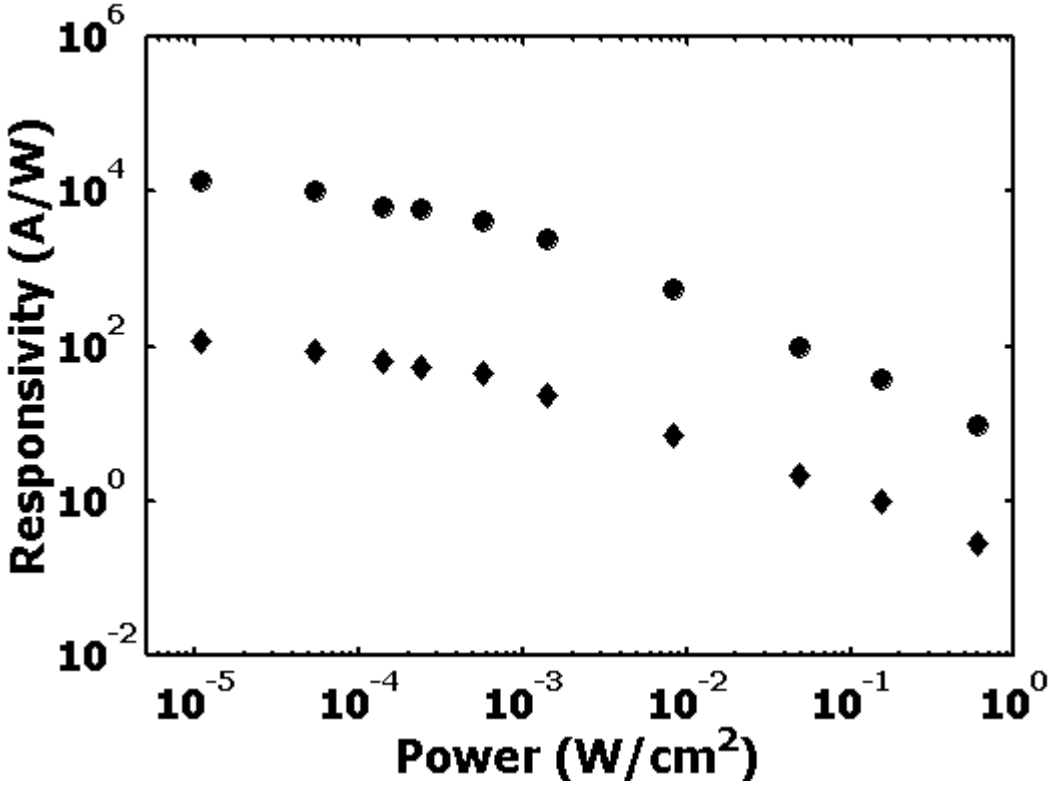

Figure 4.25 Responsivity of ZnO (500 nm) MSM photodetectors as a function of power density (Circles: as-deposited; diamonds: after oxygen plasma treatment).

4.3 Conclusions

We demonstrated high-quality ZnO epitaxial films grown on c-plane sapphire by a rf magnetron sputtering technique. We have investigated an oxygen-plasma treatment as a possible means of modifying/controlling the surface properties of ultra-thin (~20-nm-thick) ZnO epitaxial films. Oxygen plasma treatment is found to dramatically enhance the UV detection properties of ZnO, reducing the decay time constant and increasing the on/off ratio. Thus, for the first time, we have developed and demonstrated high speed, high reponsivity UV photodetectors with extremely low dark current using a single layer of nanometer-thick ZnO.

Oxygen plasma treatment has no significant effect on the crystalline structure of ZnO epilayers. Under room temperature, oxygen plasma only affects the surface electrical properties of ZnO epilayers. Oxygen plasma treatment is an effective way to suppress the chemisorption effect of ZnO epilayers. Oxygen plasma treatment is considered an effective way of making nanometer-scale ZnO viable for high performance UV optoelectronic devices. The effects observed in this study are also expected to be observable in other low-dimensional structures of ZnO, such as quantum dots, nano wires and ribbons.

5.0 MODELING OF ZNO UV DETECTORS

ZnO photoconductor shows high responsivity in the range 10^3-10^4A/W, and the responsivity dependence on incident power typically between $P^{-0.5}$ and $P^{-0.9}$. It is interesting to mention that a similar behavior, i.e. the power dependence of responsivity of $R \propto P^{-k}$ (k = 0.5-0.9), has been reported with GaN photoconductors.[80] The behavior was explained with a model based on the idea that space charge regions inside the semiconductor produce a variation of the conductive volume when carriers are photogenerated. One of the key assumptions of their model is that the degree of carrier modulation is negligible compared with the conductive volume modulation. It should be mentioned that this assumption may not always be valid as discussed below, and therefore the conductive volume modulation may not be a major factor that determines the power dependence of responsivity in some cases.

It is known that oxygen chemisorption plays a central role on regulating the photoconductance of bulk or thin film ZnO, where a UV response of similar magnitude has been observed.[81] In the dark, oxygen molecules adsorb on the film surface as negatively charged ions by capturing free electrons from n-type ZnO, thereby creating a depletion layer with low conductivity near the film surface. When the light with energy higher than the fundamental absorption band of the ZnO is illuminated, photo-generated holes migrate to the surface, and discharge the adsorbed oxygen ions through surface electron-hole recombination, and destruct the depletion layer, increasing the conductivity. At the same time, the photo-generated electrons also significantly increase the conductivity of the films.

5.1 Photo Responsivity of ZnO Photoconductors

Let us consider a photoconductor structure that has a length l, a across sectional area A (width w times thickness t), and n-type carrier concentration n. In most semiconductors, especially in wide bandgap materials such as GaN and ZnO, significant amount of surface and interface states are expected to exist near the film surface and in the grain boundary regions. Interaction of carriers with these states would result in formation of charge regions. The actual conductive volume is then expected to be different from the nominal value calculated from the

physical dimension of a photoconductor. For acceptor states, which capture electrons from the conductance band, a negative surface charge forms at the surface and results in the space charge region near the surface. For simplicity, only space charge region near film surface is taken into account in this work. The thickness of the conducting layer is reduced by the space charge region width t_s. The dark current can be expressed as follows,

$$I_d = \frac{t - t_{sd}}{l} wnq\mu V \,, \qquad (5\text{-}1)$$

where t_{sd} is the space charge region width in the darkness, μ is the electron mobility, V is the applied voltage, and q is the electron charge. Illumination with a light of proper wavelength will generate photocarriers. The photocarriers will separate as holes, which are captured by the surface states, and electrons, staying at the bulk film regions. This will change the amount of surface charge and therefore space charge region width (shown in Figure 5-1). The photocurrent, in general, depends on both the conductive volume and the carrier density, and can be expressed as follows,

$$I_{ph} = \frac{t - t_{si}}{l} w(n + dn)q\mu V \,, \qquad (5\text{-}2)$$

where t_{si} is the space charge region width under illumination. The amount of current change under illumination is, in general, expressed as follows,

$$\Delta I = I_{ph} - I_d = \frac{t - t_{si}}{l} \mathrm{wnq}\mu(\frac{\mathrm{dt_s}}{\mathrm{t - t_{si}}} + \frac{dn}{n})V \,, \qquad (5\text{-}3)$$

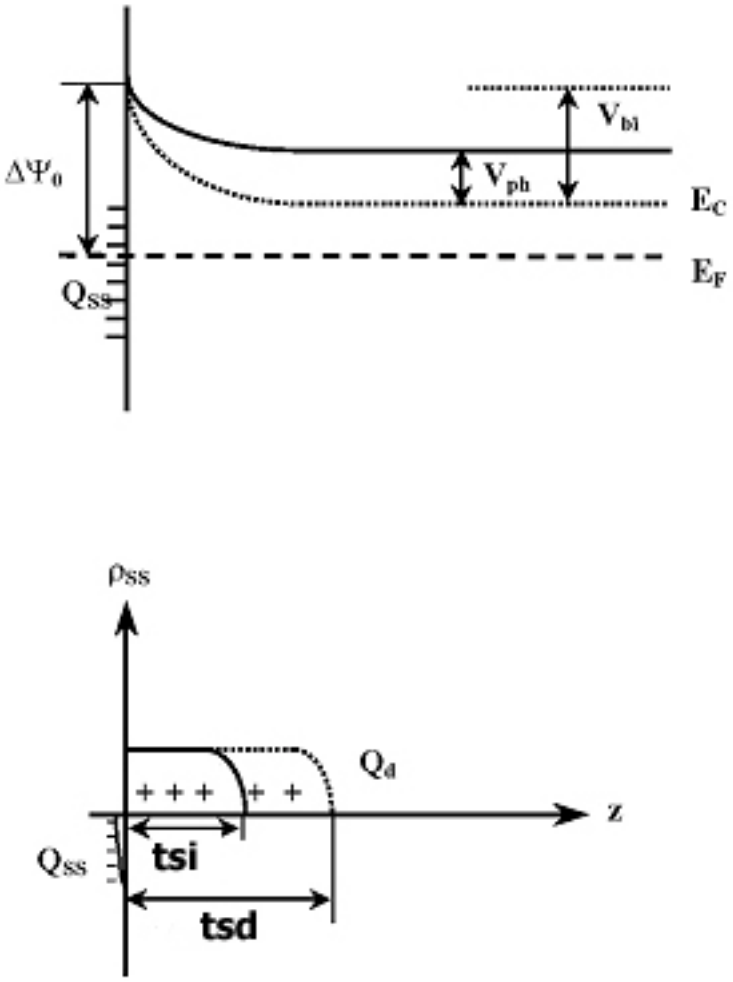

Figure 5.1 Energy-band and charge density associated with a negative charged semiconductor surface in the dark (dashed line) and under illumination (solid line).

This formula basically tells that there are two components contributing to current increase, one from the conductive volume modulation ($(t_{sd}-t_{si})WnqμV/l$) and the other from the carrier modulation ($(t-t_{si})dnWqμV/l$). It is important to mention that a photocurrent I_{ph} is expected to be significantly larger than a dark current I_d for practical operation of a photodetector (i.e. for high signal-to-noise ratio). This condition ($I_{ph}>>I_d$) can be translated into the following condition,

$$1+\frac{dn}{n}>>1-\frac{dt_s}{t-t_{si}}. \qquad (5\text{-}4)$$

It should be noted that $0 \le dt_s/(t-t_{si}) \le 1$. It is interesting to note that this condition can be satisfied at least by the following two cases, each corresponding to a situation dominated by either conductive volume modulation or carrier modulation.

Case 1: $\frac{dt_s}{t-t_{si}} \approx 1$ and $\frac{dn}{n} << 1$

This case corresponds to a situation that the entire film thickness is completely depleted by the surface charge in the darkness. The current is expressed as follows by dropping the carrier modulation terms of equation 5-3,

$$\Delta I = \frac{1}{l}\text{wnq}\mu V dt_s. \qquad (5\text{-}5)$$

Case 2: $\frac{dn}{n} >> 1$.

This case corresponding to a strong modulation of carriers, and the current increment can be expressed as follows by dropping the conductive volume modulation term of equation 5-3,

$$\Delta I = \frac{t - t_{si}}{l} \text{wnq}\mu V dn . \qquad (5\text{-}6)$$

Under steady illumination the photogenerated carriers can be expressed as follows using an effective carrier lifetime τ_r,

$$dn = \eta \frac{P}{h\nu} \tau_r . \qquad (5\text{-}7)$$

Combining equation 5-2 and 5-3, and introducing the carrier transit time τ_t,

$$\tau_t = \frac{l^2}{\mu V} . \qquad (5\text{-}8)$$

The current can be expressed as

$$\Delta I = q\eta \frac{P}{h\nu} G , \qquad (5\text{-}9)$$

where the photoconductive gain G is defined as

$$G = \frac{\tau_r}{\tau_t} . \qquad (5\text{-}10)$$

If we assume the conductive volume modulation is much less than the carrier modulation and also that the carrier mobility (and therefore the carrier transit time) maintains nearly the same level under different illumination power, this power dependence of gain (and responsivity) observed in this work can then be ascribed to a strong dependence of the effective carrier lifetime on the illumination power.

The responsivity is defined as

$$\Re = \frac{\Delta I}{P}. \qquad (5\text{-}11)$$

The relationship of the responsivity and the gain is then described by

$$G = \Re \frac{h\nu}{\eta q} = \Re \eta \frac{1.24}{\lambda_0}. \qquad (5\text{-}12)$$

Undoped ZnO usually shows n-type conductivity mainly ascribed to the non-stoichiometric defects such as oxygen vacancies and/or Zn intersititials. Considering the surface states on the film surface are chemisorption induced acceptor-like states, a negative surface charge would form near the film surface and therefore band bending occurs. The space charge region width in the dark (t_{sd}) is given by the surface charge density and the doping level through the following equation,

$$t_{sd} = \sqrt{\frac{2\varepsilon}{qNd} V_{bi}}, \qquad (5\text{-}13)$$

where V_{bi} is build-in potential in the dark.

Under UV illumination, the photocarriers are generated and the holes are swept to the depletion region and captured by the surface states. This results in the reduction of space charge region width. The space charge region width under illumination (t_{si}) is given by

$$t_{si} = \sqrt{\frac{2\varepsilon}{qNd}(V_{bi} - V_{ph})}. \qquad (5\text{-}14)$$

Besides the space charge width reduction, the carrier modulation would cause a certain amount of band bending change. The amount of bending change is expressed as follows

$$V_{ph} = V_T \ln[1 + e^{\Delta\Psi_0 / V_T}(q\eta \frac{P}{h\nu AT^2})], \qquad (5\text{-}15)$$

where V_T in the thermal voltage, equal to kT/q, $\Delta\Psi_0$ is the energy gap between Fermi level and the bottom of the conductance band at the surface, and A is the Richardson constant. This equation is derived from the following understanding. In the dark, two opposite electron fluxes exist over the barrier, namely the thermionic emission from the surface states towards the n-type ZnO bulk film and a compensating flux from the ZnO bulk film towards the surface states. Under the constant illumination, the photogenerated carriers reduce the band bending by V_{ph}, and this allows an electron flux reaching the surface equal to the holes arriving by drift and equal to the photocarriers generated. The lifetime of carrier electron is inversely proportional to the electron concentration available at the surface, and is expressed as follows,

$$\tau_r \propto e^{-\frac{V_{ph}}{V_T}}. \qquad (5\text{-}16)$$

Substituting equation 5-15 into equation 5-16, the lifetime can be expressed as follows

$$\tau_r = \tau_0[1 + e^{\frac{\Delta\Psi_0}{V_T}}(\frac{\eta qP}{h\nu AT^2})]^{-1}, \qquad (5\text{-}17)$$

where τ_0 is the effective carrier lifetime in the dark.

From this, the power dependence of gain (and the responsivity) can be understood.

5.2 Dynamic Behavior

The photoconductor's dynamic behavior can be understood analogous to a metal-semiconductor (n-type) Schottky contact. In the dark, two opposite electron fluxes exist over the barrier, namely thermionic emission from the surface states towards the bulk semiconductor and a compensating flux from the semiconductor towards the surface states. As a first approximation we neglect the effect of the tunneling currents. Therefore, to model the time evolution of the accumulated charge at the surface, we take into account two competing processes, the electron thermionic emission from the surface states and the thermionic capture over the barrier of electrons from the bulk. The dynamic equation of the accumulated charge can be expressed as

$$\frac{dQ_{SS}(t)}{dt} = J_{cap} - J_{emiss} = AT^2 e^{-\Delta\Psi_0 / V_T}(e^{V_{ph}(t)/V_T} - 1), \qquad (5\text{-}18)$$

where

$$V_{ph}(t) = \Delta\Psi_0 - \frac{{Q_{SS}}^2(t)}{2q\varepsilon N_d}.$$

The surface states of ZnO epilayer are assumed to be induced by oxygen adsorption on the surface. The effect of chemisorption of ZnO on the dynamic behavior of the photoconducotor should be considered. Two-step process was proposed for oxygen chemisorption.[82] Physisorption or collision of oxygen molecules with the surface to form the weak chmisorption states is the first step. The capture of electrons by the oxygen molecules to form strong chemisorption states is the second step. A thermal activation is associated with the first step, which is also dependent on the pressure of the gas ambient.[83] It is the energy required to excite the physisorbed molecules or the molecules striking the surface into weak chemisorption states. The term $exp(-E_A/kT)$ representing the probability of such excitation is added to equation, and also the term $Cp_{O_2}^m$, which represents the gas ambient effect, then obtained

$$\frac{dQ_{SS}(t)}{dt} = J_{cap} - J_{emiss} = AT^2 e^{-\Delta\Psi_0/V_T}(e^{V_{ph}(t)/V_T} - 1)(Cp_{O_2}^m e^{-E_A/V_T}), \qquad (5\text{-}19)$$

where C and m are the constants, dependent on temperature, E_A is activation energy.

5.3 Results and Discussion

5.3.1 Responsivity Dependence on the Power Density

Responsivity of the photoconductors consists of two contributions, one is from the conductive volume modulation and the other is from the carrier modulation. Which one is main part depends on several parameters, carrier concentration of the film, N_d, initial surface potential, $\Delta\Psi_0$, and effective carrier lifetime in the dark, τ_0. Figure 5-2, 3, 4 shows the calculated responsivity as a function of carrier concentration under different initial surface potentials. Solid line represents the total responsivity, dashed line is contribution from the conductive volume modulation and dotted line from the carrier modulation. In this calculation the power is fixed at 0.01 W/cm^2 and τ_0 is 10^{-6}s and film thickness is 1.0 μm. In Figures 5-2, $\Delta\Psi_0$ is in low value regime, 0.5 V. The responsivity is predominately contributed by the carrier modulation in almost all calculated N_d range and the responsivity is low. The contribution of conductive volume modulation is negligible as the width of space charge region is negligible compared with the film thickness. In Figures 5-3, $\Delta\Psi_0$ is in high value regime, 0.7 V. The responsivity is predominately contributed by the conductive volume modulation in almost all calculated N_d range and the responsivity is high. The contribution of carrier modulation is negligible as the excess carrier concentration is negligible compared with the film carrier concentration. In the regime between them, 0.6 V (Figure 5-4), The two contributions must be included to account for the total responsivity.

Figure 5-5, 6, 7 shows the calculated responsivity as a function of surface potential $\Delta\Psi_0$. Solid line represents the total responsivity, dashed line is contribution from the conductive volume modulation and dotted line from the carrier modulation. In this calculation the power is fixed at 0.01 W/cm^2 and N_d is 10^{17}/cm^3 and film thickness is 1.0 μm. In Figures 5-5, τ_0 is 10^{-6} s.

The responsivity is predominately contributed by the conductive volume modulation in almost all calculated $\Delta\Psi_0$ range. The contribution of carrier modulation is negligible as excess lifetime is short and excess carrier concentration is negligible compared with the film carrier concentration. In Figures 5-6, τ_0 is 1 s. The responsivity is predominately contributed by the carrier modulation when $\Delta\Psi_0$ < 0.8V. The contribution of conductive volume modulation is negligible as the width of space charge region is negligible compared with the film thickness. When $\Delta\Psi_0$ > 0.9V, the conductive volume modulation becomes dominant as the width of space charge region is significant compared with the film thickness. In the regime between them, τ_0 is 0.01 s (Figure 5-7), The two contributions must be included to account for the total responsivity, but the $\Delta\Psi_0$ range is very small, therefore in this case, the responsivity can be represented either by conductive volume modulation or carrier modulation in a wide $\Delta\Psi_0$ range.

The responsivity dependence on the illumination power density is also calculated. Figure 5-8 shows the responsivity as a function of power density at various film carrier concentrations. With the increase of film carrier concentration, the effect of film carrier concentration on responsivity becomes smaller. As $\Delta\Psi_0$ is 0.6 V in low value regime, the carrier modulation is dominant. With the increase of film carrier concentration, the carrier modulation effect becomes smaller. The flat responsivity region that appears at extremely low power is due to low *Vph* developed in space charge region, the lifetime of the excess carrier is long, and the excess carrier concentration is high.

Figure 5-9 shows the responsivity as a function of power density at various initial surface potential. The characteristics have an obvious difference when the initial surface potential increases. This is due to the transition from carrier modulation dominance to conductive volume modulation dominance.

Figure 5-10 shows the responsivity as a function of effective carrier lifetime in the dark. With the increase of effective carrier life time the excess carrier concentration increases and the modulation effect becomes large and the responsivity increases.

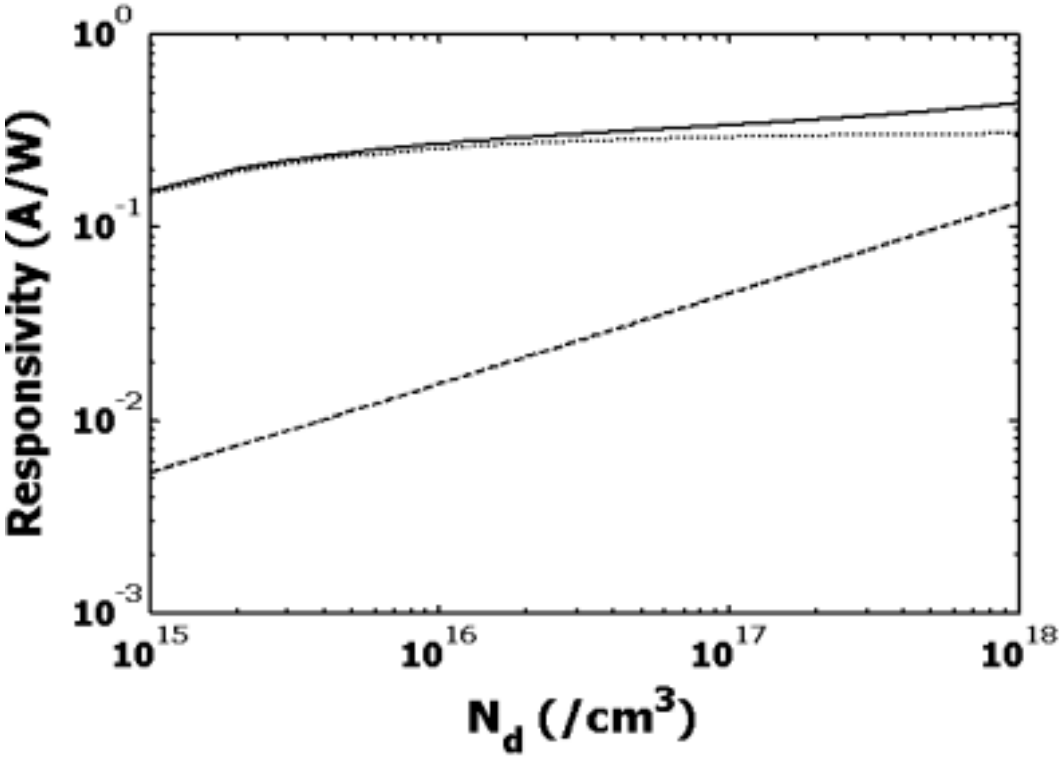

Figure 5.2 Responsivity as a function of film carrier concentration (dashed line from conductive volume modulation, dotted line from carrier modulation). $\Delta\Psi_0$ = 0.5 V.

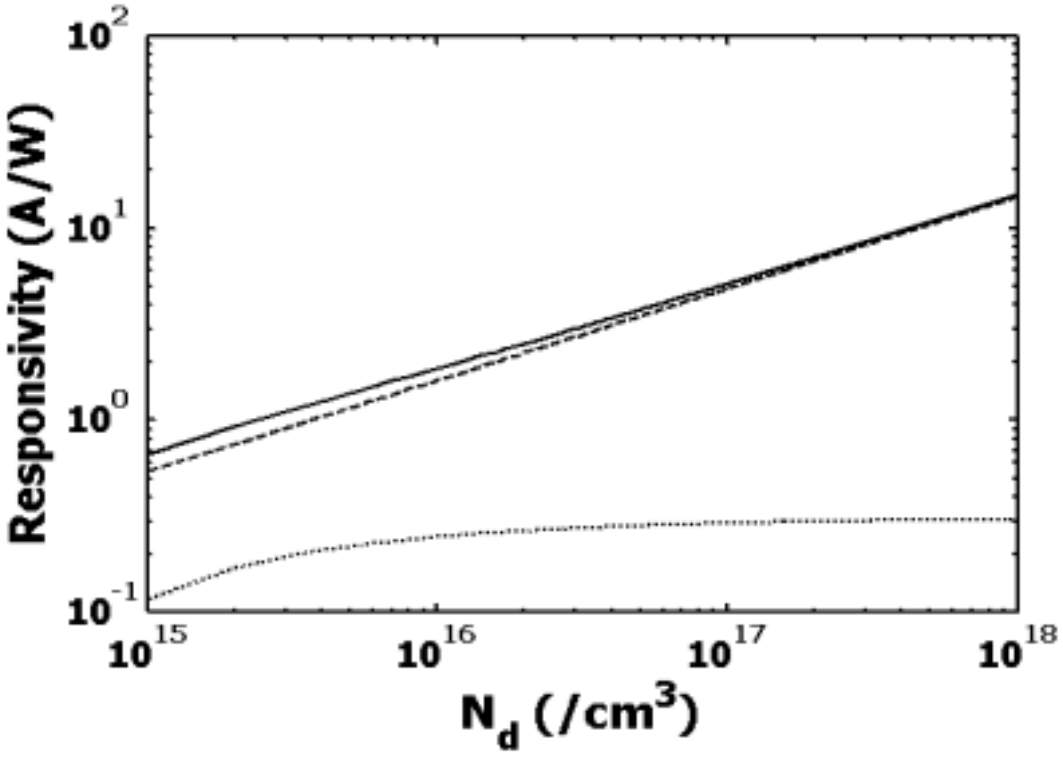

Figure 5.3 Responsivity as a function of film carrier concentration (dashed line from conductive volume modulation, dotted line from carrier modulation). $\Delta\Psi_0$ = 0.7 V.

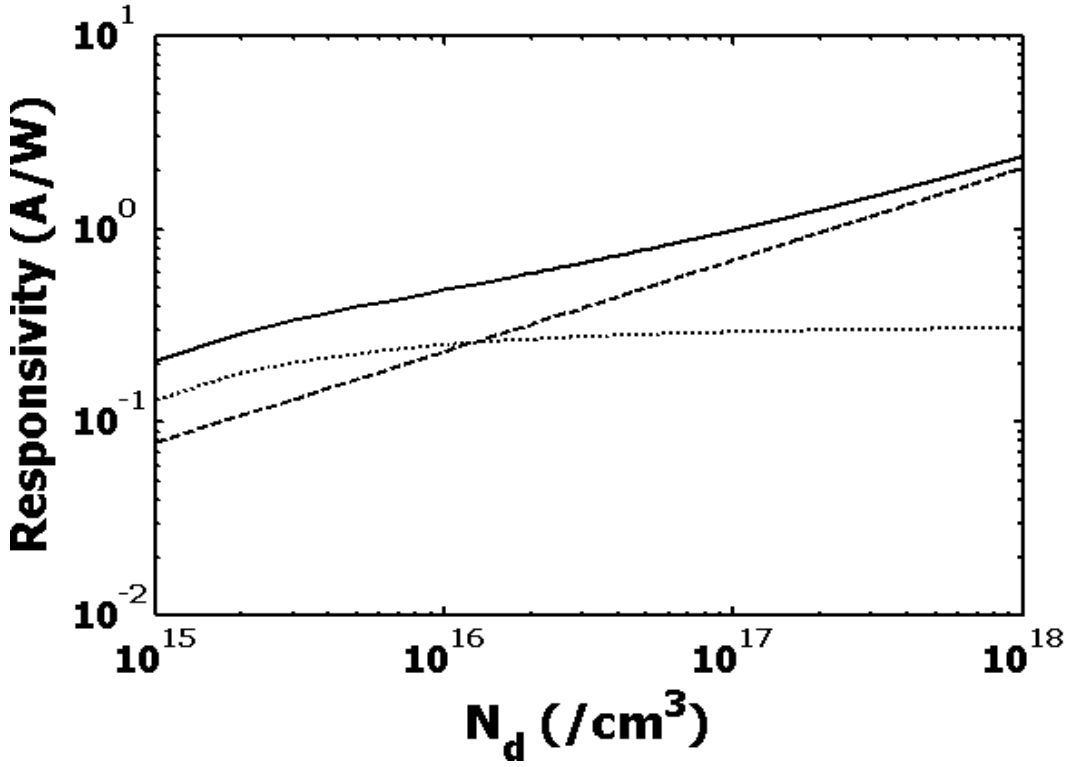

Figure 5.4 Responsivity as a function of film carrier concentration (dashed line from conductive volume modulation, dotted line from carrier modulation). $\Delta\Psi_0$ = 0.6 V.

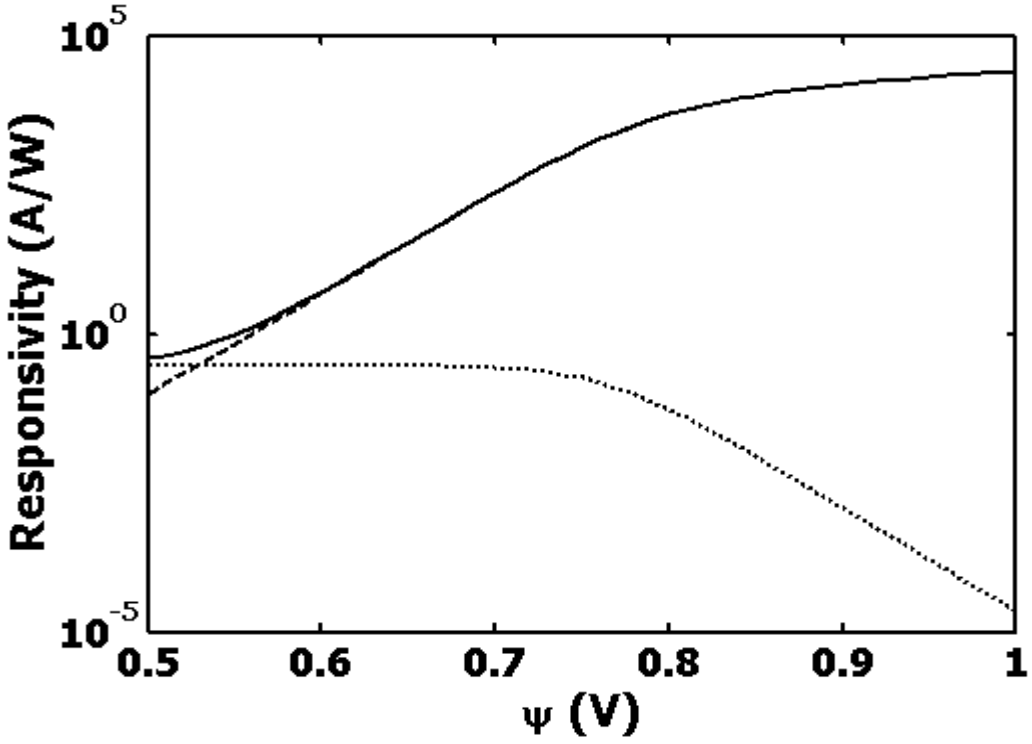

Figure 5.5 Responsivity as a function of film initial surface potential (dashed line from conductive volume modulation, dotted line from carrier modulation). $\tau_0 = 10^{-6}$ s.

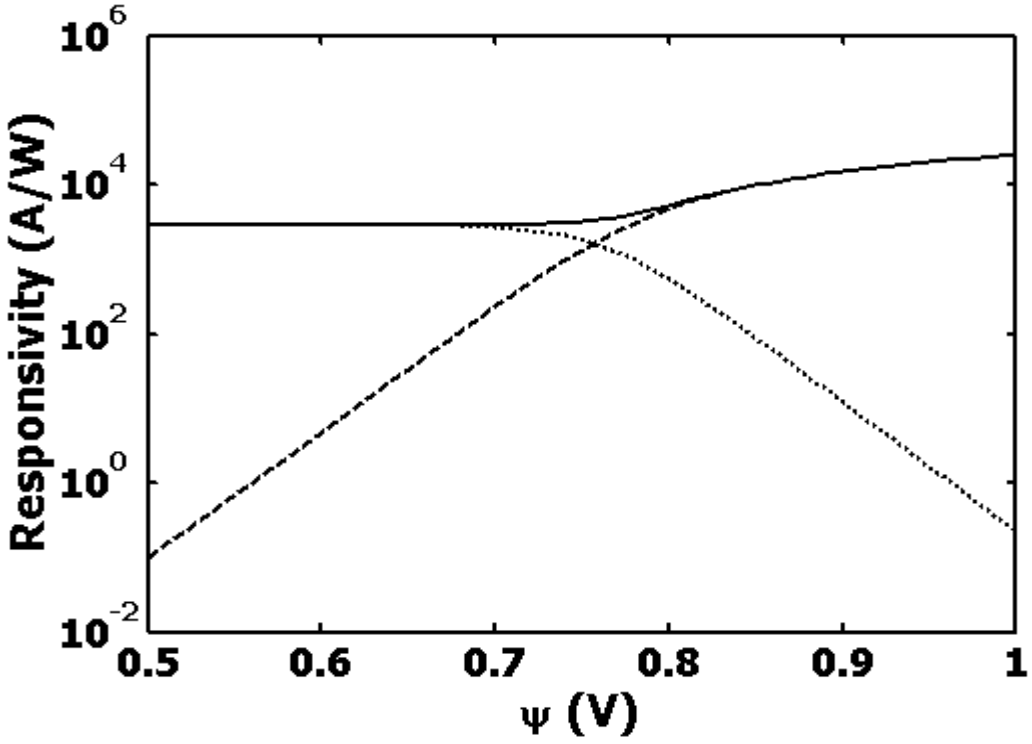

Figure 5.6 Responsivity as a function of film initial surface potential (dashed line from conductive volume modulation, dotted line from carrier modulation). τ_0 = 1 s.

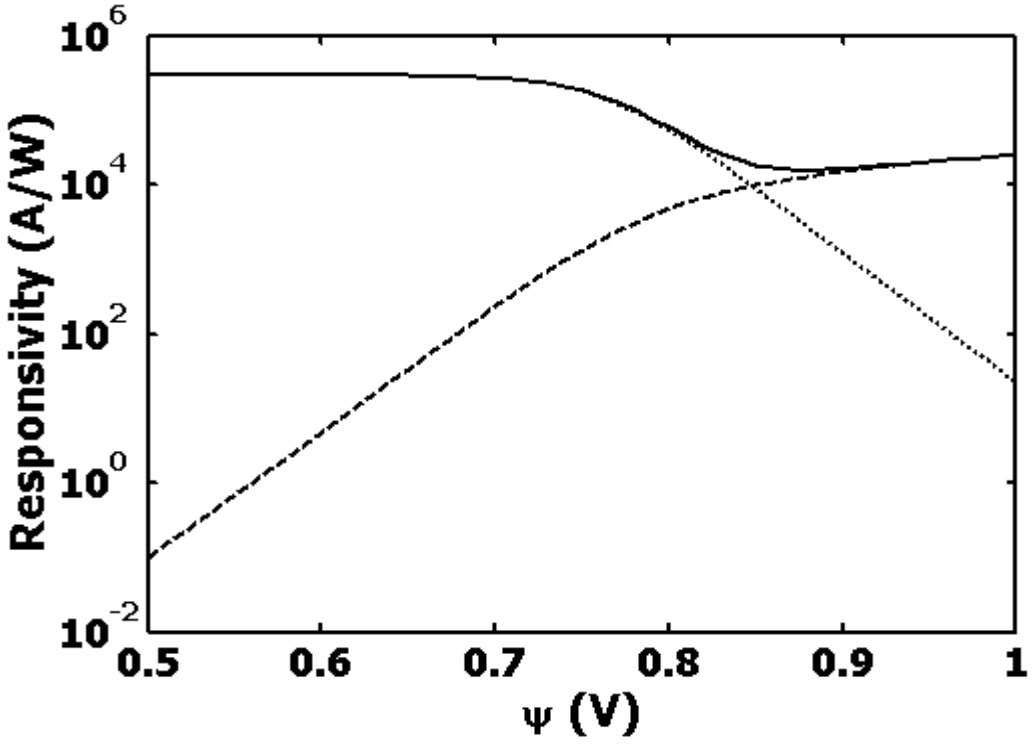

Figure 5.7 Responsivity as a function of film initial surface potential (dashed line from conductive volume modulation, dotted line from carrier modulation). $\tau_0 = 10^{-2}$ s.

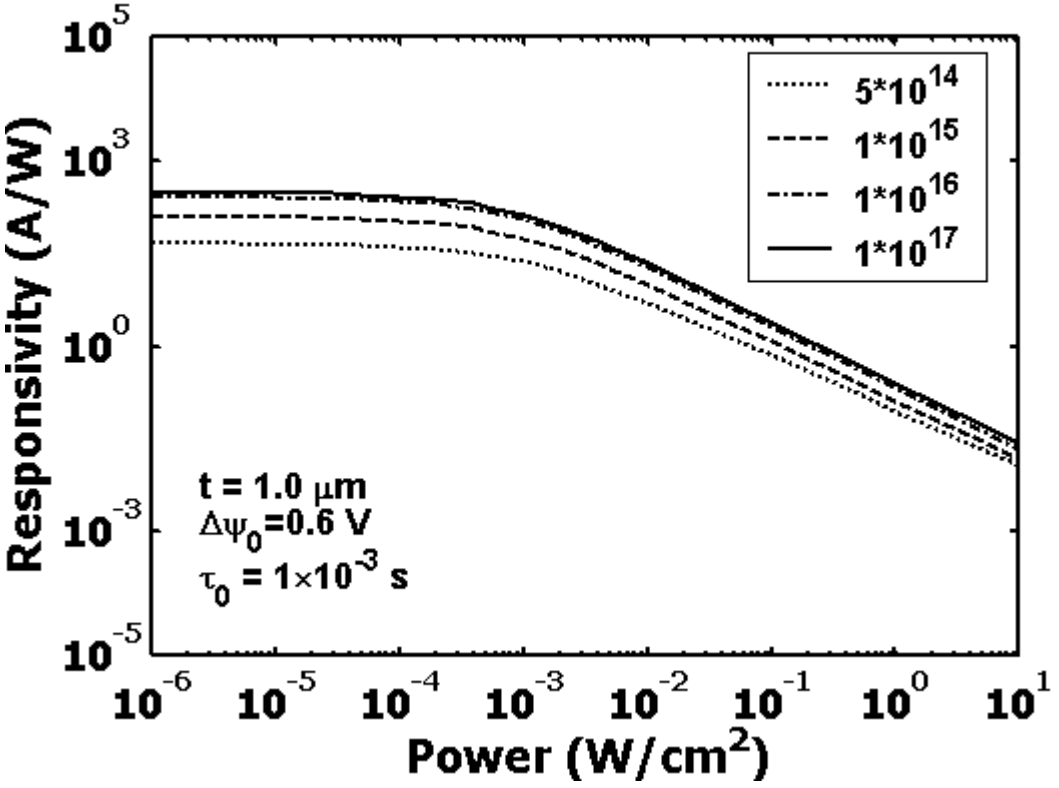

Figure 5.8 Responsivity as a function of power density at various film carrier concentration.

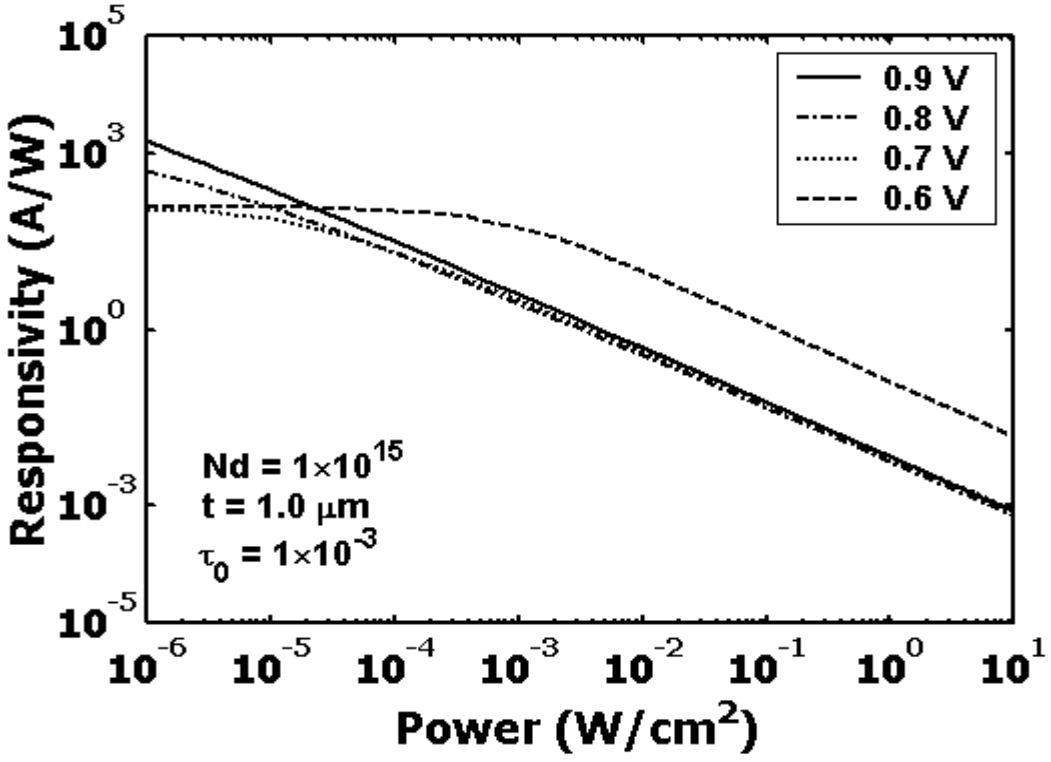

Figure 5.9 Responsivity as a function of power density at various surface potential.

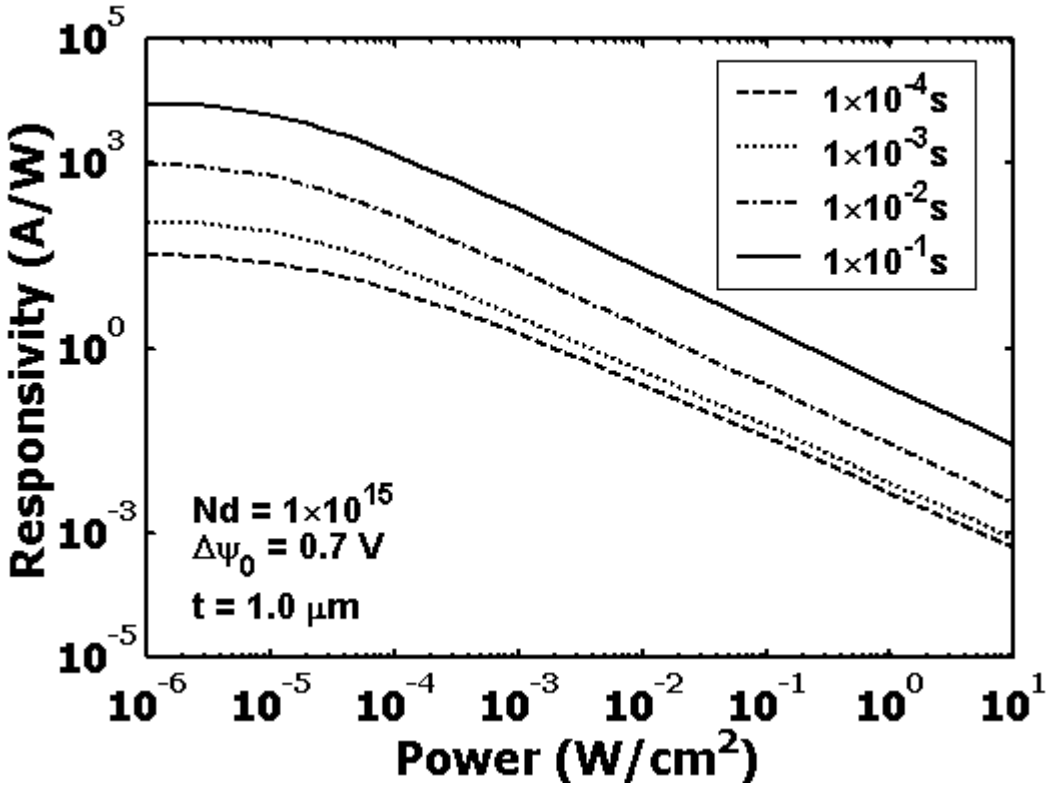

Figure 5.10 Responsivity as a function of power density at various effective carrier lifetime in the dark.

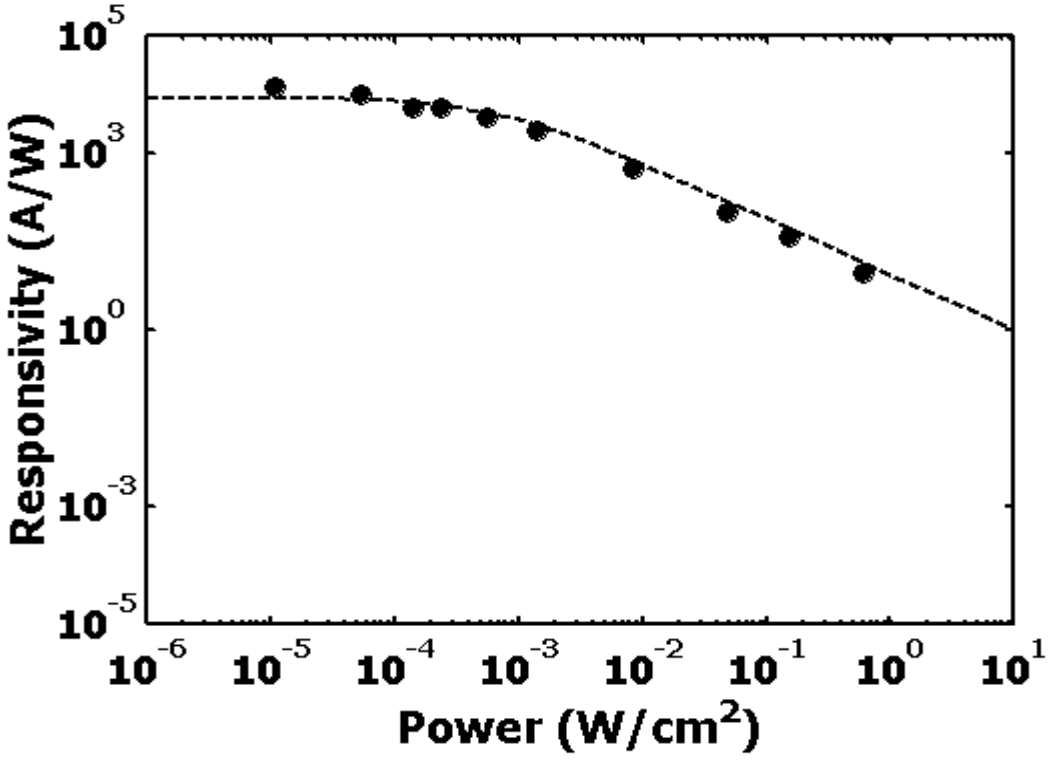

Figure 5.11 Responsivity as a function of power density of a ZnO photodetector with as-deposited ZnO epilayer and film thickness 0.5 μm. Solid dots represent experimental data, dashed line is the fitting curve.

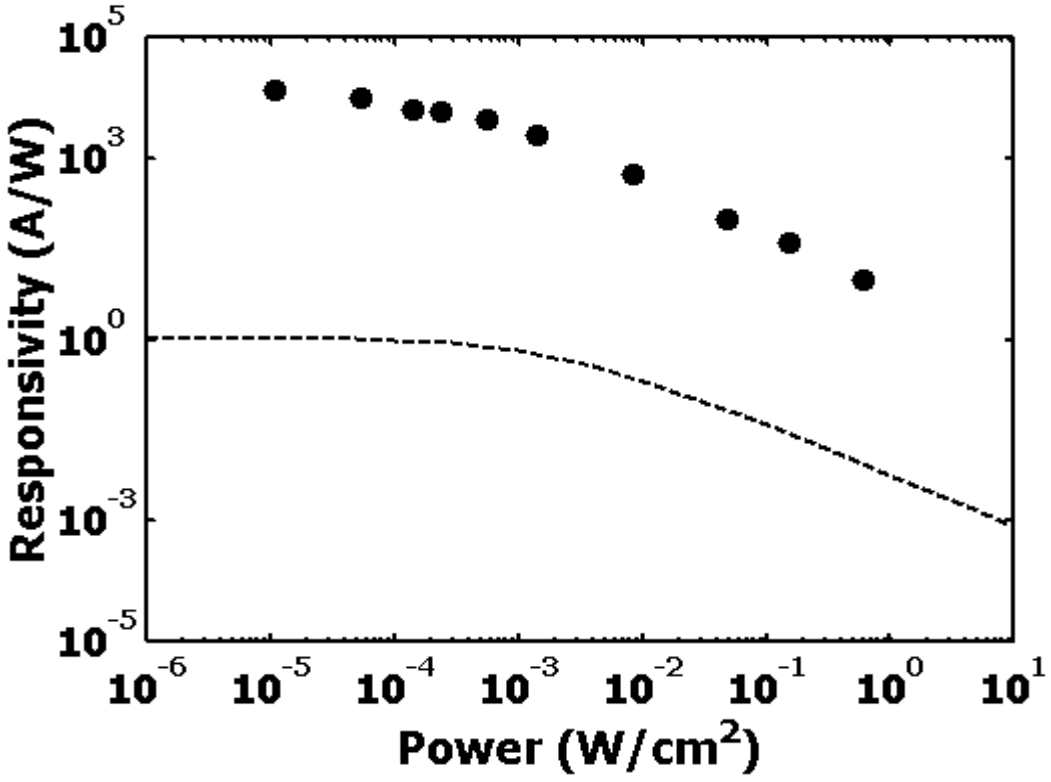

Figure 5.12 Responsivity as a function of power density of a ZnO photodetector with with as-deposited ZnO epilayer and film thickness 0.5 μm. Dashed line represents the conductive volume modulation contribution in Figure 5-11.

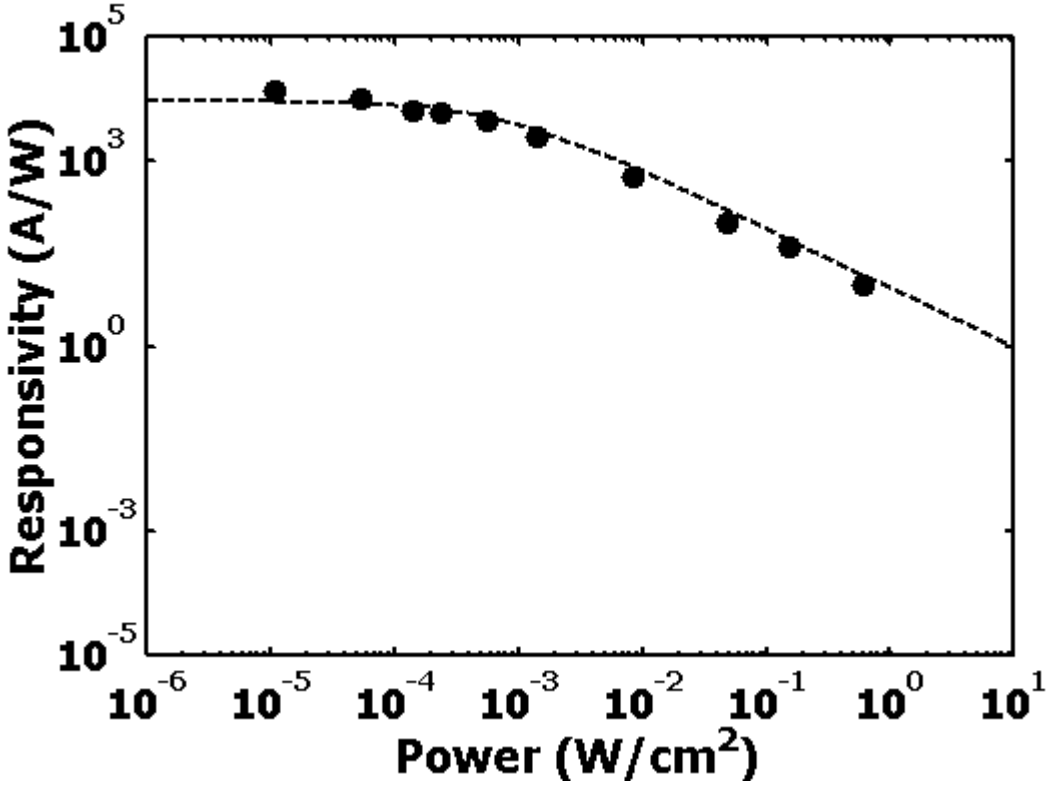

Figure 5.13 Responsivity as a function of power density of a ZnO photodetector with as-deposited ZnO epilayer and film thickness 0.5 μm. Dashed line represents the carrier modulation contribution in Figure 5-11.

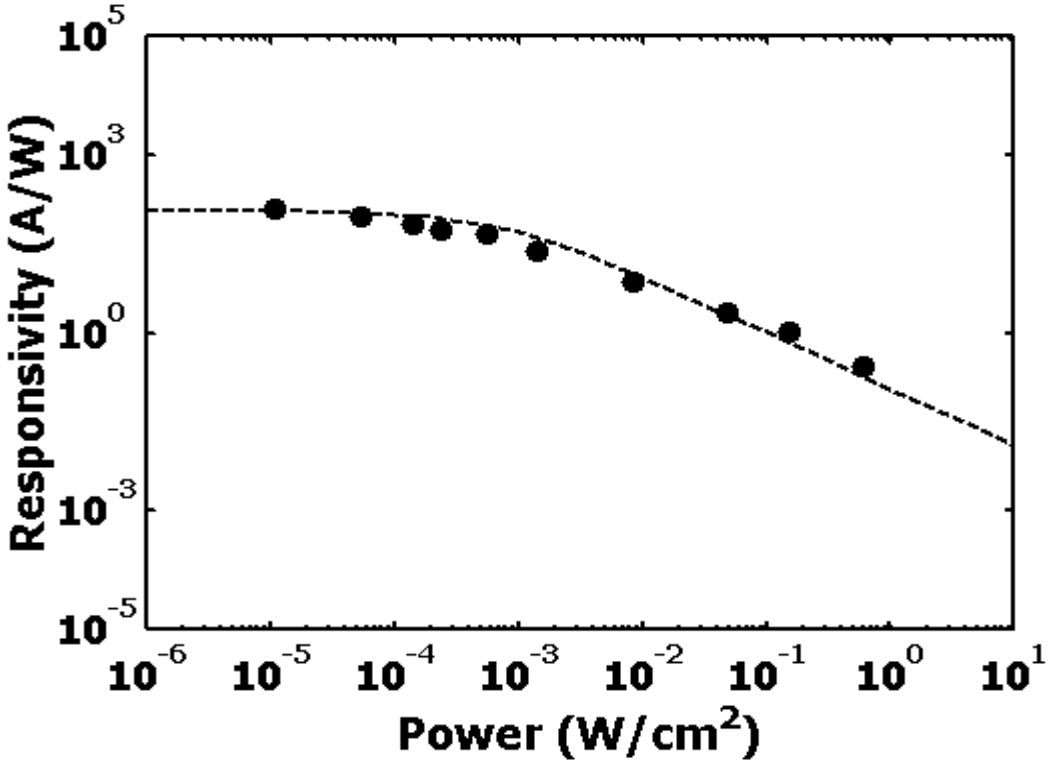

Figure 5.14 Responsivity as a function of power density of a ZnO photodetector with oxygen plasma treated ZnO epilayer and film thickness 0.5 μm (same as Figure 5-11). Solid dots represent experimental data, dashed line is the fitting curve.

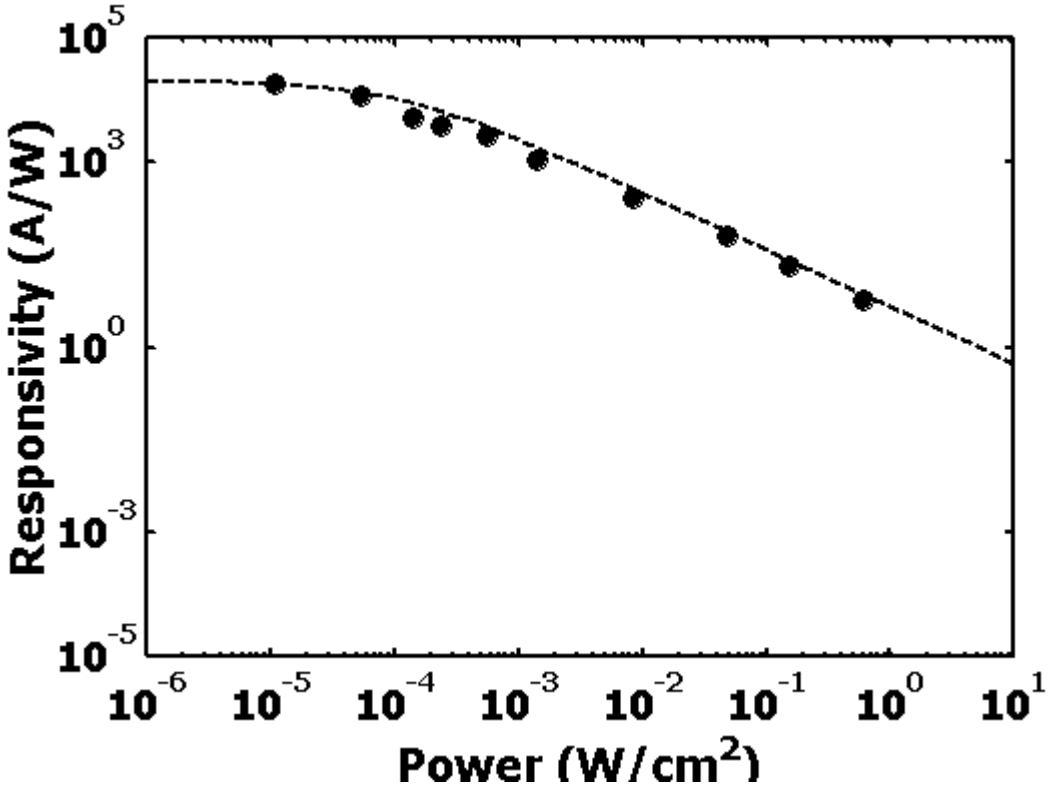

Figure 5.15 Responsivity as a function of power density of a ZnO photodetector with as-deposited ZnO epilayer and film thickness 0.02 μm. Solid dots represent experimental data, dashed line is the fitting curve.

With this model, the experimental data can be well fitted. Figure 5-11, 12, 13 is responsivity as a function of power density of a ZnO photodetector with as-deposited ZnO epilayer and film thickness 0.5 μm, carrier concentration $5\times10^{15}/cm^3$. In Figure 5-11, the measured data is fitted with parameters, $\Delta\Psi_0$ = 0.65 V, τ_0 = 0.1s. Figure 5-12 is contribution from conductive volume modulation. Figure 5-13 is contribution from carrier modulation. It indicates that the device is carrier modulation dominant and the conductive volume modulation is negligible.

Figure 5-14 and Figure 5-15 show another two detectors. They are also carrier modulation dominant. In the Figure 5-14, ZnO film was treated with oxygen plasma, others are the same as those of Figure 5-11. The experimental data was fitted with parameters: $\Delta\Psi_0$ = 0.6 V, τ_0 = 0.01s. It indicates that after oxygen plasma treatment, the initial surface potential was reduced, which means the chemisorption was alleviated. The effective carrier lifetime is also reduced, which is consistent with photoresponse measurement result. These extracted parameters will be used to fit the transient measurement results of the detectors.

Figure 5-15 is responsivity as a function of power density of a ZnO photodetector with as-deposited ZnO epilayer and film thickness 0.02μm, carrier concentration 2×10^{18}. In the Figure, the measured data is fitted with parameters, $\Delta\Psi_0$ = 0.72 V, τ_0 = 1 s. It indicates that after the film carrier concentration increases about three orders, the surface potential increases about 0.07 V. This result is consistent with Wolkenstein's isotherm predication discussed in section 3. The surface band bending increases by $2.3kT$ when the doping level increases by two orders of magnitude.[84]

5.3.2 Photoresponse of ZnO Photoconductors

In equation 5-19, Ea = 0.7V, m is 0.23.[85] To determine the value C, we assume that in the oxygen ambient when the pressure is larger than the pressure, in which the oxygen

chemisorption is saturate, the photoresponse is independent of the pressure. In section 3, it shows that $\theta^0 >> \theta^-$, when $p_{O_2} = 1atm$. Without losing generality, C is assumed to be approximately equal to 1. Under these conditions, by solving equation 5-19, we calculated the photocurrent decay with time with various parameters. Figure 5-16 shows the photocurrent decay with time at different film carrier concentration (N_d) with parameters: initial photovoltage(V_{ph0}), 0.4 V; initial surface potential($\Delta\Psi_0$), 0.6 V; film thickness 1.0 μm. As carrier concentration increases, the width of space charge region decreases, the barrier slope increases and the excess carrier in the conductance band is hard to thermionically emit to the surface states.

Figure 5-17 shows the photocurrent decay with time at different initial surface potential ($\Delta\Psi_0$) with parameters: initial photovoltage (V_{ph0}), 0.4 V; film thickness (t), 1.0 μm; film carrier concentration, $10^{16}/cm^3$. As initial surface potential ($\Delta\Psi_0$) increases, the initial barrier of the excess carrier in the conductance band is high and hard to thermionically emit to the surface states, resulting in slower photocurrent decay.

Figure 5-18 shows the photocurrent decay with time at different initial photovoltage (V_{ph0}) with parameters: initial surface potential ($\Delta\Psi_0$), 0.6 V; film thickness (t), 1.0 μm; film carrier concentration, $10^{16}/cm^3$. As initial photovoltage (V_{ph0}) increases, the initial barrier height of the excess carrier in the conductance band is low and easy to thermionically emit to the surface states, resulting in faster photocurrent decay.

Figure 5-19 shows the photocurrent decay with time at different film thickness (t) with parameters: initial surface potential ($\Delta\Psi_0$), 0.6 V; initial photovoltage (V_{ph0}), 0.4 V; film carrier concentration, $10^{16}/cm^3$. As the film thickness decreases, the excess carriers concentrate at small volume and more excess carriers distribute on high energy level, resulting in faster photocurrent decay. The film thickness effect is relatively weak and it decreases very fast with the increase of film thickness.

With the parameters extracted above, the measurement results were fitted with the model. In Figure 5-20, solid lines are measurement (performed in the air) results at different illumination power density of a ZnO photodetector with as-deposited ZnO epilayer and film thickness 0.5

μm. The dashed lines are fitting curves with fitting parameters: initial surface potential ($\Delta\Psi_0$), 0.65 V, initial photovoltage (V_{ph0}), 0.48 V, film carrier concentration, $5\times10^{15}/cm^3$; Ea = 0.65 V for low curve; for upper curve, initial photovoltage (V_{ph0}), 0.4 V, others the same.

In Figure 5-21, solid lines are measurement (performed in the air) results at different illumination power density of a ZnO photodetector with oxygen-plasma treated ZnO epilayer (same as that of Figure 15) and film thickness 0.5 μm. The dashed lines are fitting curves with fitting parameters: initial surface potential ($\Delta\Psi_0$), 0.6 V, initial photovoltage (V_{ph0}), 0.44 V, film carrier concentration, $5\times10^{15}/cm^3$, Ea = 0.65 V for low curve; for upper curve, initial photovoltage (V_{ph0}), 0.38V, others the same.

Comparing the two detectors shown in Figure 20&21, the only difference is the ZnO epilayers, In Figure 5-20, the film is the as deposited ZnO epilayer; in Figure 5-21, ZnO epilayer was oxygen plasma treated. The fitting results show that after oxygen plasma treatment the initial surface potential reduced. It indicates that the oxygen chemisorption on ZnO epilayer was alleviated by oxygen plasma treatment.

In Figure 5-22, solid lines are measurement results at different ambient, upper curve in the air (1atm), low curve in vacuum, 5×10^{-6} Torr, of a ZnO photodetector of as-deposited ZnO epilayer with film thickness 0.5 μm The dashed lines are fitting curves with fitting parameters: initial surface potential ($\Delta\Psi_0$), 0.65 V, initial photovoltage (V_{ph0}), 0.41 V; film carrier concentration, $5\times10^{15}/cm^3$, Ea = 0.65V, p_{O_2} = 200Torr for low curves; for upper curve, p_{O_2} = 5×10^{-6} Torr, others the same.

In the fitting curves, Ea = 0.65 V, which is approximate to the value in reference 83, 0.72V.

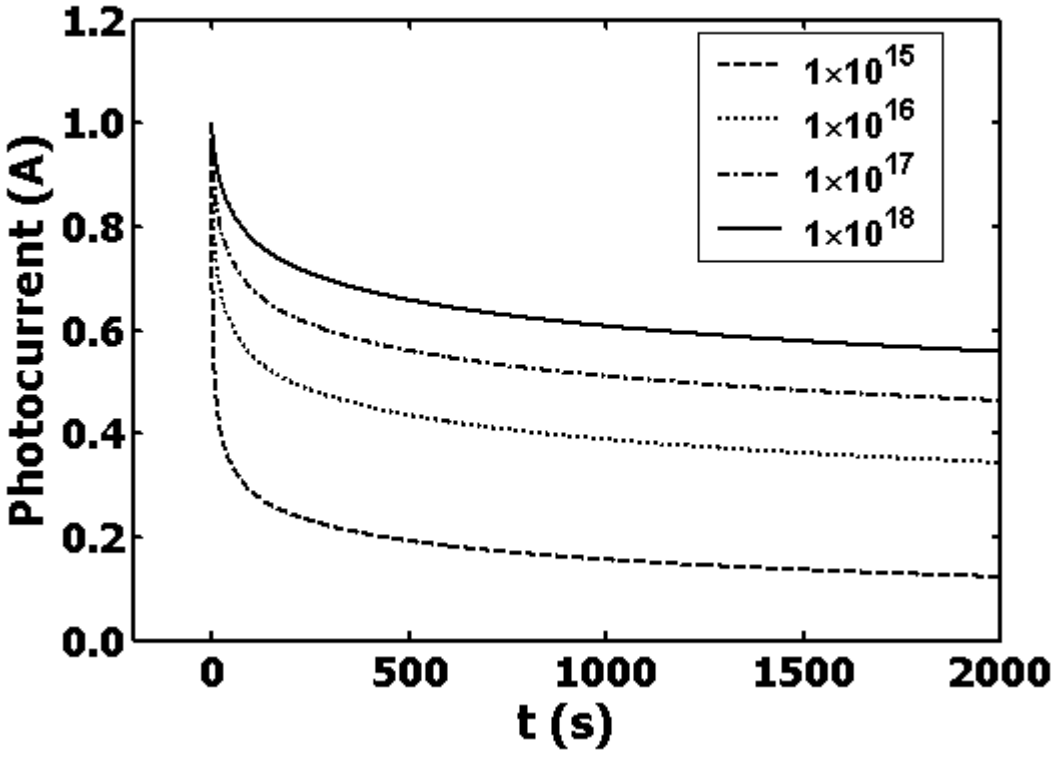

Figure 5.16 Photocurrent decay with various film carrier concentration.

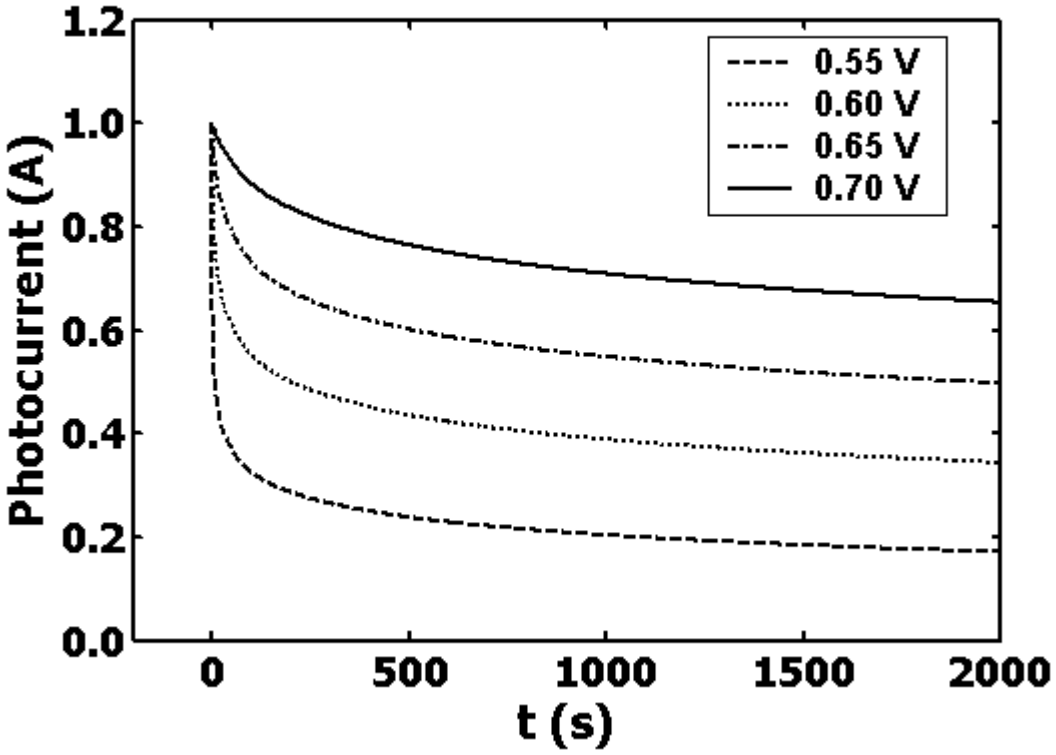

Figure 5.17 Photocurrent decay with various initial surface potential.

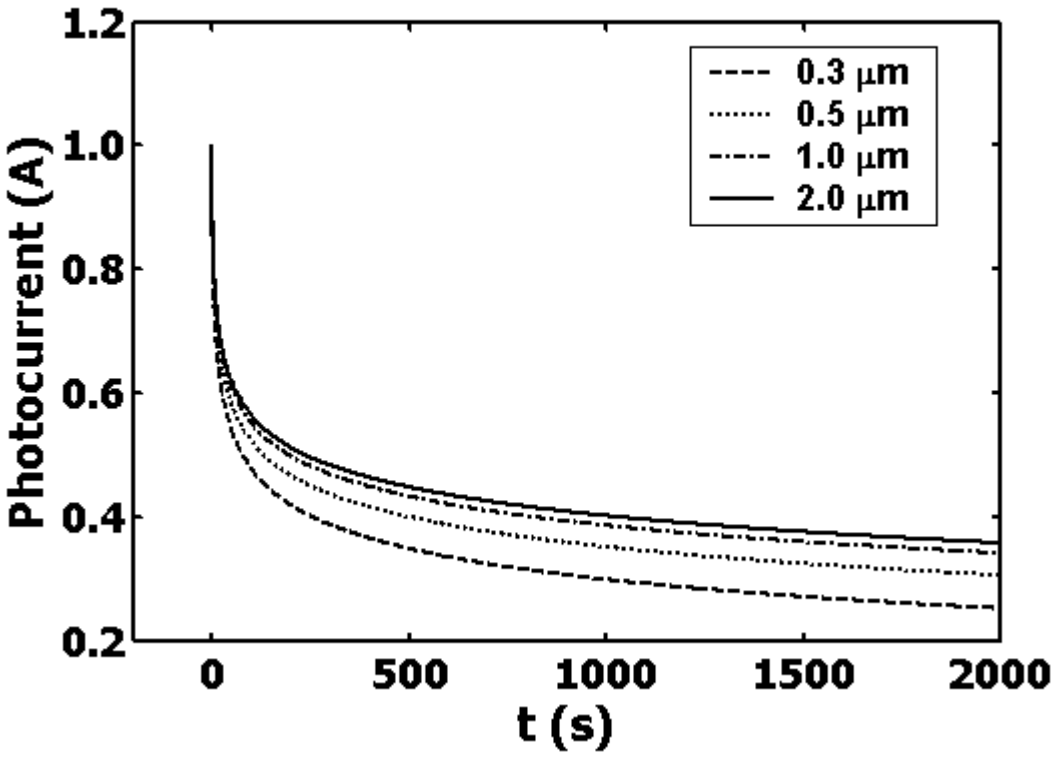

Figure 5.18 Photocurrent decay with various film carrier thickness.

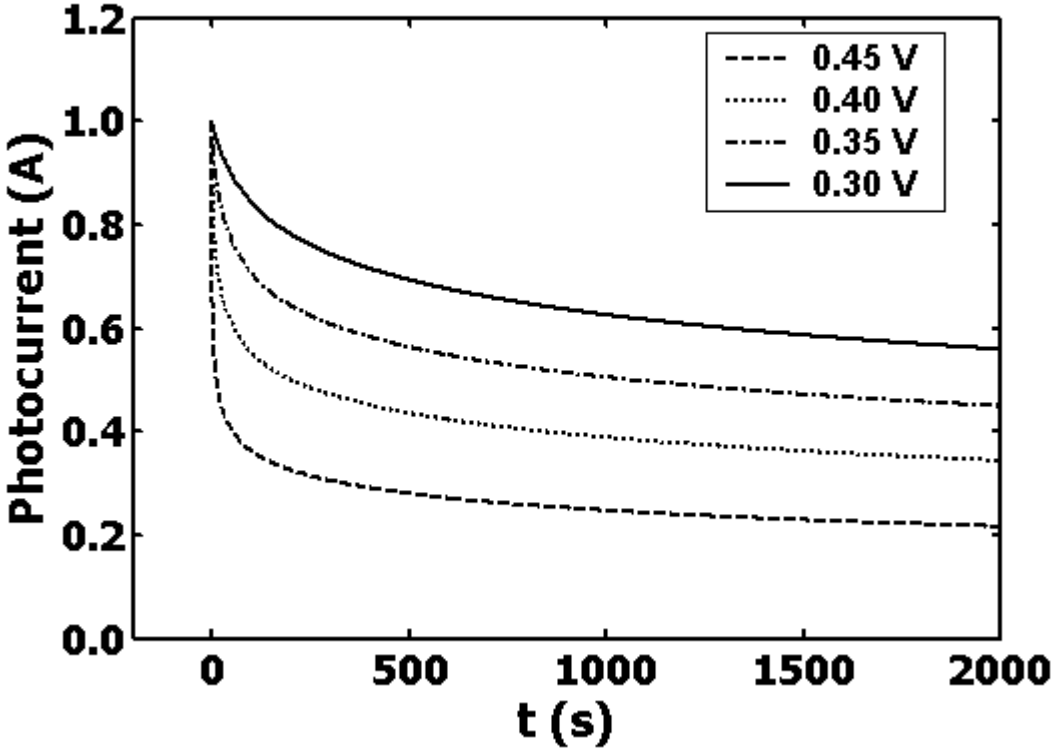

Figure 5.19 Photocurrent decay with various initial photovoltage.

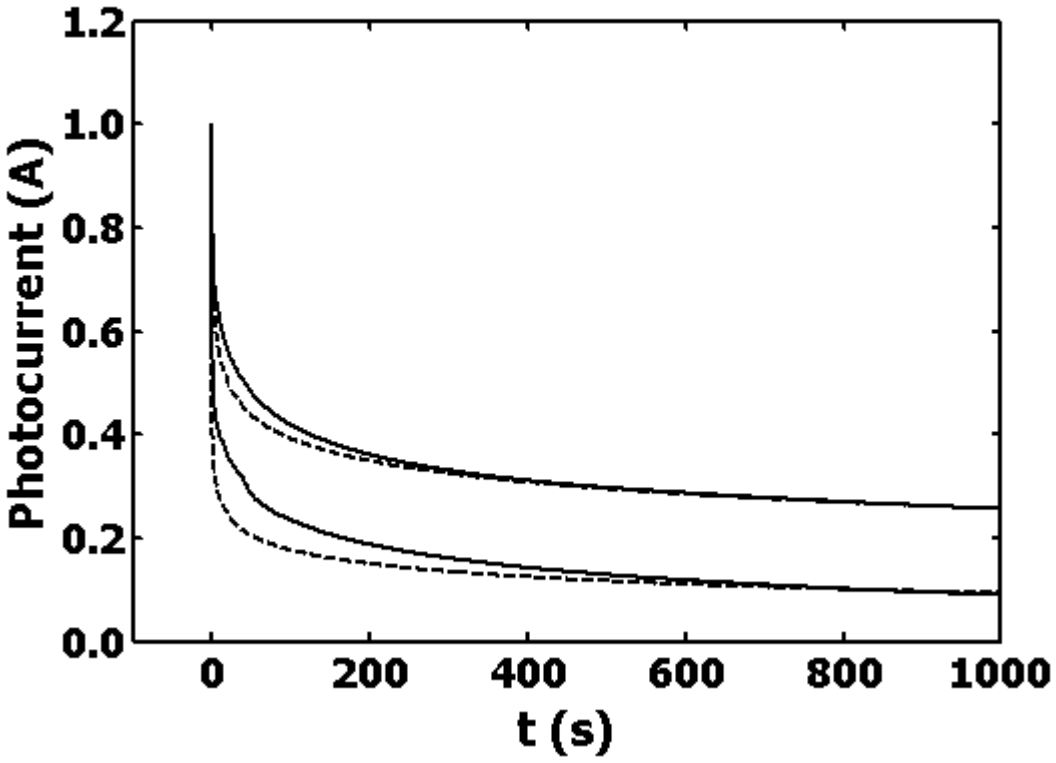

Figure 5.20 Photocurrent decay of a ZnO photodetector with as-deposited ZnO epilayer and film thickness 0.5 μm. Solid lines are measurement results under different intensity of He-Cd laser. Dashed lines are fitting curves with different initial photovoltage.

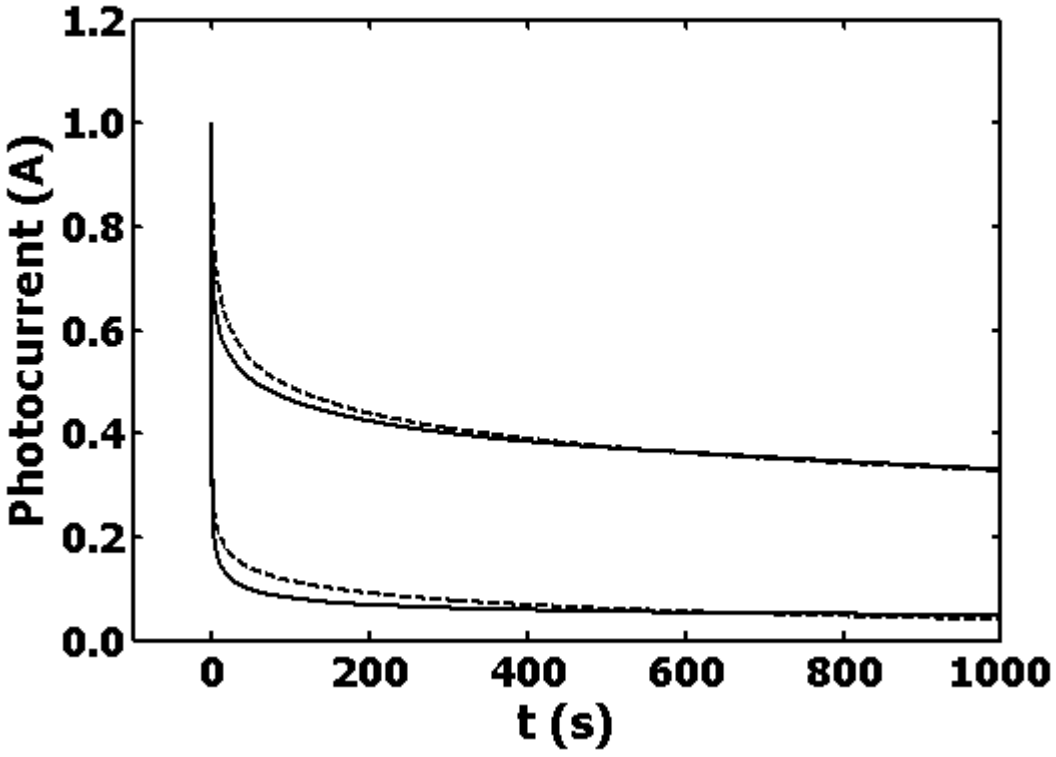

Figure 5.21 Photocurrent decay of a ZnO photodetector with oxygen plasma treated ZnO epilayer and film thickness 0.5 μm (same as Figure 5-20). Solid lines are measurement results under different intensity of He-Cd laser. Dashed lines are fitting curves with different initial photovoltage.

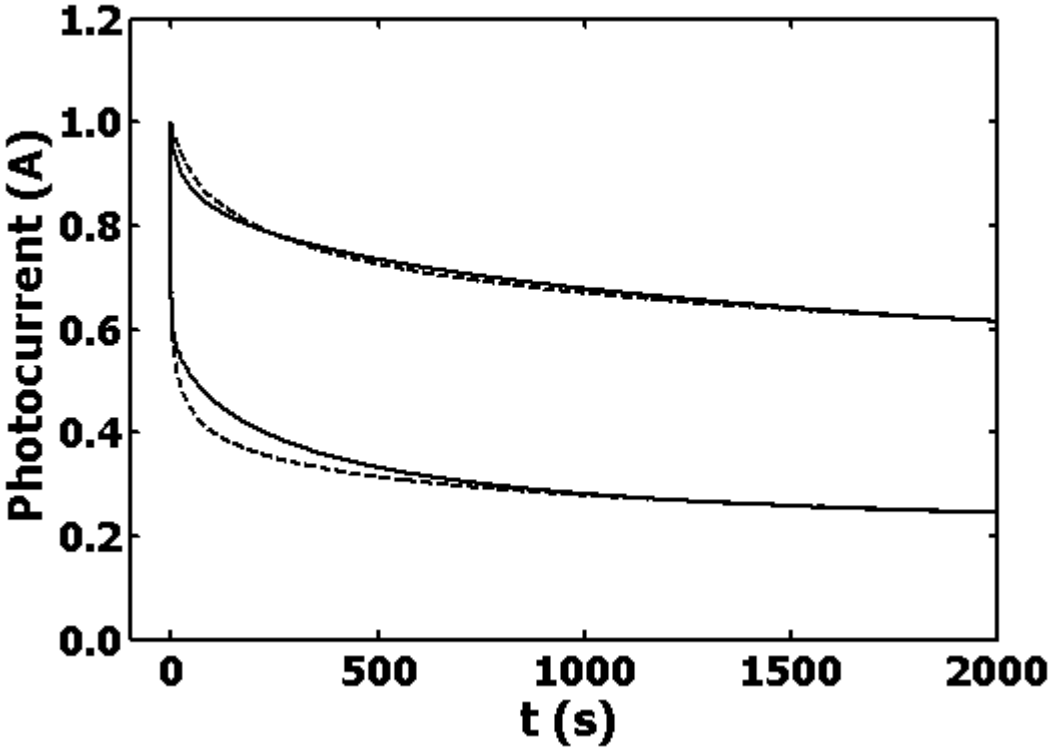

Figure 5.22 Photocurrent decay of a ZnO photodetector (same as Figure 5-20) with as-deposited ZnO epilayer and film thickness 0.5 μm. Solid lines are measurement result in the air (low curve) and in vacuum (5×10^{-6}, upper curve). Dashed lines are fitting curves with different pressure.

5.4 Conclusions

A model, based on modulation mechanism of the conductive volume and carriers, has been developed to explain the power dependence of the UV responsivity of ZnO photodetectors. In this model, the photocurrent decay process is analyzed with oxygen chemisorption and thermionic theory. The results suggest that the plasma treatment reduces the oxygen vacancy concentration at the surface and in the near-surface bulk of ZnO, which in turn reduces the surface band bending and therefore the chemisorption effects. Oxygen plasma treatment is considered an effective way of making nanometer-scale ZnO viable for high performance UV optoelectronic devices. The effects observed in this study are also expected to be observable in other low-dimensional structures of ZnO, such as quantum dots, nano wires and ribbons.

BIBLIOGRAPHY

BIBLIOGRAPHY

1. S. A. Studenikin, Nickolay Golego, and Michael Cocinera, J. Appl. Phys. 87, 2413 (2000)

2. D. C. Look, D. C. Reynolds, J. R. Sizelove, R. L. Jones, C. W. Litton, G. Cantwell, W. C. Harsch, Solid State Commun. 105, 399(1998)

3. D. C. Reynolds, D. C. Look, B. Jogai, C. W. Litton, T. C. Collins, W. Harsch, G. Cantwell, Phys. Rev. B57, 12151 (1998)

4. P. Fons, K. Iwata, A. Niti, A. Yamada, K. Matsubara, J. Crystal Growth, 210, 627 (1999)

5. J. Narayan, K. Dovidenko, A. K. Sharna, S. Oktyabrsky, J. Appl. Phys. 84, 2597 (1998)

6. Y. Liu, C. R. Gorla, S. Liang, N. Emanetoglu, Y.Lu, H. Shen, M. Wraback, J. Electron. Mater. 29, 69 (2000)

7. B. Haha, G. Heindel, E. Pschoor-Schoberer, W. Gebhardt, Semicond. Sci. Tech. 13, 788 (1998)

8. A.Ohtomo, M.Kawasaki, T. Koida, K. Masubuchi, H. Koinuma, Y. Sakurai, Y. Yasuda, Y. Segawa, Appl. Phys. Lett. 72, 2466 (1998)

9. Yefan Chen, D. M. Bagnall, H. J. Koh, K. T. Park, K. Hiraga, Z. Q. Zhu, T. Yao, J. Appl. Phys. 84, 3912 (1998)

10. M. S. Sherr, M. Asif Khan, "*Semiconductors and Semimetals*", 57, 407 (1999)

11. H. Morkoç, "*Nitride Semiconductors and Devices*", Springer (1998)

12. Chandrasekhar R. Gorla, "*Properties of ZnO Thin Films Grown on R-plane Al_2O_3 By Metal Organic Chemical Vapor Deposition*", PhD Thsis(1999)

13. J. P. Suchet, "*Chemical Physics of Semiconductors*", Van Nostrand, London, 1965

14. International Tables for X-ray Crystallography, vol. 1, The international Union of Crystallography, Kynoch Press, England, 1965

15. S. Nakamura, T. Mukai and M. Senoh, Appl. Phys. Lett. 64, 1687 (1994)

16. R. D. Vispute, V. Talyansky, S. Choopun, R. P. Sharma, T. Venkatesan, M. He, X. Tang, J. B. Halpern, M. G. Spencer, Y. X. Li, L. G. Salamanca-riba, A. a. Iliadi and K. A. Jones, Appl. Phys. Lett. 73, 348 (1998)

17. T. Detchprohm, K. Hiramatsu, H. Amano and I. Akasaki, Appl. Phys. Lett. 61, 2688 (1992)

18. M. H. Sukkar and H. L. Tuller, in Advances in Ceramics, edited by M. F. Yuan and A. H. Heuer (American Ceramics Society, Columbs, 1982), vol. 7, 71 (1982)

19. A.F. Kohan, G. Ceder, D. Morgan and Chris G. Van de Walle, Phys. Rev. B, 61, 15019 (2000)

20. W. Hirschwald, P. Bonasewicz, L. Ernst, M. Grade, D. Hofmann, A. Krebs, R. Littbarski, G. Neumann, M. Geunze, D. Kolb and H. J. Schulz in Current Topics in Materials Science, vol. 7, edited by E. Kaldis, North-Holland, 1981

21. G. Mandel, Phys. Rev. 134, S1073 (1964)

22. Semiconductors and Semimetals, II-VI Blue/Green Light Emitter: Device Physics and Epitaxical Growth, edited by R. L. Gunshor and A. V. Nurmikko, vol. 44, 122 (1997)

23. D. B. Laks, C. G. Van De Walle, G. F. Neumark and S. T. Pantelides, Phy. Rev Lett. 66, 648 (1991)

24. R. M. Park, M. B. Troffer, C. M. Rouleau, J. M. DePuydt and M. A. Haase, Appl. Phys. Lett. 57, 2127 (1990)

25. S. B. Zhang, A. H. Wei and Alex Zunger, Phys. Rev. B63, 075205 (2001)

26. K. L. Chopra, S. Major, D. K. Pandya, Thin Solid Films 102, 1(1983)

27. C. G. Van de Walle, Phys. Rev. Lett. 85, 1012 (2000)

28. M. Joseph, H. Tabata and T. Kawai, Jpn. J. Appl. Phys. 38, L166(1999)

29. T. Yamamoto and H, Katayama-Yoshida, Jpn. J. Appl. Phys. 38, L166 (1999)

30. Toru Aoki, and Yoshinori Hatanka, David C. Look, 76, 3257(2000)

31. Gang Xiong, John Wilkinson, Brian Mischuck, S. Tüzemen, K. B. Ucer, and R. T. Willams, Appl. Phys. Lett., 80, 1195 (2002)

32. Donald L. Smith, *Thin film deposition: principles and practice*, 143(1995), McGraw-Hill

33. Vitality A. Shchukin and Dieter Bimberg, Reviews of Modern Physics, vol. 71, No. 4, 1125(1999)

34. B. D. Cullity, *Elements of X-ray Diffraction*, 2nd edt., Addison-Wesley Publishing Company, Inc. (1978)

35. Jasprit Singh, *Physics of Semiconductors and Their Heterostructures*, McGraw-Hill, Inc., 219(1993)

36. J. Perriere and E. Millon etc., Appl. Phys. Lett. 91, 690 (2002)

37. Y. Chen, D. M. Bagnall, H. J. Koh, K. T. Park, K. Hiraga, Z. Zhu, and T. Yao, J. Appl. Phys. 84, 3912(1998).

38. K. Pinardi, U. Jain, S. C. Jain, H. E. Maes, R. Van Overstraeten, and M. Willander, J. Appl. Phys. 83, 4724(1998).

39. T. Zheleva, K. Jagannadham, and J. Narayan, J. Appl. Phys. 75, 860(1994)

40. D. J. Eaglesham and M. Cerullo, Phys. Rev. Lett. 64, 1943(1990).

41. S. Guha, A. Madhukar, and K. C. Rajkumar, Appl. Phys. Lett. 57, 2110(1990).

42. See, for example, J. A. Floro, S. J. Hearne, J. A. Hunter, P. Kotula, E. Chason, S. C. Seel, and C. V. Thompson, J. Appl. Phys. 89, 4886(2001), and references therein.

43. P. F. Miceli and C. J. Palmstrøm, Phys. Rev. B51, 5506(1995).

44. This does not exclude the possibility of presence a 2D continuous wetting laye. In view of the AFM image of 2 or 5-nm-thick ZnO samples, however, a 2D layer, if present, is believed to be of negligible thickness. This is s big contrast to Cho et al.'s report that their ZnO growth on sapphire at 300°C by sputtering shows 2D layer growth as thickness up to 5 nm. (See reference 5.) The difference may be ascribed to the different growth temperature used, which cririically sffects the surface adatom mobility ad thus the growth mode.

45. The surface energy of ZnO(0001) is known to be $4.0 J/m^2$, much larger than $1.4 J/m^2$ of sapphire. See A. Wander, F. Schedin, P. Steadman, A. Norris, R. McGrath, T. S. Turner, G. Thornton, and N. M. Harrison, Phy. Rev. Lett. 86, 3811 (2001) for ZnO surface energy and R. F. Cook, J. Mater. Res. 1, 852(1986) for sapphire surface energy.

46. V. Shchukin and D. Bimberg, Rev. Mod. Phys. 71, 1125(1999)

47. A. Ohtomo, K. Tamura, K. Saikusa, K. Takahashi, T. Makino, Y. Segawa, H. Koinuma, and M. Kawasaki, Appl. Phys. Lett. 75, 2635(1999)

48. R. C. Neville, and C. A. Mead, J. Appl. Phys. 41, 3795 (1970)

49. H. Fabricius, T. Skerttrup, and P. BISGAARD, Appl. Opt., 25, 2764(1986)

50. H. Sheng, S. Muthukumar, N. W. Emanetoglu, and Y. Lu, Appl. Phys. Lett. 80, 2123(2002)

51. J. Tersoff, J. Val. Sci. Technol. B 3(4), 1985

52. H. Morkoç, "Nitride Semiconductors and Devices", Springer (1998)

53. Dieter K. Schroder, "*Semiconductor Material and Device Characterization*", John Wiley & Sons, Inc. (1990)

54. T. Wolkenstein, "*Electronic Processes on Semiconductor Surfaces during Chemisorption*", Consultants Bureau, New York (1992)

55. H. Geistlinger, Surf. Sci. 277 (1992) 429

56. A. Rothschild, Y. Komem, and N. Ashkenasy, J. Appl. Phys., 92 (2002) 7090

57. K. S. Kim, M. G. Cheng, H. K. Cho, E. K. Suh, and H. J. Lee, Appl. Phys. Lett., 80, 799(2002)

58. D. C. Look and R. J. Molnar, Appl. Phys, Lett., 70, 3377 (1997)

59. Landolt-Börnstein New Series, "Numerical Data and Functional Relationships in Sciences and Technology", vol 17, Springer-Verlog (1984)

60. Ji-Myon Lee, Kyoung-Kook Kim, Seong-Ju Park, and Won-Kook Choi, Appl. Phys. Lett. 78, 3842(2001)

61. E. Kaldis, "Current Topics in Material Science", vol. 7, North-Holland Publishing Company (1981)

62. Bahaa E. A. Saleh, and Malvin Carl Teich, *Fundamentals of Photonics*, John Wiley & Sons, Inc. (1991)

63. Pallab Bhattacharya, *Semiconductor Optoelectronic Devices*, Prentice-Hall, Inc. (1994)

64. Kwok K. Ng, *Complete Guide to Semiconductor Devices*, McGraw-Hill, Inc., (1995)

65. D. C. Look, D. C. Reynolds, J. W. Hemsky, R. L. Jones, and J. R. Sizelove, Appl. Phys. Lett. 75, 811(1999)

66. P. Schreiber, T. Dang, G. Smith, T. Pickenpaugh, P. Gehred, and C. Litton, Proc. SPIE 3629, 230(1999)

67. Y. Takahashi, M. Kanamori, A. Kondoh, H. Minoura, Y. Ohya, Jpn. J. Appl. Phys. 1994, 33, 6611

68. Y. Chen, D. M. Bagnall, H. J. Koh, K. T. Park, K. Hiraga, Z. Zhu, and T. Yao, J. Appl. Phys. 84, 3912(1998)

69. Kohn, G. Ceder, D. Morgon, and Chris G. Van de Walle, Phys. Rev. 61, 15019(2000)

70. Yong Woo Choi, and Byung Tae Ahn, J. Appl. Phys. 1999, 86, 4004

71. D. K. Bowen, and B. K. Tanner, *High resolution x-ray diffractometry and topography*, Taylor & Francis, London, 1998.

72. P. F. Miceli, and C. J. Palmstrøm, Phys. Rev. B, 51, 5506(1995)

73. W. Yang, R. D. Vispute, S. Choopun, R. P. Sharma, and Venkatesan, Appl. Phys. Lett. 78, 2787(2001)

74. Hannes Kind, Haoquan Yan, Benjamin Messer, Mathew Law, and Peidong Yang, Adv. Mater. 14, 158(2002)

75. Yasutaka Takahashi, Masaaki Kanamori, and Akiko Kondoh, Jpn. J. Appl. Phys. 33, 6611(1994)

76. Y. Liu, C. R. Gorla, S. Liang, N. Emanetoglu, Y. Lu, H. Shen, and M. Wraback, J. Electron. Mater. 29, 69(2000)

77. K. S. Kim, M. G. Cheng, H. K. Cho, E. K. Suh, and H. J. Lee, Appl. Phys. Lett., 80, 799(2002)

78. D. C. Look and R. J. Molnar, Appl. Phys, Lett., 70, 3377 (1997)

79. Landolt-Börnstein New Series, “Numerical Data and Functional Relationships in Sciences and Technology”, vol 17, Springer-Verlog (1984)

80. E. Muñoz, E. Monroy, J. A. Garrido, I. Izpura, F. J. Sánchez, M. A. Sánchez-García, E. Calleja, and B. Beaumont, P. Gibart, Appl. Phys. Lett. 71, 870(1997)

81. Y. Takahashi, M. Kanamori, A. Kondoh, H. Minoura, Y. Ohya, Jpn. J. Appl. Phys. 1994, 33, 6611

82. H. Geistlinger, Surf. Sci. 277, 429(1992)

83. J. Lagowski, E. S. Sproles, Jr., and H. C. Gatos, J. Appl. Phys. 48, 3566(1977)

84. A. Rothschild, Y. Komem, and N. Ashkenasy, J. Appl. Phys. 92, 7090(2002)

85. W. Hirschwald, P. Bonasewice, L. Ernst, M. Grade, D. Hoffmann, S. Krebs, R. Littbarski, G. Neumann, M. Grunze, D. Kolb, and H. J. Schulz, “Current Topics in Material Science”, vol. 7, North-Holland(1981)